TOWARDS MORE EFFICIENT ACCELERATING RF SYSTEMS: SUPERCONDUCTING ENERGY RECOVERY LINACS AND THERMOMETRY OF HIGH Q CAVITIES

A Dissertation

Presented to the Faculty of the Graduate School

of Cornell University

in Partial Fulfillment of the Requirements for the Degree of

Doctor of Philosophy

by

Nilanjan Banerjee

December 2020

TOWARDS MORE EFFICIENT ACCELERATING RF SYSTEMS:
SUPERCONDUCTING ENERGY RECOVERY LINACS AND
THERMOMETRY OF HIGH Q CAVITIES

Nilanjan Banerjee, Ph.D.
Cornell University 2020

Multi-turn Energy Recovery Linacs (ERLs) powered by Superconducting Radio Frequency (SRF) cavities enable the production of continuous bright high-current beams while being very efficient. The low energy consumption can be attributed to diminishing refrigeration costs from increasingly advanced SRF materials and the efficient use of rf power in maintaining the accelerating gradient. Operating the main linac cavities of SRF ERLs with large Q_L reduces average rf power consumption but increases its sensitivity to resonance detuning. We discuss passive measures as well as develop a novel Active Noise Control algorithm to reduce microphonics detuning and ensure stable field. This dissertation describes the complete rf commissioning process of a SRF main linac in detail including the use of automation in various steps. These techniques were utilized in the Cornell BNL ERL Test Accelerator (CBETA), the first multi-turn SRF ERL, which achieved an energy recovery efficiency of 99.4 % during high-current operations in the single turn mode. We further analyze the effect of transient beam loading using a novel linear model which predicts the existence of reactive beam loading arising from relativistic effects in the presence of low energy beam. Finally, we discuss a novel thermometry system to image local heating and thermal runaway on the surface of SRF cavities, thus aiding the development of more efficient SRF materials for future ERLs.

BIOGRAPHICAL SKETCH

Nilanjan was born in Kolkata, India and spent his childhood there. As a *Bangali*, his favorite things were food and *Durga Pujo*. In 2010, he began his undergraduate education in physics at the Indian Institute of Technology Kharagpur where he spent a lot of time watching American TV. Along the way he became passionate about particle accelerators and after receiving his Integrated Master of Science degree, joined Cornell University for his PhD studies in 2015. During graduate school, he met Heather and the two became engaged. He finished his PhD in 2020.

To my parents who have encouraged me to follow my dreams and supported me throughout.

ACKNOWLEDGEMENTS

Don't you know the first law of physics? Anything that's fun costs at least eight dollars. - Eric Cartman

What I cannot create, I do not understand.

-Richard Feynman

Before I begin, I want to acknowledge the humanitarian crisis that is the COVID-19 pandemic. At the time of writing, more than 1.4 million people have died worldwide, and the death toll is still rising. I recognize that physicists are among the privileged people, who are able to work remotely and reduce the chance of infection which cannot be said for the vast majority of the working population. I am indebted to Cornell University, CLASSE and all my colleagues for maintaining a safe working environment following all available scientific guidelines during these adverse times.

I would not have been able to complete the research presented in this dissertation without the support and contribution of numerous people.

I want to begin by expressing my gratitude towards my family back home who instilled and nurtured my interest in science and whose constant support and encouragement enabled me to complete the doctoral program. I want to thank my fiancée, Heather who has always been my champion and whose love and companionship has changed me and made my life brighter. Even though we now live a 1000 miles apart, she has never let me feel the distance and I am grateful for all her patience, understanding and support. In this time of political upheaval, my life in the US would have been a lot different without Heather and her family who have given me a home away from home.

I want to express my deepest appreciation for my advisor, Prof. Georg Hoffstaetter whose mentorship, encouragement and deep physical insight has en-

abled me to become the researcher I am today. Besides guiding my research and scholarship, he has inculcated in me the skill of scientific communication. I am indebted to his teachings, his enthusiasm and ardent advocacy of my work which has set me on a positive trajectory in my career. In addition, I want to thank Prof. Matthias Liepe for advising me throughout the process of rf commissioning and for giving me the exciting opportunity to work on fundamental SRF, thus extending my work on CBETA. I especially want to acknowledge his patience and understanding during the pandemic where he prioritized the safety of the members of the lab. I want to also thank Prof. Tomas Arias for being a part of my special committee and giving me the chance to learn about classical DFT.

Participating in the CBETA commissioning process was the highlight of my PhD and I wouldn't have succeeded without the guidance and mentorship of many people. I first want to recognize Peter Quigley for teaching me everything I know about linac cryomodules, rf instrumentation, operations, cryogenics and safety. I want to thank Adam Bartnik and Colwyn Gulliford for being my teachers and mentors in the control room, fielding my countless questions and advising me on academics and beyond. I want to thank Kirsten Deitrick and John Dobbins for actually doing all the work for the Equipment Protection System, while I got to present the results. I also want to acknowledge Scott Berg and Dejan Trbojevic for their insight and uplifting presence in the control room, and especially Dejan for dinner on many many nights.

At Newman, I found a welcoming team ready to teach me everything about fundamental SRF testing. I especially want to thank Ryan Porter for teaching me about the T-map, the vertical test systems and procedures in the clean room . I also want to thank James Sears for giving me the required training and making

sure I had all I needed for my research.

I want to thank all my fellow graduate students including Peter Koufalis, William Lou and Neil Stilin among others. I am indebted to the undergraduate students I have mentored over the years who have aided my research, especially Joseph Petrullo for his detailed radiation simulations of the damage to permanent magnets in CBETA. There have been countless others who contributed to my work over the years: Stephen Brooks, David Burke, Jim Crittenden, Fumio Furuta, Mingqi Ge, Roger Kaplan, Vaclav Kostroun, Yulin Li, Rob Michnoff, Ritchie Patterson, Steve Peggs, Dan Sabol, Colby Shore, Eric Smith, Karl Smolenski, Zeming Sun, Vadim Veshcherevich, Dwight Widger and everyone else in the CBETA and Newman team.

Last but not the least, I want to acknowledge my wonderful friends who have stood with me through thick and thin and made my graduate school experience a memorable one. I especially want to mention Abhisek Datta, Ruofan Li and Thomas Oseroff for all their friendship, emotional support and fun adventures over the years. Finally, I want to thank my Friday dinner (now Zoom dinner) buddies Gabriel Bonilla, Patrick Hollister and Thy Le for endless discussions on physics, politics, philosophy and life in graduate school.

TABLE OF CONTENTS

LIST OF TABLES

LIST OF FIGURES

CHAPTER 1

INTRODUCTION

Radio Frequency (rf) acceleration has been the primary method of accelerating charged particles ever since it was first introduced by Rolf Widerøe in 1928. In this method, particles are introduced into an oscillating electric field sustained inside a hollow metallic chamber called a cavity. If particles enter at the right time, they are subject to forces which increases their kinetic energy. Many different types of accelerating structures have been developed over the years, all of them working on this same basic principle. Copper has been a common choice when constructing these cavities for its relatively low resistivity at room temperature and cost of machining, compared to other readily available metals. The introduction of superconducting materials for making cavities was a major leap which greatly reduced the amount of dissipation in the accelerating structures thus paving the way for the efficient high-current and high energy particle accelerators of today.

The concept of Energy Recovery Linacs (ERLs) introduced by Maury Tigner in 1965[Tigner, 1965], provides a path to further push our capabilities in the medium energy, high beam current and brightness frontier. In this method, the kinetic energy of the used beam is absorbed back into the rf structures for accelerating newly injected beam. The use of Superconducting Radio Frequency (SRF) technology along with the technique of energy recovery enables the construction of highly efficient machines capable of providing multi-megawatt beam powers while using a lot less rf power compared to conventional linear accelerators(linacs) achieving the same beam parameters. This chapter reviews the

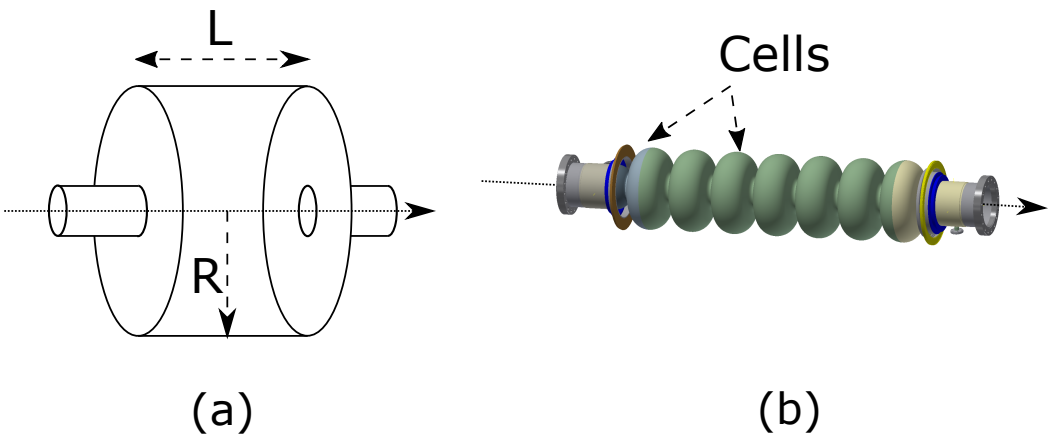

Figure 1.1: Examples of high-β resonant cavities. (a) Ideal pillbox with radius R and accelerating gap L including tubes to allow the passage of the beam. (b) Superconducting Radio Frequency cavity with 7 cells.

fundamentals of resonant cavities, SRF technology, cavity operations and ERLs to provide a context for the research presented in this dissertation.

1.1 Resonant Cavities

Resonant cavities provide an efficient way of sustaining large electric fields for use in acceleration of charged particles. This is realized by designing a structure which can sustain standing waves oscillating at a design resonance frequency. The net energy provided to the particles is equal to the total work done by the time-dependent electric field on the particle as it traverses the cavity. Figure 1.1 shows rf cavities used to accelerate particles which travel close to the speed of light ($\beta \equiv v/c \approx 1$). To ensure that the particle only sees electric field in one direction, the length it travels in the presence of field, called the *accelerating gap* is fixed to less than half the wavelength ($\lambda/2$) of the standing waves. The left

panel shows an ideal pillbox cavity fitted with beam tubes at the ends while the particle travels along the axis of this structure getting accelerated according to the principle described above. The right panel shows a SRF cavity with cylindrical symmetry consisting of 7 cells, each of length $\lambda/2$ and with a rounded shape to prevent multipacting.[1] Microwaves coupled into this cavity set up standing waves where consecutive cells have a phase difference of π between each other. This allows an ultra-relativistic particle to travel through the cavity while only witnessing fields with the correct sign. In contrast, low-β structures are designed to have accelerating gaps of $\beta\lambda/2$, with a comparatively large λ i.e low resonant frequency, close to 100 MHz compared to $\gtrsim$ 500 MHz for high-β structures. The electrodynamics of the resonant modes is the same regardless of the shape of the cavity, and is important in characterizing the performance of these structures.

The Maxwell's equations in free space are,

$$\vec{\nabla} \cdot \vec{E} = \frac{\rho}{\epsilon_0}\,, \tag{1.1a}$$

$$\vec{\nabla} \cdot \vec{B} = 0\,, \tag{1.1b}$$

$$\vec{\nabla} \times \vec{E} = -\frac{\partial \vec{B}}{\partial t}\,, \tag{1.1c}$$

$$\vec{\nabla} \times \vec{B} = \mu_0 \vec{J} + \mu_0 \epsilon_0 \frac{\partial \vec{E}}{\partial t}\,, \tag{1.1d}$$

where $\vec{E}$ is the electric field, $\vec{B}$ is the magnetic flux density, μ_0 and ϵ_0 are the permeability and permittivity of vacuum respectively. ρ and $\vec{J}$ represent the charge and current density in the cavity respectively. The fields are subject to boundary conditions at the interface between vacuum and the metal surface.

[1] Multipacting refers to the resonant emission of electrons and subsequent multiplication driven by rf electric fields on a cavity surface.[Padamsee et al., 2008]

For a perfect conductor, the electric field must be normal to the surface while the magnetic flux density is parallel to the surface. These boundary conditions may be expressed as,

$$\vec{E} \times \mathrm{d}\vec{S} = 0,\ \vec{H} \cdot \mathrm{d}\vec{S} = 0, \tag{1.2}$$

where $\mathrm{d}\vec{S}$ is the normal vector to an infinitesimal patch on the inner surface S of the cavity and $\vec{H}$ is the magnetic field. The solution to the above set of equations can be decomposed into a set of discrete eigenmodes of the structure, i.e $\vec{E}(\vec{r}, t) = \sum e_k(t)\vec{\mathcal{E}}_k(\vec{r})$, where $\vec{\mathcal{E}}_k(\vec{r})$ is an eigenmode with index k. The electric field inside the cavity from a single eigenmode in steady state unperturbed by charges or currents is described by a standing wave $\vec{\mathcal{E}}_k(\vec{r})\mathrm{e}^{i\omega_k t}$, where ω_k is the resonant frequency of the mode. Combining the Maxwell's equations for the single eigenmode $\vec{\mathcal{E}}_k$ without the source terms yields the Helmholtz equation,

$$\vec{\nabla}^2\vec{\mathcal{E}}_k + \frac{\omega_k^2}{c^2}\vec{\mathcal{E}}_k = 0\,, \tag{1.3}$$

where $\vec{\nabla} \cdot \vec{\mathcal{E}}_k = 0, \vec{\mathcal{E}}_k \times \mathrm{d}\vec{S} = 0$ at the surface and c is the speed of light in vacuum. Any resonant structure can be characterized by an infinite set of eigenmodes described by Eq. (1.3). In the case of structures exhibiting the same topology as a pillbox, the eigenmodes can be divided into two major classes, Transverse Magnetic (TM) and Transverse Electric (TE) describing eigenmodes where either the magnetic fields or the electric fields are purely transverse to the axis of the cavity respectively. TM modes are used for particle acceleration since the electric field can be in the longitudinal direction.

In the case of an ideal pillbox without beam tubes, analytical solutions to Eq. (1.3) exists for the complete set of TM_{mnp} eigenmodes, where m, n and p are indices indicating the number of nodes of the solution in the azimuthal (ϕ), ra-

dial (r) and longitudinal (z) directions respectively. Modes with $m = 0$ are called *monopole* modes since the field patterns exhibit azimuthal symmetry. These $0np$ modes allow a non-zero longitudinal electric field on axis given by,

$$\mathcal{E}_{z_{0np}}(r = 0, z) = \mathcal{E}_{0np} \cos\left(\frac{p\pi z}{L}\right), \tag{1.4}$$

where L is the length of the cavity and $\mathcal{E}_{0np}$ is the normalization factor. The resonance frequency ω_{0np} is,

$$\omega_{0np} = c\sqrt{\left(\frac{u_{0n}}{R}\right)^2 + \left(\frac{p\pi}{L}\right)^2}, \tag{1.5}$$

where u_{0n} is the nth zero of the Bessel function $J_0(x)$. The monopole mode of the lowest frequency also called the fundamental mode of the cavity TM_{010} is usually selected for particle acceleration. In multi-cell cavities, the TM010 in each cell couple together creating a fundamental mode passband containing the same number of modes as the number of cells. The mode which shows a phase difference of π between consecutive cells is chosen for acceleration. All modes with higher resonance frequencies are called Higher Order Modes (HOMs) which are usually disruptive to the beam, capable of causing Beam Break-Up instabilities (BBU)[Hoffstaetter and Bazarov, 2004] in many accelerators. This chapter focuses on the TM010 π-mode.

The net energy gain of a particle traveling through a cavity depends on the electric field and the velocity of the particle. For a beam of arbitrary energy, the equations of motion along the axis are given by,

$$mc^2 \frac{\mathrm{d}\gamma}{\mathrm{d}t} = qE_{z_0}(r = 0, z)c\sqrt{1 - \frac{1}{\gamma^2}} \cos(\omega_0 t + \phi), \tag{1.6a}$$

$$\frac{\mathrm{d}z}{\mathrm{d}t} = c\sqrt{1 - \frac{1}{\gamma^2}}, \tag{1.6b}$$

where γ is the relativistic factor of the charged particle with mass m and charge q, $E_{z_0}(r = 0, z)$ is the longitudinal field pattern for the fundamental eigenmode (constant for a pillbox) with frequency ω_0 and ϕ is the phase of the field when the particle enters the cavity. When the incoming beam is ultra-relativistic i.e. $\gamma >> 1$, then the energy gain of the particle is given by,

$$\Delta\mathcal{E}(\phi) = q \int_0^L E_{z_0}(r = 0, z) \cos\left(\frac{\omega_0 z}{c} + \phi\right) \mathrm{d}z\,, \tag{1.7}$$

where r is the radial coordinate with respect to the axis of the structure. The accelerating voltage V_c of a cavity is defined as the maximum energy gain imparted to a single ultra-relativistic bunch when it enters at the *on-crest phase* and is given by,

$$V_c \equiv \max_{\phi} \Delta\mathcal{E}(\phi)/q = \left| \int_0^L E_{z_0}(r = 0, z) \mathrm{e}^{i\frac{\omega_0 z}{c}} \mathrm{d}z \right|. \tag{1.8}$$

The average accelerating gradient is defined as $E_{acc} \equiv V_c/L$, where L is the active length of the cavity. Figure 1.2 shows the energy gain of an electron as a function of arrival phase as it travels through a 7-cell cavity (Fig. 1.1 (b)) at an accelerating voltage of 6 MV for two incident energies $\mathcal{E}_i$, 6 MeV and 600 MeV. At $\mathcal{E}_i = 600$ MeV the energy gain corresponds to an exact sinusoid of phase with amplitude matching the accelerating voltage. At low energies, the relativistic effects due to the comparatively low β change the response of the cavity, slightly reducing the maximum energy gain while shifting the on-crest phase by a few degrees.

Power dissipated as heat from the walls of the cavity under the influence of the oscillating magnetic fields at the surface is a crucial limiting factor in operations. The total power P_c dissipated at the surface is given by,

$$P_c = \frac{1}{2} \int_S R_s |\vec{H}(\vec{r})|^2 \,\mathrm{d}S \tag{1.9}$$

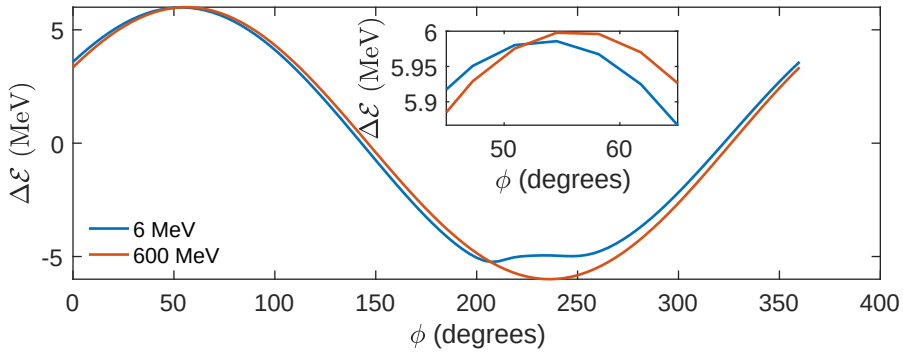

Figure 1.2: Energy gain as a function of arrival phase for 6 MeV (blue) and 600 MeV (red) electrons traveling through a 7-cell cavity with accelerating voltage set to 6 MV.

where R_s is the surface resistance of the metal dependent on position and $|\vec{H}|$ is the amplitude of the oscillating magnetic field at the surface. Whereas, the total energy U contained in the eigenmode is given by,

$$U = \frac{1}{2}\epsilon_0 \int_V |\vec{E}(\vec{r})|^2 \, \mathrm{d}V = \frac{1}{2}\mu_0 \int_V |\vec{H}(\vec{r})|^2 \, \mathrm{d}V \,, \tag{1.10}$$

with $|\vec{E}(\vec{r})|$ being the amplitude of the oscillating electric field in the cavity. Combining the parameters V_c, P_c, U and ω_0 yields several important figures of merit which can quantify the performance of a cavity and provide a basis to optimize designs.[Padamsee et al., 2008]

- The **intrinsic quality factor** of the cavity defined as $Q_0 \equiv \omega_0 U / P_c$, approximates the number of rf cycles required to dissipate the energy stored in the eigenmode if left unperturbed, and thus is a measure of heat dissipation.
- The **ratio of shunt impedance to the quality factor** defined as $R/Q \equiv V^2/(2\omega_0 U)$ characterizes the response of the eigenmode to the passage of beam current.
- The **geometry factor** defined as $G \equiv \bar{R}_s Q_0$ is a size independent character-

Parameter	Pillbox	Cornell 7-cell
R/Q (Ω)	98	387
G (Ω)	256.6	270.7
E_{pk}/E_{acc}	1.6	2.1
H_{pk}/E_{acc} (Oe/(MV/m))	30.5	42.0

Table 1.1: Comparison of the Cornell 7-cell cavity[Valles, 2014] with an ideal pillbox cell at the same frequency.

ization of the cavity. $\bar{R_s} \equiv \int_S R_s |\vec{H}(\vec{r})|^2 \, \mathrm{d}S / \int_S |\vec{H}(\vec{r})|^2 \, \mathrm{d}S$ is the surface resistance averaged over S, weighted by the square of the field $|\vec{H}(\vec{r})|^2$.

- The **ratios of peak fields to the accelerating gradient**, E_{pk}/E_{acc} and H_{pk}/E_{acc} determines the maximum energy gain which can be attained in a cavity.

Table 1.1 compares these parameters for a 1.3 GHz 7-cell cavity (Fig. 1.1(b)) to an ideal pillbox with the same resonant frequency.

1.2 RF Superconductivity

The power dissipated as heat from the rf surface is proportional to the average surface resistance of the metal used to fabricate the cavity. For a typical copper cavity at room temperature this is $\approx$ 10 mΩ, which gives rise to quality factors of few times 10^4. As an example, a single pillbox cell with parameters listed in Tab. 1.1 operating at 1 MV would dissipate $\approx$ 200 kW. To sustain this large power dissipation, copper cavities are usually operated in pulsed mode i.e the rf accelerating field stays on for a short instant of the order of micro-seconds, and then stays off for a longer period to allow the structure to cool down. Since the beam can only be accelerated in short bursts, this severely limits the total

beam current in copper linacs. While low temperatures can be used to improve conductivity, at low temperatures, the surface resistance converges to a limit set by the anomalous skin effect. However copper cavities provide an advantage of being able to reach very high fields when compared to their SRF counterparts which are subject to critical fields as explained later in this section. Cryogenic copper cavities are being investigated as a method of reaching very high accelerating gradients of 250 MV/m in pulsed mode.[Cahill et al., 2018]

Superconducting materials are characterized by their *zero* electrical resistance to direct currents (DC) below a **transition temperature** T_c.[Ashcroft and Mermin, 1976] This property has been extensively used to make very strong electromagnets in particle accelerators. In contrast, superconductors dissipate heat under rf fields, although at a rate much smaller than copper and are subsequently also used to make rf cavities. The transition temperature of Niobium, the most widely used material for SRF applications is 9.2 K, necessitating the use of cryogenic systems in transferring away the heat in order to sustain the required temperatures during operation. Despite this, the overall electrical power consumption of a typical SRF accelerator excluding the power transferred to the beam but including the contribution from the refrigeration systems and the rf power sources is still a factor of 100 smaller than an equivalent normal conducting system.[Padamsee et al., 2008] Hence, SRF cavities are widely used in modern particle accelerators.

Superconductors also exhibit the Meissner effect, which refers to the phenomenon of expulsion of all magnetic field from the bulk of the material as it

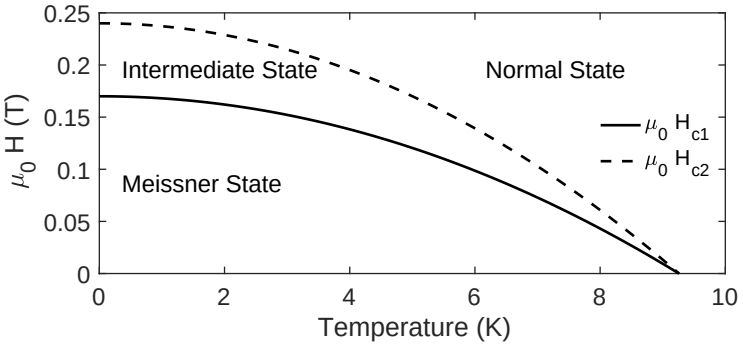

Figure 1.3: The phases of Niobium, a Type II superconductor with different regions separated by the lower and upper critical fields, $\mu_o H_{c1}$ and $\mu_o H_{c2}$ respectively.

cools below T_c. Combining this effect with ballistic transport of charge carriers inside the bulk gives rise to the London's equations which describe the electrodynamics of superconductors. One important parameter arising out of these equations is called the **London penetration depth**, λ_L. This is the characteristic length scale of penetration of applied magnetic fields $\vec{H}$ into the bulk of the superconductor expressed as,

$$\vec{\nabla}^2 \vec{H} = \frac{\vec{H}}{\lambda_L^2} \,. \tag{1.11}$$

The superconductor equivalently sets up a current density $\vec{j}_s$ to attenuate the field as it enters into the bulk. The existence of finite density of charge carriers in the superconductor available to support $\vec{j}_s$ results in a maximum amount of applied magnetic field beyond which a superconductor can no longer act as a perfect diamagnet even below T_c.

Low temperature superconductors are classified according to their behavior under the influence of external magnetic field. Type-I superconductors demonstrate only a single temperature-dependent critical field H_c beyond which the

material becomes normal conducting even below T_c. Whereas, Type-II superconductors exhibit two critical limits: the **lower critical field** H_{c1} beyond which some magnetic flux enters the bulk creating an *intermediate state* containing localized normal conducting regions in an otherwise superconducting bulk, and the **upper critical field** H_{c2} beyond which all of the material becomes normal conducting. The superconducting phases for bulk Niobium, a Type-II superconductor is illustrated in Fig. 1.3. The exact preparation of the sample including its purity and crystalline structure determine the exact values of the critical fields.[Dhakal et al., 2011]

The phenomenon of low temperature superconductivity can be explained using the Bardeen–Cooper–Schrieffer (BCS) theory[Bardeen et al., 1957] which is based on the existence of *Cooper pairs* which undergo Bose-Einstein condensation below T_c. Superconductivity under this mechanism appears from the combination of two distinct processes. Pairs of electrons occupying states close to the Fermi energy combine together to form bosons under a net attractive interaction mediated by lattice vibrations or *phonons*.[Cooper, 1956] In addition, these bosons undergo Bose-Einstein condensation below T_c to occupy a single quantum state thereby providing a channel for current to flow without getting scattered by phonons, lattice defects or impurities. The spatial extent of these Cooper pairs or equivalently the distance between the interacting electrons is known as the **coherence length** ξ_0 and it affects the transport properties of these charge carriers. The paired electrons themselves leave a band of electron states in the superconductor unoccupied, creating an **energy gap** Δ. At $T < T_c$, a fraction of Cooper pairs gain energy comparable to this gap giving rise to *quasiparticle excitations*[Kivelson and Rokhsar, 1990], and creating a population of

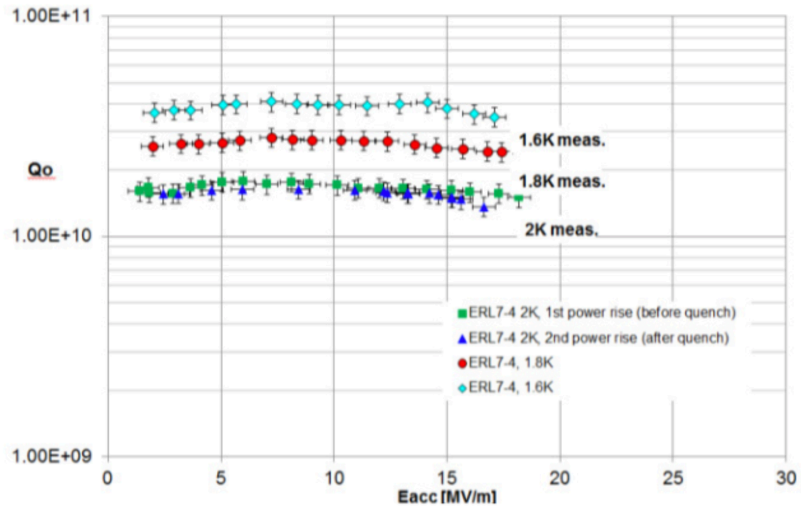

Figure 1.4: Intrinsic quality factor Q_0 as a function of accelerating gradient E_{acc} for the Cornell 7-cell cavity. Reproduced from Eichhorn et al. [2015]

.

normal conducting carriers in addition to the superconducting species.

While a DC current can flow through a superconductor with zero resistance, rf currents tend to flow through both the superconducting and the normal conducting channels giving rise to ohmic dissipation. The surface resistance of a superconductor due to the BCS contribution R_{BCS} for temperatures $T < T_c/2$, is given by, [Ciovati, 2014]

$$R_{BCS}(T) = A_s \omega^2 \mathrm{e}^{-\frac{\Delta(0)}{k_B T}}, \tag{1.12}$$

where ω is the microwave frequency, $\Delta(0)$ is the energy gap at 0 K and A_s is a constant which depends on material parameters. Even though Eq. (1.12) predicts zero resistance at 0 K, a residual resistance R_0 dominates at low temperatures leading to a net surface resistance $R_s = R_{BCS}(T) + R_0$. In practice the dissipation in a SRF cavity is also dependent on the accelerating field. Figure 1.4 shows the

field dependence of the intrinsic quality factor $Q_0 = G/R_s$ for the Cornell 7-cell cavity made of Niobium.

The maximum accelerating gradient which can be sustained by a Niobium SRF cavity depends on many factors including metallurgy[Dhakal et al., 2011], surface preparation[Dhakal et al., 2013], shape of cavity[Devanz, 2001], doping[Grassellino et al., 2017] and contamination[Koufalis et al., 2016] among others. The intrinsic limitation of a superconductor to sustain its state in the presence of rf surface magnetic fields may be explained using thermodynamic considerations. The net change in free energy due to the entry of magnetic flux lines into the bulk of the superconductor can be attributed to two parts: the increase due to the formation of a normal conducting region with a characteristic length scale ξ_0, and the decrease due to the penetration of magnetic flux with length scale λ_L. The interplay of these quantities and the resulting values of critical fields can be explained under the *Ginsburg-Landau* (GL) theory. The relevant upper limit of surface magnetic field which can be sustained by an ideal superconductor in the context of SRF cavities is given by the **superheating field** H_{sh}.

While Niobium has been the material of choice for modern SRF accelerators, Niobium-tin (Nb_3Sn) reaches much lower surface resistance when compared to Niobium at the same temperature. This has opened the possibility of operating accelerating cavities at higher temperatures using efficient in-situ refrigeration.[Stilin et al., 2020] The superheating field of Nb_3Sn is predicted to be approximately twice[Padamsee et al., 2008] that of Niobium. However experimental studies have failed to reach the high theoretical predictions due to

thermal runaway at comparatively low fields.[Posen and Hall, 2017] A detailed study on the onset and spread of local heating can provide insight into the mechanisms impeding the performance of this new material.

1.3 RF Operations

The accelerating gradient of a SRF cavity is subject to perturbations from the beam, changes in resonance frequency of the structure, dissipation from the walls and the action of the input coupler which couples in rf waves into the cavity. The evolution of the fundamental mode under these effects may be modeled as a simple harmonic oscillator derived from the Maxwell's equations (Eq. (1.1)). The wave equation of the electric field inside the cavity is given by,

$$\frac{1}{c^2}\frac{\partial^2 \vec{E}}{\partial t^2} - \vec{\nabla}^2 \vec{E} = -\mu_0 \frac{\partial \vec{J}}{\partial t} - \frac{\vec{\nabla}\rho}{\epsilon_0}, \tag{1.13}$$

where $\vec{J}$ and ρ are the current density and the charge distribution respectively. These source terms account for the beam current, surface currents and charges set up in the cavity wall and current and charges at the rf input coupler. If the fundamental mode accounts for almost all the electric field inside the cavity then,

$$\vec{E}(\vec{r}, t) \equiv V(t)\vec{\mathcal{E}}_0(\vec{r}) \equiv \mathcal{R}\{\tilde{V}_c e^{i\omega_0 t}\}\vec{\mathcal{E}}_0(\vec{r}) \tag{1.14}$$

where $\vec{\mathcal{E}}_0(\vec{r})$ is the fundamental eigenmode with frequency ω_0 satisfying Eq. (1.3) and $\mathcal{R}\{\}$ represents the real part of a complex number. $V(t)$ is the time-dependent fundamental mode voltage while $\tilde{V}_c$ is a complex phasor. The normalization of $\vec{\mathcal{E}}_0(\vec{r})$ is chosen so that the acceleration voltage is $|\tilde{V}_c|$. Using the definition of

accelerating voltage from Eq. (1.8) gives,

$$\max_{\phi} \int_0^L \mathcal{R}\{|\tilde{V}_c| e^{i\omega_0 z/c + i\phi}\} \mathcal{E}_{z_0}(r=0,z)\, \mathrm{d}z = |\tilde{V}_c|\,, \tag{1.15}$$

where ϕ is argument of the complex number $\tilde{V}_c$. Dividing by $|\tilde{V}_c|$ on both sides and recognizing that the LHS is maximized when it's purely real, results in,

$$\int_0^L \mathcal{E}_{z_0}(r=0,z) e^{i\frac{\omega_0 z}{c}}\, \mathrm{d}z = e^{-i\phi_0}\,, \tag{1.16}$$

where ϕ_0 is referred to as the *on-crest phase* of the cavity with respect to the beam. Combining the definition of the ratio of shunt impedance to the quality factor $R/Q \equiv V^2/(2\omega_0 U)$, with the amount of stored energy gives the normalization of the eigenmode as,

$$\int_V |\vec{\mathcal{E}}_0(\vec{r})|^2\, \mathrm{d}V = \frac{1}{\epsilon_0 \omega_0 R/Q}\,. \tag{1.17}$$

Further plugging in the approximate electric field given by Eq. (1.14) into the wave equation gives,

$$\Big(\frac{\ddot{V} + \omega_0^2 V}{c^2}\Big)\vec{\mathcal{E}}_0(\vec{r}) = -\mu_0 \frac{\partial \vec{J}}{\partial t} - \frac{\vec{\nabla}\rho}{\epsilon_0}\,, \tag{1.18}$$

where Eq. (1.3) is used to substitute for the term $\vec{\nabla}^2 \vec{\mathcal{E}}_0$. Multiplying with the eigenmode function on both sides and integrating over the volume of the cavity yields a linear second order ordinary differential equation for the mode voltage,

$$\ddot{V} + \omega_0^2 V = -\omega_0 \frac{R}{Q}\Big[\int_V \frac{\partial \vec{J}}{\partial t} \cdot \vec{\mathcal{E}}_0(\vec{r})\, \mathrm{d}V + c^2 \int_V \vec{\nabla}\rho \cdot \vec{\mathcal{E}}_0(\vec{r})\, \mathrm{d}V\Big]\,, \tag{1.19}$$

where the spatial dependence is averaged away using the mode normalization. Applying the vector identity $\vec{\nabla}\cdot(f\vec{A}) = A\cdot\vec{\nabla}f + f\vec{\nabla}\cdot\vec{A}$, to the second term in the above equation and recognizing that $\vec{\nabla}\cdot\vec{\mathcal{E}}_0 = 0$ gives,

$$\int_V \vec{\nabla}\rho \cdot \vec{\mathcal{E}}_0(\vec{r})\, \mathrm{d}V = \int_S \rho \vec{\mathcal{E}}_0 \cdot\, \mathrm{d}\vec{S}\,. \tag{1.20}$$

Since the charge distribution of the particle bunches are localized around the axis of the cavity, the only contributions to the surface integral comes from the coupler and the wall charges. This leads to,

$$\ddot{V} + \omega_0^2 V = -\omega_0 \frac{R}{Q} \int_V \frac{\partial(\vec{J}_{\text{beam}} + \vec{J}_{\text{coupler}} + \vec{J}_{\text{wall}})}{\partial t} \cdot \vec{\mathcal{E}}_0(\vec{r})\, \mathrm{d}V + \int_S (\rho_{\text{coupler}} + \rho_{\text{wall}}) \vec{\mathcal{E}}_0 \cdot \mathrm{d}\vec{S}\,, \tag{1.21}$$

where $\vec{J}_{\text{beam}}$ is the only contribution from the beam while $\vec{J}_{\text{coupler}}$, ρ_{coupler} and $\vec{J}_{\text{wall}}$, ρ_{wall} are the contributions from the coupler and the wall. A similar result using vector potentials is derived in Chap. 4. Consequently, the evolution of the eigenmode is only driven by currents and not the charge distribution of the bunches traveling through the cavity.

The harmonic time dependence of the accelerating field in a rf cavity requires beam to be bunched and each bunch needs to arrive at a regular time interval with a defined phase relationship with respect to the rf field inside the cavity. Consequently, the dominant spatial Fourier mode of the beam is characterized by a forward moving plane wave with wavelength $\lambda_{\text{beam}} = v_{\text{beam}}/f_0$, where v_{beam} is the velocity of the beam and $f_0 \equiv \omega_0/(2\pi)$ is the resonant frequency of the fundamental mode. For an ultra-relativistic beam localized to the axis, the beam current density may be defined as,

$$\vec{J}_{\text{beam}}(\vec{r}, t) \equiv \mathcal{R}\{\tilde{I}_{\text{beam}} \mathrm{e}^{i(\omega_0 t - \frac{\omega_0 z}{c} - \phi_0)}\} \frac{\delta(r)}{2\pi r} \hat{z}\,, \tag{1.22}$$

where $\tilde{I}_{\text{beam}}$ is a complex phasor whose amplitude equals the Fourier amplitude of beam current at the resonance frequency and the angle from the real axis denotes the phase with respect to maximum acceleration. The actual time averaged current flowing through the beam pipes is $I_b = |\tilde{I}_{\text{beam}}|/2$, where the factor of 2 arises from the Fourier series representation of a bunched beam. Using

Eq. (1.16), the source term for the fundamental mode equation becomes,

$$-\omega_0 \frac{R}{Q} \int_V \frac{\partial \vec{J}_{\text{beam}}}{\partial t} \cdot \vec{\mathcal{E}}_0(\vec{r})\, \mathrm{d}V = -\omega_0 \frac{R}{Q} \frac{\mathrm{d}\mathcal{R}\{\tilde{I}_{\text{beam}} \mathrm{e}^{i\omega_0 t}\}}{\mathrm{d}t} \equiv -\omega_0 \frac{R}{Q} \frac{\mathrm{d}I_{\text{beam}}}{\mathrm{d}t}\,, \tag{1.23}$$

where $I_{\text{beam}}(t) \equiv \mathcal{R}\{\tilde{I}_{\text{beam}} \mathrm{e}^{i\omega_0 t}\}$ is the real time-dependent beam current flowing through the cavity.

The effect of dissipation and the input coupler can be incorporated into the model following a phenomenological approach. The source term attributed to the input coupler can be defined as,

$$-\omega_0 \frac{R}{Q} \Big[\int_V \frac{\partial \vec{J}_{\text{coupler}}}{\partial t} \cdot \vec{\mathcal{E}}_0(\vec{r})\, \mathrm{d}V + \int_S \rho_{\text{coupler}} \vec{\mathcal{E}}_0 \cdot\, \mathrm{d}\vec{S} \Big] \equiv \omega_0 \frac{R}{Q} \frac{\mathrm{d}I_{\text{coupler}}}{\mathrm{d}t}\,, \tag{1.24}$$

where the time dependence of the source term is encoded into an artificial value of current $I_{\text{coupler}}(t)$, which is equivalent to the amount of beam current which would result in the same excitation of field inside the cavity. Finally the dissipation at the walls of the cavity can be included as a damping term in the simple harmonic oscillator which leads to,

$$\ddot{V} + \frac{\omega_0}{Q_0} \dot{V} + \omega_0^2 V = -\omega_0 \frac{R}{Q} \Big(\frac{\mathrm{d}I_{\text{beam}}}{\mathrm{d}t} - \frac{\mathrm{d}I_{\text{coupler}}}{\mathrm{d}t} \Big), \tag{1.25}$$

where the intrinsic quality factor Q_0 determines the rate of dissipation. A description of the rf input coupler and the associated rf power flow is required to complete this model.

Figure 1.5 illustrates the rf power system used to feed linac cavities. The rf power source is represented as a controlled current source generating I_+, which goes through a transmission line with impedance Z_0 into port 1 of a rf circulator. This device allows the flow of rf waves only in one direction denoted by the circular arrow in Fig. 1.5. The forward traveling wave with current I_+ propagates

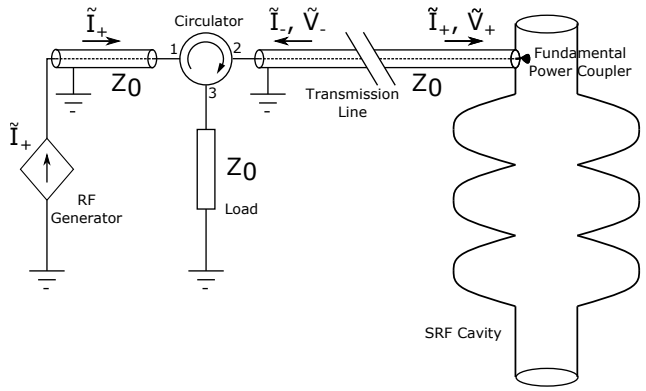

Figure 1.5: High level rf system used to power rf cavities.

into port 2, where it enters another transmission line of the same impedance Z_0, and then it finally reaches the fundamental input coupler. The difference in impedance between the transmission line, Z_0 and the effective impedance of the cavity as seen through the coupler results in the wave to be partially reflected. The backward traveling wave with current I_-, propagates back through the transmission line into port 2 of the circulator. The rf wave is directed through port 3 into a matched load with impedance Z_0. This arrangement prevents the reflected power from damaging the rf power source and is instead dissipated off as heat at the load resistor. The principle of superposition at the input coupler can be used to determine the forward and reflected waves propagating through the transmission lines. The net current $I_+ - I_-$ at the input coupler can be assumed to be linearly related to the fictitious coupler current $I_{\text{coupler}}(t)$ which appears as a source term in Eq. (1.25). On the other hand, the net voltage of the transmission line $V_+ + V_-$ is linearly related to the cavity voltage V. Assuming a phasor notation for all quantities, i.e. $I_\pm \equiv \mathcal{R}\{\tilde{I}_\pm \exp(i\omega t)\}$, $V_\pm \equiv \mathcal{R}\{\tilde{V}_\pm \exp(i\omega t)\}$ and

$I_{\text{coupler}} \equiv \mathcal{R}\{\tilde{I}_{\text{coupler}} \exp(i\omega t)\}$, we get,

$$\tilde{I}_+ - \tilde{I}_- \equiv \tilde{\alpha}_1 \tilde{I}_{\text{coupler}}\,, \tag{1.26a}$$

$$\tilde{I}_+ + \tilde{I}_- \equiv \frac{\tilde{V}_c}{\tilde{\alpha}_2 Z_0}\,, \tag{1.26b}$$

where the voltages of the traveling waves are related to the current through the impedance of the transmission line i.e $\tilde{V}_\pm = Z_0 \tilde{I}_\pm$. $\tilde{\alpha}_1$ and $\tilde{\alpha}_2$ are undetermined complex constants parameterizing the input coupler.

In the absence of input power and beam current, the stored energy of the fundamental mode gets dissipated in the walls and is emitted through the input coupler. The power emitted from the cavity through the coupler in the unpowered situation is $P_e \equiv \omega_0 U_0 / Q_{ext}$, where Q_{ext} is the **external quality factor** of the cavity. This results in an extra damping term $\omega_0 \dot{V}/Q_{ext}$ in Eq. (1.25), which is actually driven by coupler current, implying $\omega_0 \dot{V}/Q_{ext} = -(\omega_0 R/Q)\dot{I}_{\text{coupler}}$. Combining this relation with Eq. (1.26) and defining the emitted current phasor $I_e = \mathcal{R}\{\tilde{I}_e \exp(i\omega_0 t)\}$ which propagates in the backward direction (replacing $\tilde{I}_-$) gives,

$$\tilde{I}_e = \frac{\tilde{\alpha}_1 \tilde{V}_c}{\frac{R}{Q} Q_{ext}} = \frac{\tilde{V}_c}{\tilde{\alpha}_2 Z_0}\,, \tag{1.27}$$

where $V = \mathcal{R}\{\tilde{V}_c \exp(i\omega t)\}$. The unknown constants may be related to the known parameters using,

$$|\tilde{\alpha}_1|^2 Z_0 = \frac{R}{Q} Q_{ext}, \quad \tilde{\alpha}_1 \tilde{\alpha}_2 = \frac{\frac{R}{Q} Q_{ext}}{Z_0} \tag{1.28}$$

which can be obtained by combining the different expressions of emitted current in Eq. (1.27) and using the average emitted power dissipated at the load resistor, $P_e = \langle |I_e|^2 \rangle Z_0 = |\tilde{I}_e|^2 Z_0/2$, where $\langle\rangle$ represents the mean.

In the steady state, all the currents and voltages in Eq. (1.25) have a harmonic

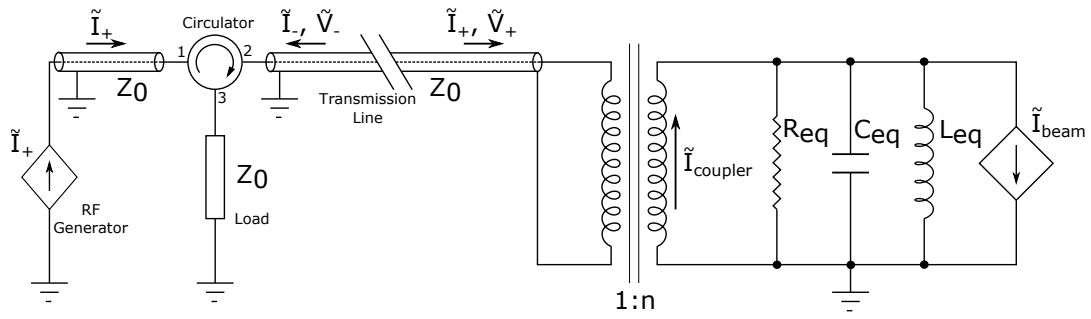

Figure 1.6: Equivalent LRC circuit for fundamental mode with a transmission line model of the rf input coupler.

time dependence. Substituting all quantities in terms of phasors yields,

$$\left\{\left(\frac{\omega_0}{\omega}-\frac{\omega}{\omega_0}\right)+\frac{i}{Q_0}\right\}\tilde{V}_c = i\frac{R}{Q}(\tilde{I}_{\text{coupler}}-\tilde{I}_{\text{beam}})\,. \tag{1.29}$$

Defining the cavity impedance as $Z_c(\omega) \equiv R/Q/\{i(\omega_0/\omega-\omega_0/\omega)+1/Q_0\}$, the coupler current required to sustain a certain cavity voltage in the presence of beam is given by,

$$\tilde{I}_{\text{coupler}} = \frac{\tilde{V}_c}{Z_c(\omega)} + \tilde{I}_{\text{beam}}\,. \tag{1.30}$$

Now combining Eq. (1.26) and (1.30) in the general powered case, gives an expression for the forward and reflected currents,

$$\tilde{I}_{\pm} = \frac{1}{2}\left[\frac{\tilde{V}_c}{\tilde{\alpha}_2 Z_0} \pm \tilde{\alpha}_1\left\{\frac{\tilde{V}_c}{Z_c(\omega)}+\tilde{I}_{\text{beam}}\right\}\right], \tag{1.31}$$

which can be used to determine power requirements during accelerator operation. It is important to note that since the dynamics of the system follows a linear second order differential equation, the same results can be obtained by analyzing an equivalent LRC circuit model as shown in Fig. 1.6. In that case, a transformer with turns ratio n is used to model the input coupler which can be related to our coupler parameters as $n \equiv |\tilde{\alpha}_1| = |\tilde{\alpha}_2|$.

Following from Eq. (1.31), the forward and reflected powers when the cavity

voltage is kept at a steady state is given by,

$$P_{\pm} = \langle |\tilde{I}_{\pm}|^2 \rangle Z_0 = \frac{Z_0}{8} \left| \frac{\tilde{V}_c}{\tilde{\alpha}_2 Z_0} \pm \tilde{\alpha}_1 \left\{ \frac{\tilde{V}_c}{Z_c(\omega)} + \tilde{I}_{\text{beam}} \right\} \right|^2 . \tag{1.32}$$

Substituting for $Z_c(\omega)$, using Eq. (1.28) and simplifying gives,

$$P_{\pm} = \frac{1}{8} \frac{R}{Q} Q_{ext} \left| \frac{1}{R/Q} \left\{ \frac{1}{Q_{ext}} \pm \frac{1}{Q_0} \pm i \Big(\frac{\omega}{\omega_0} - \frac{\omega_0}{\omega} \Big) \right\} \tilde{V}_c \pm \tilde{I}_{\text{beam}} \right|^2 . \tag{1.33}$$

The energy gain of a bunch passing through the cavity depends on the relative phase of the fundamental mode and the beam current. Hence without loss of generality, the mode voltage can assumed to be real i.e $\tilde{V}_c = V_c$, while the beam current can be represented as $\tilde{I}_{\text{beam}} = I_{\text{beam}} e^{-i\phi}$, where ϕ is the phase of the accelerating field when the beam enters the cavity. Plugging this into Eq. (1.33), using the definitions $\beta \equiv Q_0/Q_{ext}$, $Q_L^{-1} \equiv Q_0^{-1} + Q_{ext}^{-1}$ and simplifying gives,

$$P_{\pm} = \frac{V_c^2}{8 \frac{R}{Q} Q_L^2} Q_{ext} \left[\left\{ \frac{1 \pm \beta}{1 + \beta} + \frac{I_{\text{beam}} \frac{R}{Q} Q_L \cos\phi}{V_c} \right\}^2 + \left\{ - \frac{I_{\text{beam}} \frac{R}{Q} Q_L \sin\phi}{V_c} + Q_L \Big(\frac{\omega}{\omega_0} - \frac{\omega_0}{\omega} \Big) \right\}^2 \right]. \tag{1.34}$$

The forward power P_+ required to operate the cavity in steady state thus depends on many factors which can be optimized to increase efficiency of rf accelerating systems.

The surface resistance R_s of a superconductor at the operating fields determines the amount of heat which needs to be pumped away from the cavity. Since SRF cavities are usually kept at at liquid Helium temperatures, pumping the heat away takes much more electrical power than the amount of heat being pumped. Hence increasing the intrinsic quality factor Q_0 of cavities is an important goal towards making SRF accelerators more efficient.

The amount of rf power used to sustain the accelerating gradient depends on

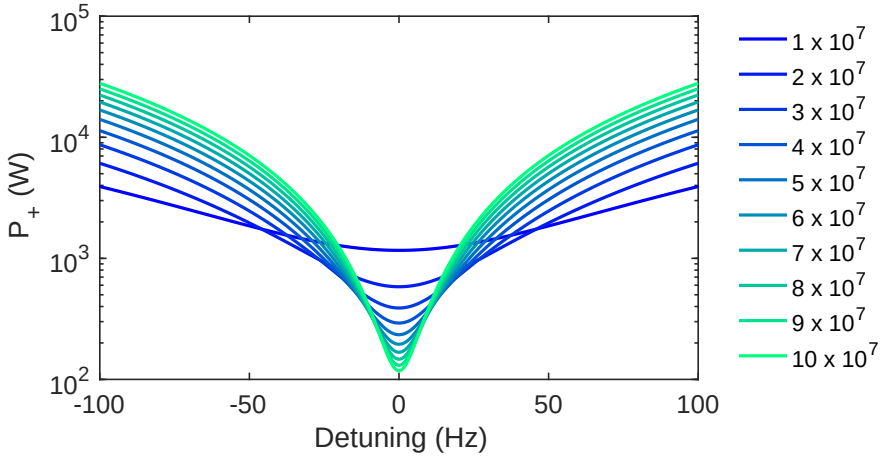

Figure 1.7: Forward power required to sustain $V_c = 6$ MV as a function of detuning in the Cornell 7-cell cavity under various values of Q_{ext}.

a variety of factors other than dissipation. In accelerators, where the beam current is small, or the net energy transferred to the beam is negligible, the forward power required according to Eq. (1.34) reduces to,

$$P_+ = \frac{V_c^2}{8\frac{R}{Q}Q_L^2} Q_{ext}\left[1 + Q_L^2\left(\frac{\omega}{\omega_0} - \frac{\omega_0}{\omega}\right)^2\right]. \tag{1.35}$$

If the resonance frequency of the fundamental mode matches the operating frequency of the accelerator, the average forward power required may be reduced by increasing the external quality factor of the input coupler. For vacuum tube power amplifiers such as Klystrons, this does not necessarily amount to a reduction in total power consumption since the electrical power required is approximately independent of the rf power generated which makes these sources inefficient for medium power applications. In contrast, solid state power amplifiers capable of delivering tens of kilo-watts are much more efficient only drawing electrical power proportional to the rf power generated. Consequently, the advent of solid state amplifiers at the relevant frequency range makes increasing Q_{ext} an attractive choice.[Marchand et al., 2007] However, SRF cavities are

subject to mechanical deformations causing transient changes in their resonance frequency, also called *detuning* $\delta f \equiv f - f_0$. Sustaining a given accelerating gradient at the operating frequency in the presence of detuning requires additional forward power as shown in Fig. 1.7. Suppression of detuning plays an important role in accelerators operating with relatively high Q_L and is explored in Chap. 2.

1.4 Energy Recovery Linacs

Continuous high-current bright beams are becoming increasingly relevant with many applications including hadron cooling[Ben-Zvi and Ptitsyn, 2015], light sources[Socol, 2013, Krafft and Priebe, 2010], various particle physics experiments employing internal targets[Balewski et al., 2014, Grieser et al., 2018, Pellegrini et al., 2015] in addition to industrial applications such as lithography [Nakamura et al., 2017] and isotope production.[Starovoitova et al., 2014] Achieving multi mega-watt beam powers in a Linac configuration, requires rf sources capable of delivering the full beam power which is infeasible in most cases. While the cooling requirements can be reduced substantially by using SRF cavities with high intrinsic quality factors, the full beam power still needs to be supplied. On the other hand, ERLs can provide high beam powers while consuming a lot less rf power.[Ben-Zvi, 2016] ERLs achieve this efficiency by recovering a large fraction of the energy from the accelerated beam itself. Apart from a few exceptions[Konoplev et al., 2017], notably the first ERL proposed by Maury Tigner[Tigner, 1965], energy recovery is most commonly achieved in a racetrack topology[Neil et al., 2006, Akemoto et al., 2018, Shevchenko et al., 2019, Arnold

et al., 2020, Bartnik et al., 2020]. In a racetrack design, the used beam is recirculated through a straight section containing the accelerating main linac. The used high energy beam enters the rf cavities in the decelerating phase, which decelerates the beam and transfers the energy back into the cavities. Acceleration can be done over multiple turns to boost the highest energy, even while extracting a modest one turn energy gain from the accelerating main linac. SRF ERLs thus provide an energy efficient platform for achieving moderate energy high-current continuous bright beams.

There are several metrics quantifying the efficiency of the energy recovery process. One metric known as the *rf to beam multiplication factor*, κ[Merminga et al., 2003] is defined as the ratio of the amount of power contained in the beam, P_{beam} to the total amount of rf power used by all the accelerating cavities in order to sustain the beam. This figure of merit can be represented as,

$$\kappa \equiv \frac{P_{\text{beam}}}{P_{rf}} \sim \frac{I_{inj}\mathcal{E}_{\text{max}}}{I_{inj}\mathcal{E}_{\text{inj}} + \sum_m P_{+,m}}, \tag{1.36}$$

where I_{inj} is the beam current into the ERL with energy $\mathcal{E}_{\text{inj}}$, $\mathcal{E}_{\text{max}}$ is the maximum energy of the recirculating beam and $\sum_m P_{+,m}$ is the total forward power consumed by all the cavities in the main linac. If the ERL is phased for perfect average energy recovery, the power required is dominated by resonance detuning as evidenced from Fig. 1.7. While this metric gives an overall picture of power consumption and efficiency, it does not explicitly quantify the amount of energy recovered from the beam during operations. The *power balance efficiency* ϵ_P of an ERL is given by,

$$\epsilon_P = 1 - \frac{P_b^{\text{ER}}}{P_{b,\uparrow}}, \tag{1.37}$$

where $P_b^{\text{ER}} = \sum_m (P_{+,m}^{\text{ER}} - P_{-,m}^{\text{ER}})$ is the total rf power provided to the beam from

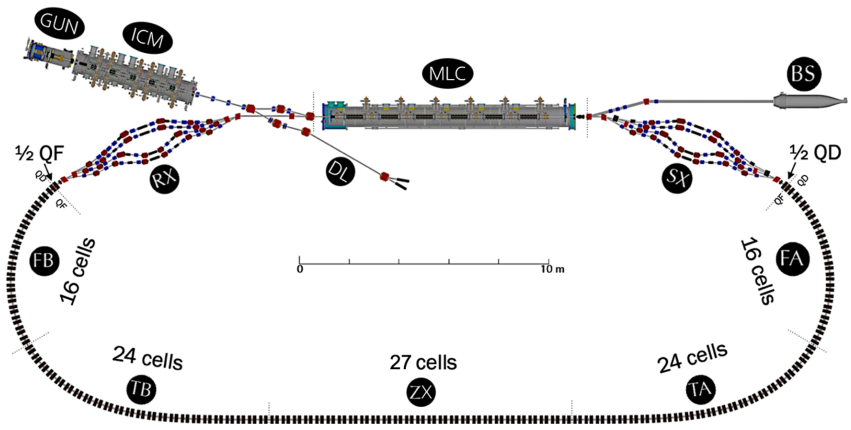

Figure 1.8: The layout of CBETA[Bartnik et al., 2020] showing the major components: the photo-injector (GUN), SRF booster linac (ICM), main linac (MLC), NS FFA re-circulation arc (FA, TA, ZX, TB, FB) and the beam stop (BS).

the rf cavities during energy recovery operation. While $P_{b,\uparrow} = \sum_m (P^{\uparrow}_{+,m} - P^{\uparrow}_{-,m})$ represents the total rf power provided to the beam only during the acceleration passes in the ERL. The power balance efficiency accounts for the actual power lost due to incorrect phasing and due to beam loss in the re-circulation passes.

The Cornell-BNL ERL Test Accelerator (CBETA) is the first superconducting ERL to demonstrate multi-turn energy recovery and consequently has a high rf to beam multiplication factor. The floor plan of this accelerator is shown in Fig. 1.8. The photo-injector along with the SRF booster linac generates a $\mathcal{E}_{\text{inj}} = 6$ MeV electron beam with a design current of $I_{inj} = 40$ mA.[2] The injected beam then gets accelerated by the main linac 4 times gaining about 36 MeV in each pass to a final energy of $\mathcal{E}_{\text{max}} = 150$ MeV. In each pass, the beam recirculates through a Non-Scaling Fixed Field Alternating (NS FFA) return loop constructed using permanent magnets.[Berg et al., 2018] At the highest energy pass,

[2] At the time of writing, the maximum current reached during the course of commissioning CBETA is 60 μA in a 1-turn configuration.Gulliford et al. [2020]

the path length of the beam has an additional 2.5 rf periods to offset the bunches into the decelerating phase of the main linac. The beam gets decelerated in the subsequent 4 passes and is finally transported into a beam stop. This dissertation discusses multiple aspects of commissioning the main linac for CBETA.

1.5 Overview of this Dissertation

The development of CBETA, the first multi-turn SRF ERL is a significant advance towards more efficient sources of bright high current electron beams. The main linac used in CBETA incorporates six 7-cell SRF cavities made of Niobium with a typical intrinsic quality factor of 2×10^{10}. These cavities are operated with a typical external quality factor of 6×10^7 which greatly reduces average power consumption and allows the use of 5 kW solid state amplifiers to sustain stable field in each cavity. However, as explained earlier in this chapter, this greatly increases the sensitivity of the system to resonance detuning. Chapter 2 is a reproduction of the manuscript Banerjee et al. [2019] which explores the active suppression of detuning due to external vibrations coupling to the SRF cavities. Chapter 3 details the commissioning process for the main linac, discussing various steps and documenting the performance of the main linac including the power balance efficiency measured during high current operations. Chapter 4 explores the interaction between the beam and the accelerating field of the main linac cavities in order to establish best practices for future high current operation.

The use of high Q_0 SRF cavities for energy recovery can further contribute to efficiency by reducing the amount of electrical power spent on refrigeration. Doped Niobium, engineered thin film structures and Niobium-Tin (Nb_3Sn) are emerging as new materials which promise to operate with much lower dissipation at the operating gradient. However, the maximum fields reached in experiments on materials such as Nb_3Sn have been limited by thermal runaway at fields much lower than the predicted superheating field. Chapter 5 describes the design and operation of a dynamic temperature mapping system capable of imaging sites of local heating on the surface of SRF cavities, hence providing a new window to study the dynamics of heating on cavities built with novel materials of low surface resistance.

Chapter 6 discusses the conclusions of the research presented in this dissertation and proposes future directions to improve on this work.

CHAPTER 2

MICROPHONICS SUPPRESSION

Operation of SRF cavities with high loaded quality factors is becoming increasingly preferred for applications which involve low beam loading including ERLs. Vibration induced microphonics detuning poses a major operational bottleneck in these low bandwidth systems, adversely affecting field stability. Besides passive measures of mitigating the vibration sources, modern SRF cavities are also attached to fast tuners incorporating piezo-electric actuators. This chapter demonstrates the narrow band active noise control algorithm for realizing active resonance control. We further derive a modification based on the Least Mean Square approach which can adaptively tune the control parameters and study its stability and performance. This chapter also discusses the experience of using passive mitigation techniques while commissioning the Main Linac Cryomodule for CBETA. We report a net reduction in peak detuning by more than a factor of 2 in its unstiffened cavities. Finally, we demonstrate stable performance of our resonance control system with consistent reduction of peak microphonics detuning by almost a factor of 2 on multiple cavities.

2.1 Introduction

Modern particle accelerators are reaching the pinnacle of efficiency using SRF cavities which are characterized by low loses arising from high intrinsic quality factors ($Q_0 \gtrsim 10^{10}$) [Padamsee, 2014]. The microwave power requirements of such SRF cavities depend on the effective beam loading and the loaded quality factor Q_L used in operation. In situations of high beam loading, they are oper-

ated with a comparatively low Q_L in order to couple the required power into the beam, such as in the LHC [Mastorides et al., 2010], CESR [Belomestnykh and Padamsee, 2001], NSLS-II [Rose et al., 2011] and many others. However, in new applications such as light source Linacs (eg. LCLS-II [Doolittle et al., 2015], XFEL [Branlard et al., 2013]) and in ERLs, high Q_L is becoming common due to the low or negligible beam loading involved. Low beam loading implies the reduction of the rf power requirements and allows the use of efficient solid state amplifiers.

However, the limited bandwidth arising from large Q_L make rf systems more sensitive to detuning when operating at a fixed frequency, as during linac operation. Transient changes in the resonant frequency of the cavity resulting from mechanical deformations change its response to the microwaves coming through the fundamental power coupler. Due to enhanced reflection of the incoming waves from a detuned cavity, more power is needed to maintain a stable field. The interaction of the field with the wall currents is one mechanism leading to mechanical deformation and is known as Lorentz Force Detuning (LFD). This leads to transient detuning as a function of the field inside the cavity and is important for pulsed rf systems. Vibrations inside cryomodules couple into the cavity walls causing transient deformations in its shape resulting in microphonics detuning. The rf power P consumed by a detuned cavity to maintain a voltage V with zero beam loading is given by, (Eq. (1.34) revisited)

$$P = \frac{V^2}{8\frac{R}{Q}Q_L}\frac{\beta+1}{\beta}\left[1+\left(\frac{2Q_L\Delta\omega}{\omega_0}\right)^2\right], \tag{2.1}$$

where Q_L is the loaded quality factor, β is the coupling factor, R/Q is the shunt impedance in circuit definition and $\Delta\omega$ is the detuning of the SRF cavity. Hence, the maximum voltage which can be stably sustained in a cavity depends on the peak microphonics detuning and is constrained by the peak forward power

available from the amplifiers.

Suppression of peak detuning is important in machines operating with high Q_L especially in multi-turn ERLs such as CBETA, where there are tight tolerances on field stability (RMS amplitude stability of 1×10^{-4} and phase stability of 0.1°) to preserve the intrinsic energy spread of the beam. Designing cavities mechanically less sensitive to vibrations is one way of achieving this goal. Cavities fabricated with metal rings welded on to them can be designed to be less sensitive to vibrations. Depending on whether the machine will be pulsed or CW, the shape and location of the stiffening rings may be optimized to reduce the effect of LFD or increase its stiffness towards external forces respectively. [Posen and Liepe, 2012b] In this chapter, we discuss suppression of the vibration sources and describe active compensation of microphonics detuning to reduce peak power consumption.

In the next section, we describe the design and operation of fast tuners while modeling them as a linear time invariant system and further explore their nonlinear behavior. Using the linear model, we develop a Least Mean Square (LMS) control system based on narrow band Active Noise Control to command the piezo-electric actuators and analyze its performance and stability. Next, we catalog the microphonics sources found while commissioning the Main Linac Cryomodule (MLC) used in CBETA and the measures taken to mitigate them. We then report on the results of using the active control algorithm during rf operations.

2.2 Fast Tuner

Mitigation of vibration sources is the preferred method of suppressing microphonics, however an active resonance control mechanism is equally important. By further reducing peak detuning, it improves the margin of power consumption with respect to the maximum capability of the microwave amplifier. It also provides an emergency mitigation mechanism against new sources of microphonics until they are found and suppressed. Active control of microphonics requires the use of fast tuners with acoustic response time scales such as the one used in CBETA. [Eichhorn et al., 2014] While a stepper motor drives the slow movement of the tuner over a large range, the piezo-electric actuators drive fast movement with a range of 2 kHz [Posen and Liepe, 2012a] which is almost 100 times the operating bandwidth of the cavity. The response of the cavity resonance frequency to voltages applied to the actuator greatly influences the design of the active resonance control system.

2.2.1 Linear Response

A Linear Time Invariant (LTI) response model can be used to describe the dynamics of the tuner for small excitations of the piezo-electric actuator. In the time domain, the change in resonant frequency $\delta f_{\text{tuner}}(t)$ of the cavity may be written as a convolution of the actuator voltage $u_{\text{pz}}(t)$ with an impulse response function $\tau(t)$ as follows,

$$\delta f_{\text{tuner}}(t) = \int_0^t \tau(t - t')u_{\text{pz}}(t')\text{dt}' \tag{2.2}$$

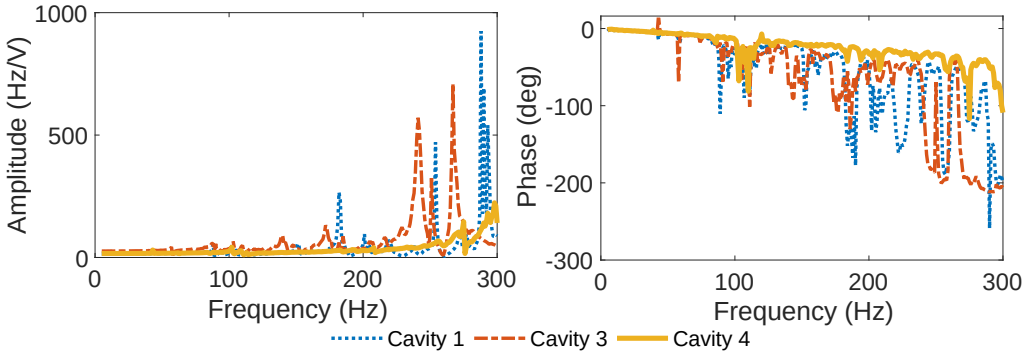

Figure 2.1: Tuner response amplitude and phase as functions of excitation frequency for three cavities of the main linac in the CBETA project.

Applying the Fourier transform on both sides of this equation we obtain,

$$\delta \tilde{f}_{\text{tuner}}(\omega) = \tau(\omega)\tilde{u}_{\text{pz}}(\omega) \tag{2.3}$$

where $\delta \tilde{f}_{\text{tuner}}(\omega)$ and $\tilde{u}_{\text{pz}}(\omega)$ are the Fourier transforms of detuning and voltage respectively. $\tau(\omega)$ is the frequency domain tuner transfer function which encodes both the amplitude of the response and the phase shift generated by the tuner. We measured the transfer function at each frequency by exciting the actuator using sine waves of different amplitudes. A linear fit of the response phasor as a function of amplitude isolates the tuner response from the background microphonics at that frequency. Using this procedure, we obtained the response of the tuner for frequencies between 5 Hz and 300 Hz which corresponds to most of the vibrations in the main linac cryomodule used in CBETA.

The transfer functions measured on three cavities of the main linac in CBETA are shown in Fig. 2.1. All the transfer functions show a region of flat amplitude and linear phase response in the range of low frequencies up to 30 Hz; this makes the use of simple algorithms like proportional integral control feasible for attenuating low frequency microphonics. The large peaks in amplitude correspond to resonances and they are accompanied by large swings in the phase

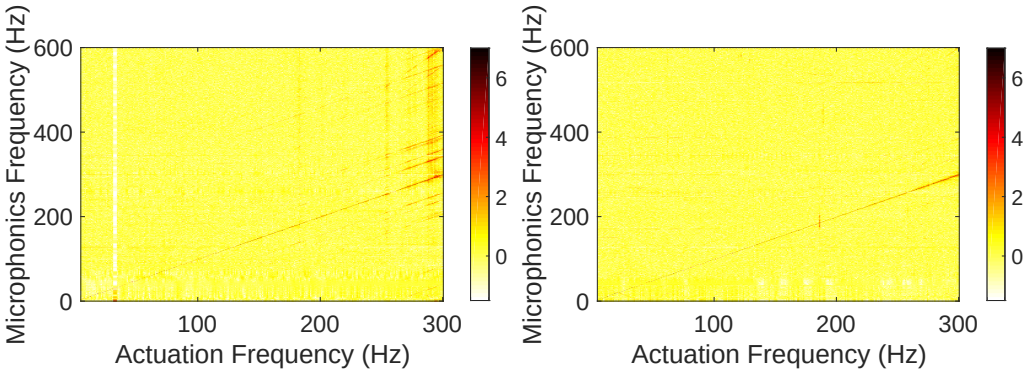

Figure 2.2: Spectral response of tuners to single frequency sinusoidal excitations in two cavities (left:unstiffened and right:stiffened) of the main linac used in the CBETA project.

response of the tuner; this limits feedback control at these frequencies. The measurements also verify one of the design goals of stiffening cavities, shifting the lowest mechanical eigenmode to a higher frequency. The transfer function data can be used to construct a LTI model of the tuner and is used to analyze the stability of the control algorithm used for resonance control.

2.2.2 Non-linear response

The assumption of linearity is dependent on the linearity of the piezo-electric effect, the stress strain curves and damping mechanisms in the materials involved. Although the stress strain curve and the piezo-electric effect are reasonably linear in the regime of use, slight hysteresis is generally observed in resonant frequency as the applied voltage is cycled from 0 V to high voltage back to 0 V. [Posen and Liepe, 2012a, Pischalnikov et al., 2015, Cichalewski et al., 2015] This implies that some non-linearity is present in the system and we should verify its magnitude. The appearance of multiple vibration frequencies even in the presence of a single tone excitation is a simple indicator of non-linear dynam-

ics.[Elliott et al., 2015] We measure the power spectrum of detuning for different frequencies of excitation of the tuner and subtract the contribution from the ambient microphonics present in the system to yield an approximate spectral response function.[1] Figure 2.2 illustrate some examples of spectral responses. The plots show the logarithm of power spectra (in color) of tuner response as functions of actuation frequency f_{pz} on the x-axes and frequency of detuning f_{detuning} on the y-axes. The white line on the left panel at the actuation frequency of 30 Hz indicates an absence of valid detuning data due to a rf trip during the measurement. The linear response shows up as a line with slope of 1, i.e. the frequency of excitation equals the major frequency component of detuning. However, the plot also shows evidence of higher order responses in the form of additional frequencies in the detuning spectrum.

We can use the straight lines observed in the plots to estimate the order of non-linearity present in the system and gain some insight into its source. In general, the frequencies present in non-linear responses of a dynamical system to a sinusoidal excitation can be written as,

$$f_{\mathrm{detuning}} = m f_{\mathrm{pz}} + \sum_i n_i f_{\mathrm{vib,i}} \tag{2.4}$$

where f_{detuning} and $f_{\mathrm{vib,i}}$ are the frequencies present in the tuner response and ambient microphonics, while f_{pz} is the frequency of excitation. m and n_i are integers, with $|m|$ representing the order of the non-linear term and the addition of vibration frequencies represent parametric behavior of the tuner dependent on external microphonics. Both the cavities show lines parallel to the linear response line indicating the presence of modulation from ambient microphonics. The unstiffened cavity further shows the second harmonic with evidence

[1] We subtract the contributions from ambient microphonics in Fig. 2.2 using a scaling relation, $\log(\chi'(f_{\mathrm{pz}}, f_{\mathrm{detuning}})) = \log(\chi(f_{\mathrm{pz}}, f_{\mathrm{detuning}})) - \frac{1}{N}\sum_i \log(\chi(f_{\mathrm{pz},i}, f_{\mathrm{detuning}}))$. $\chi(f_{\mathrm{pz}}, f_{\mathrm{detuning}})$ is the spectral power at frequency f_{detuning} when the tuner is excited with a sine wave of frequency f_{pz}.

of the $m = 2$ line near $f_{pz} = 300$ Hz. The strength of the non-linear responses appear to be a function of frequency with excitation frequencies of above 250 Hz showing the most activity. These observations suggest that we can ignore the non-linearity as long as we excite the tuner below 250 Hz which limits the bandwidth of the compensation system.

2.3 Active Noise Control

Microphonics compensation of SRF cavity detuning using fast tuners has been demonstrated using a variety of techniques. Resonance control of CW rf cavities typically rely on feedback of microphonics detuning. In this control topology, the detuning acts as an input to the controller which generates a signal for the piezo-electric actuator which in turn affects the net microphonics detuning thus closing the loop. The transfer function of the tuner system as discussed in the previous section plays an important role in designing the controller. The traditional method of Proportional-Integral feedback has been demonstrated in various machines [Conway and Liepe, 2010, Banerjee et al., 2017, Neumann et al., 2010] and is very effective when the phase response of the tuner is a monotonous function of frequency which is typical at lower frequencies ($\leq$ 10Hz). At higher frequencies, the tuner cavity system typically has mechanical eigenmodes which introduce steps in the phase response which may possibly lead to positive feedback and instability at even modest gains. Consequently, low pass filters are used to ensure stability of the PI loop but at the cost of reducing the bandwidth. Additional band pass filters may be used in parallel to attenuate certain frequency bands, however manually adjusting them while ensuring stability is inconvenient. In order to get past this limitation, arbitrary digital control filters

can be optimized specifically to compensate for a given microphonics spectrum while taking into account the exact phase response of the tuner. This has been demonstrated on the new LCLS-II cryomodules which were tested at Fermi-Lab.[Holzbauer et al., 2018]

In the methods described above, the tuner transfer function and the microphonics spectrum are first measured and the data is processed external to the rf control system and the optimal filter coefficients are then uploaded into the control system. In contrast, adaptive tuning of digital control filters inside the rf system during operations using Least Mean Squares (LMS) algorithms have also been demonstrated. In traditional LMS, an external reference signal which correlates to microphonics detuning is used as an input to a Finite Impulse Response (FIR) filter whose coefficients are updated continuously to reduce the mean square of detuning [Neumann et al., 2010]. In a different technique [Kandil et al., 2005, Rybaniec et al., 2017] based on Active Noise Control (ANC) methods, amplitude and phase of sine-waves at different frequencies are adjusted to cancel out microphonics. However, both these methods require prior measurement of the tuner transfer function which may be a function of tuner position [Posen and Liepe, 2012b] and may not stay constant over long periods of time and over multiple pressure or temperature cycles. In this chapter, we derive the narrow band ANC technique and propose a modification so that it adapts to the tuner response phase in-situ.

Microphonics detuning due to narrow band vibration sources can be well approximated by a finite series of sinusoids at different frequencies with slowly changing amplitudes and phases. This motivates the use of an algorithm which works by adjusting the amplitudes of a series of sine and cosine functions in or-

der to reduce the mean square detuning. At a particular frequency ω_m, the ideal phase of the actuator signal θ_m^{pz} is determined by not only the relative phase of external detuning with respect to the internal clock θ_m^{micro} of the control system but also the phase response ϕ_m of the actuator. The ideal actuator signal phase given by $\theta_m^{\text{pz}} = \theta_m^{\text{micro}} + \phi_m - \pi$ in principle perfectly cancels the sine wave produced by external vibrations. The phase lag ϕ_m introduced by the tuner can be assumed to be a constant when the frequency of vibrations is far from a mechanical resonance, and used as a compensation parameter in the algorithm. Using the technique of stochastic gradient descent, we derive a set of equations which updates the amplitude and phase of individual sinusoids along with online optimization of the phase parameter ϕ_m at the frequencies of vibration.

2.3.1 Derivation

Microphonics from narrow band vibration sources may be represented by a finite series of sinusoids at different frequencies with slowly changing amplitudes and phases. Hence, in the time domain, the actuator voltage $u_{\text{pz}}(t)$ can also be written as a sum of sinusoids $u_m(t)$ with frequencies ω_m and whose amplitude and phase are determined by slowly changing $I_m(t)$ and $Q_m(t)$,

$$u_{\text{pz}}(t) = \sum_m u_m(t) = \sum_m I_m(t)\cos(\omega_m t) - Q_m(t)\sin(\omega_m t) \tag{2.5}$$

The piezo-electric actuator tunes the cavity in response to this signal, the effect of the tuner being represented as a linear transfer function $\tau(\omega)$. Using a phasor notation for the individual frequencies $\tilde{A}_m(t) \equiv I(t) + iQ(t)$, we can write the total actuator voltage in terms of these phasors as $u_{\text{pz}}(t) = \sum_m u_m(t) \equiv \sum_m \mathcal{R}\{\tilde{A}_m(t)\mathrm{e}^{\mathrm{i}\omega_{\mathrm{m}}\mathrm{t}}\}$. Using this notation we write the detuning near a particular frequency as a linear

response integral

$$f_m(t) = \mathcal{R}\Big\{\frac{1}{2\pi}\int_{-\infty}^{\infty} d\omega \int_{-\infty}^{\infty} dt' \tilde{A}_m(t') e^{i(\omega_m-\omega)t'} \tau(\omega) e^{i\omega t}\Big\}, \tag{2.6}$$

where we have Fourier transformed the actuator voltage, used Eq. (2.3) which gives us $f_m(\omega) = \tilde{A}_m(\omega)\tau(\omega)$ and finally applied the inverse Fourier transform to calculate the detuning $f_m(t)$ in the time domain. Since the spectral content of microphonics detuning is assumed to be concentrated around certain frequencies, only parts of the transfer function are relevant in modeling the tuner movements.

Far from resonance, where the amplitude of the response does not strongly depend on frequency, we approximate the tuner transfer function around ω_m as

$$\tau(\omega) \simeq \tau_m^{mod} e^{-i\{\phi_m^{mod} + \frac{d\phi}{d\omega}\Big|_{\omega_m}(\omega-\omega_m)\}}, \tag{2.7}$$

where we expand the phase response up to first order. Since this approximation only applies in the neighborhood of ω_m, we impose the restriction of narrow bandwidth on $u_m(t)$, which implies $|\frac{1}{\tilde{A}_m}\frac{d\tilde{A}_m}{dt}| << \omega_m$. Using this model in Eq. (2.6) and changing the order of integration, we get

$$\begin{aligned} f_m(t) &\simeq \mathcal{R}\Big\{\int_{-\infty}^{\infty} dt' \tilde{A}_m(t') e^{i\omega_m t'} \times \frac{1}{2\pi}\int_{-\infty}^{\infty} d\omega\, \tau_m^{mod} e^{i\{-\phi_m^{mod} + \frac{d\phi}{d\omega}\Big|_{\omega_m}\omega_m\}} e^{i\omega\left(t-t'-\frac{d\phi}{d\omega}\Big|_{\omega_m}\right)}\Big\} \\ &= \mathcal{R}\Big\{\tau_m^{mod} e^{i\{-\phi_m^{mod} + \frac{d\phi}{d\omega}\Big|_{\omega_m}\omega_m\}} \int_{-\infty}^{\infty} dt' \tilde{A}_m(t') e^{i\omega_m t'} \times \delta(t - t' - \frac{d\phi}{d\omega}\Big|_{\omega_m})\Big\}, \end{aligned} \tag{2.8}$$

where the integral over ω becomes a delta function which represents the approximate time domain impulse response valid when the frequency of actuation is ω_m. Using the delta function to evaluate the convolution integral, we get

$$f_m(t) \simeq \mathcal{R}\{\tau_m^{mod} \tilde{A}_m(t - D_m^{mod}) e^{i(\omega_m t - \phi_m^{mod})}\}, \tag{2.9}$$

where we have introduced the group delay $D_m^{mod} \equiv \frac{d\phi}{d\omega}\Big|_{\omega_m}$. The effective detuning $\delta f_{comp}(t)$ of the cavity in response to the perturbation given in Eq. (2.5) is thus

given by,

$$\delta f_{\text{comp}}(t) = \delta f_{\text{ext}}(t) + \sum_m f_m(t) = \delta f_{\text{ext}}(t) + \sum_m \mathcal{R}\{\tau_m^{mod} \tilde{A}_m(t - D_m^{mod}) e^{i(\omega_m t - \phi_m^{mod})}\}, \quad (2.10)$$

where we have combined the tuner response at different frequencies and $\delta f_{\text{ext}}(t)$ is the microphonics detuning coming from external vibrations. Now we can use this model to construct a suitable cost function which can be minimized by the algorithm.

The objective of microphonics compensation is to reduce the mean square detuning of the cavity.

$$C(t_n) \equiv \frac{1}{N} \sum_{i=n-N+1}^{n} (\delta f_{\text{comp}}(t_i))^2 \quad (2.11)$$

$C(t_n)$ is the cost function at time t_n which is taken to be the expectation value of the square of detuning, approximated by a running average. The method of gradient descent relies on the gradient vector being in the direction of steepest descent on the cost surface. In parameter space, the gradient represents the normal to the constant cost surface and can be estimated using the model developed in Eq. (2.10). Following standard LMS techniques [Kuo and Morgan, 1999], we use the current sample to approximate the cost function and hence use the stochastic gradient descent approach to the optimization problem. Taking $N = 1$, we calculate the partial derivatives of the cost function with respect to the real and imaginary parts of the optimization parameter $\tilde{A}_m$ which determines the actuator voltage.

$$\frac{\partial C}{\partial \mathcal{R}\{\tilde{A}_m\}} = \tau_m^{mod} \delta f_{\text{comp}}(t_n) \cos(\omega_m t - \phi_m^{mod}), \quad \frac{\partial C}{\partial \mathcal{I}\{\tilde{A}_m\}} = -\tau_m^{mod} \delta f_{\text{comp}}(t_n) \sin(\omega_m t - \phi_m^{mod}) \quad (2.12)$$

where we have used Eq. (2.10) under the assumption that group delay D_m^{mod} is negligible with respect to the time scales with which $\tilde{A}_m(t)$ changes. The typical

group delay introduced by the modified Saclay - I tuners used in the CBETA project is less than a millisecond far from resonant frequencies while the bandwidth of the vibration sources are typically less than 1 Hz. Each iteration of the stochastic gradient descent algorithm changes the control parameter a little in the direction opposite to the gradient.

$$\tilde{A}_m(t_{n+1}) = \tilde{A}_m(t_n) - \mu_m \delta f_{\mathrm{comp}}(t_n) \mathrm{e}^{-\mathrm{i}(\omega_\mathrm{m} \mathrm{t} - \phi_\mathrm{m}^\mathrm{mod})}, \tag{2.13}$$

where we have absorbed τ_m^{mod} into μ_m, which is the adaptation rate for $\tilde{A}_m$ in the algorithm. Equation (2.5) together with (2.13) form the Active Noise Control(ANC) algorithm.

The ANC algorithm derived above is mathematically equivalent to applying a linear time invariant filter on the tuning error defined as $e(t) \equiv \delta f_0 - \delta f_{comp}$ in order to generate the actuator signal $u_m(t)$, where we use $\delta f_0 = 0$ in the presence of no beam loading. To derive the equivalent filter transfer function, we start by assuming $\tilde{A}_m(0) = 0$, and write the update rule using the phasor notation,

$$\tilde{A}_m(t_{n+1}) = \mu_m \sum_{k=0}^{n} (-\delta f_{\mathrm{comp}}(t_k)) \mathrm{e}^{-\mathrm{i}(\omega_\mathrm{m} \mathrm{t_k} - \phi_\mathrm{m}^\mathrm{mod})} \tag{2.14}$$

Combining this equation with the definition $u_m(t) \equiv \mathcal{R}\{\tilde{A}_m(t) \mathrm{e}^{\mathrm{i}\omega_\mathrm{m} \mathrm{t}}\}$, we directly relate the actuator signal to the tuning error.

$$\begin{aligned} u_m(t_{n+1}) &= \mathcal{R}\{\mu_m \mathrm{e}^{\mathrm{i}\omega_\mathrm{m} \mathrm{t_{n+1}}} \sum_{\mathrm{k=0}}^{\mathrm{n}} (-\delta \mathrm{f}_{\mathrm{comp}}(\mathrm{t_k})) \mathrm{e}^{-\mathrm{i}(\omega_\mathrm{m} \mathrm{t_k} - \phi_\mathrm{m}^\mathrm{mod})}\} \\ &= \mu_m \sum_{k=0}^{n} e(t_{n-k}) \cos(\omega_m (k+1) \Delta t + \phi_m^{mod}), \end{aligned} \tag{2.15}$$

where Δt is the sample duration, and $e(t) = -\delta f_{\mathrm{comp}}(t)$. Equation (2.15) represents a discrete convolution of the input signal with a sinusoid and is an impulse response filter. The Z-transform of the filter can be written as,

$$H_m(z) = \mu_m \sum_{k=0}^{\infty} z^{-k} \cos(\omega_m (k+1) \Delta t + \phi_m^{mod}) = \mu_m \frac{\cos(\omega_m \Delta t + \phi_m^{mod}) - z^{-1} \cos \phi_m^{mod}}{1 - 2\cos(\omega_m \Delta t) z^{-1} + z^{-2}} \tag{2.16}$$

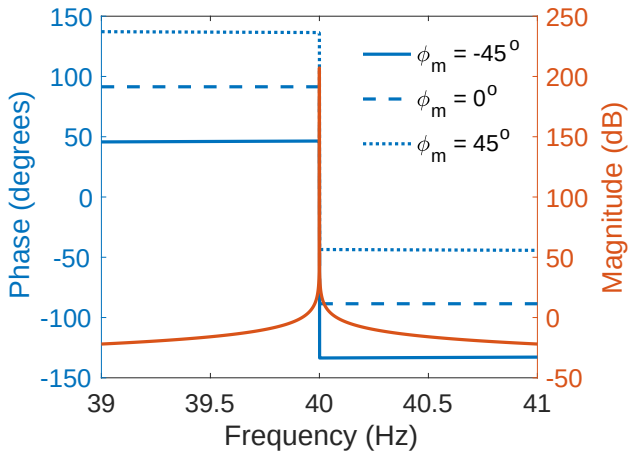

Figure 2.3: Frequency response $H_m(e^{i\omega\Delta t})$ of the control filter described in Eq. (2.15) for one mode $f_m = 40\,\text{Hz}$, $\mu_m = 10^{-4}$, $\Delta t = 0.1\,\text{ms}$ and three values of phase $\phi_m = -45°, 0°, 45°$.

The frequency response is shown in Fig. 2.3.

The control filter shows a very narrow band pass response rising to ∞ and a phase swing of 180° around the frequency ω_m. In the limit of $\omega \to \omega_m$, the filter response can be approximated by,

$$H_m(e^{i\omega\Delta t}) \approx \frac{\mu_m e^{i(-\frac{\pi}{2}+\phi_m^{\text{mod}}+\omega_m\Delta t)}}{2(\omega-\omega_m)\Delta t} \tag{2.17}$$

μ_m serves as an overall scaling factor governing the span of frequencies within which the controller-tuner system has more than unity gain and μ_m can hence be used to adjust the bandwidth of the feedback loop around the microphonics frequency. In the neighborhood of ω_m, the phase swings from $\pi/2 + \phi_m + \omega_m\Delta t$ to $-\pi/2 + \phi_m + \omega_m\Delta t$ from left to right in a discrete jump. The value of ϕ_m primarily provides a constant offset to the phase response and can be used as a knob to stabilize the feedback control loop.

2.3.2 Stability

The compensated detuning $\delta\tilde{f}_{\mathrm{comp}}(\omega)$ is the net effect of the tuner $\delta\tilde{f}_m(\omega) \equiv \tau(\omega)u(\omega)$ and the external contribution $\delta\tilde{f}_{\mathrm{ext}}(\omega)$. The tuner excitation $u(\omega) \equiv -H(\omega)\delta\tilde{f}_{\mathrm{comp}}(\omega)$ is obtained as an output of the linear controller whose frequency response is given by $H(\omega)$. From these definitions we obtain the closed loop transfer function (CLTF) of the system which provides a linear relation between the external detuning $\delta\tilde{f}_{\mathrm{ext}}(\omega)$ and the compensated detuning $\delta\tilde{f}_{\mathrm{comp}}(\omega)$ in frequency space.

$$C(\omega) \equiv \frac{\delta\tilde{f}_{\mathrm{comp}}(\omega)}{\delta\tilde{f}_{\mathrm{ext}}(\omega)} = \frac{1}{1 + \sum_m H_m(\omega)\tau(\omega)} = \prod_m \frac{1}{1 + H_m(\omega)\tau(\omega)}, \tag{2.18}$$

where the sum of all the filters $H(\omega) \equiv \sum_m H_m(\omega)$ acts as a comb with it's frequency response amplitude remaining small except for the neighborhood of ω_m. This lets us write the transfer function as a product, since $|H_m(\omega)H_n(\omega)\tau^2(\omega)| \approx 0 \quad \forall m \neq n$. In a theoretical situation, when all the microphonics detuning is generated by pure sine waves whose frequencies are exactly ω_m, the controller works perfectly to compensate for all microphonics. Figure 2.4 demonstrates this by showing that $|C(\omega)|$ equals 0 at ω_m, where $\delta f_{\mathrm{ext}}(\omega)$ only consists of a sine wave at exactly ω_m. However real microphonics signals have finite bandwidth spectral modes and the performance of feedback control is determined by the combined response of the controller and the tuner over all of frequency space. In the limit of the response of each filter being much greater near its pass-band than its nearest neighbors, we can approximate the complete tuner transfer function $\tau(\omega)$ with tuner transfer function models $\tau_m(\omega) \equiv \lim_{\omega\to\omega_m} \tau(\omega)$ at each compensation frequency ω_m.

$$C(\omega) \sim \prod_m \frac{1}{1 + H_m(\omega)\tau_m(\omega)} \tag{2.19}$$

Figure 2.4 shows the shape of one such isolated function and illustrates how adjusting ϕ_m can lead to an asymmetric response, attenuating vibrations on one

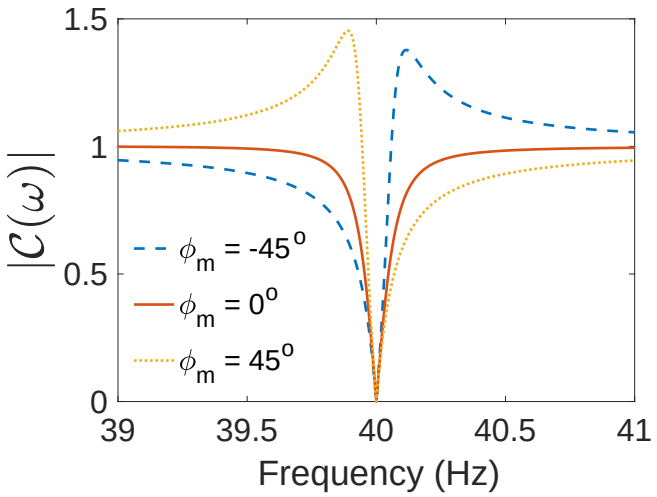

Figure 2.4: Magnitude of closed loop transfer function in frequency domain with $f_m = 40\,\text{Hz}$, $\mu_m = 10^{-4}$, $\Delta t = 0.1\,\text{ms}$ for different choices of ϕ_m when $\tau(\omega) = 1$.

side and amplifying the other. Further, the closed loop stability all of the individual contributions with index m can be a sufficient condition for the stability of the entire system.

In practice, we estimate the values of μ_m and ϕ_m^{mod} based on the measured tuner transfer function in order to configure the controller. If these guesses are close to the actual behavior of the tuner near ω_m, then the controller yields good performance and is stable. Approximating the *actual* tuner transfer function by $\lim_{\omega\to\omega_m} \tau(\omega) = \tau_m \mathrm{e}^{-\mathrm{i}\{\phi_\mathrm{m}+\mathrm{D_m}(\omega-\omega_\mathrm{m})\}}$, we can determine the range of values of μ_m and ϕ_m^{mod}, which leads to stable performance of the narrow band ANC algorithm.

We can analyze the stability of the feedback loop using the open loop transfer function $\mathcal{U}_m(\omega) \equiv H_m(\omega)\tau(\omega)$. The phase response ϕ_{OL} of $\mathcal{U}_m(\omega)$ around the

frequency ω_m is given by,

$$\phi_{\mathrm{OL}} = \begin{cases} \frac{\pi}{2} + \phi_m^{mod} + \omega_m \Delta t - \phi_m - (\omega - \omega_m) D_m, & \text{for } \omega \leq \omega_m \\ -\frac{\pi}{2} + \phi_m^{mod} + \omega_m \Delta t - \phi_m - (\omega - \omega_m) D_m, & \text{for } \omega > \omega_m \,, \end{cases} \tag{2.20}$$

where ϕ_m^{mod} is the compensation parameter used in the control algorithm. The ANC response function [Eq. (2.16)] does not have any poles in the positive half of the complex plane. Using this information, the Nyquist stability criterion dictates that instability can only happen if $\mathcal{U}_m(\omega)$ encircles the point -1 in the complex plane. This occurs when $\mathcal{U}_m(\omega)$ crosses the negative real axis while $|\mathcal{U}_m(\omega)| \geq 1$. The band of frequencies within which instability may occur is given by,

$$\omega_m - \frac{\mu_m \tau_m}{2\Delta t} < \omega < \omega_m + \frac{\mu_m \tau_m}{2\Delta t} \tag{2.21}$$

The control loop is stable when we avoid positive feedback inside the above domain i.e. $\phi_{\mathrm{OL}}(\omega_m - 0.5\mu_m\tau_m/\Delta t) < \pi$ and $\phi_{\mathrm{OL}}(\omega_m + 0.5\mu_m\tau_m/\Delta t) > -\pi$. This gives us a range of possible values for ϕ_m^{mod}.

$$-\frac{\pi}{2} + \frac{\mu_m \tau_m D_m}{2\Delta t} - \omega_m \Delta t + \phi_m < \phi_m^{mod} < \frac{\pi}{2} - \frac{\mu_m \tau_m D_m}{2\Delta t} - \omega_m \Delta t + \phi_m \tag{2.22}$$

The center of the above range, $\phi_m^{\mathrm{center}} = \phi_m - \omega_m \Delta t$ compensates for the phase lag from the tuner at frequency ω_m and gives us the maximum margin on ϕ_m^{mod}. The span of acceptable values of ϕ_m^{mod} depends on not only the tuner behavior but also the adaptation rate μ_m. To ensure that the range given by Eq. (2.22) is not a null set, we put an upper bound on μ_m.

$$\mu_m < \frac{\pi \Delta t}{D_m \tau_m} \tag{2.23}$$

These calculations assume that neighboring frequencies of the comb are far away so that their response amplitudes are much less than unity at the next

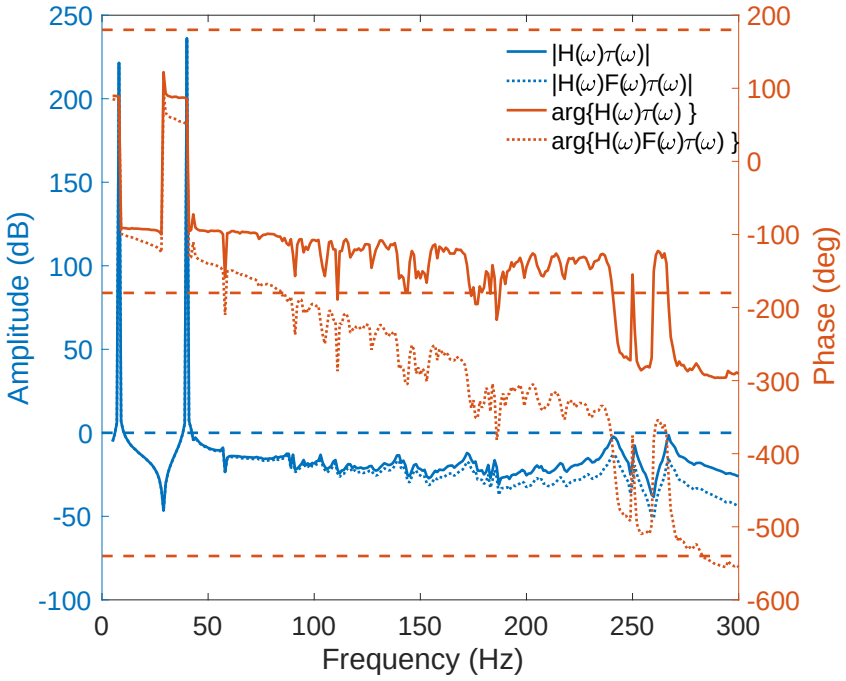

Figure 2.5: Bode plot for the mechanical open loop transfer function $\mathcal{U}(\omega) \equiv H(\omega)\tau(\omega)$ of an unstiffened cavity inside the CBETA main linac showing both the amplitude and phase in blue and orange respectively.

frequency i.e. $|\mathcal{U}_{m-1}(\omega_m)| = |\tau(\omega_m)H_{m-1}(\omega_m)| << 1$. This gives us a crude limit on the distance between nearest neighbors as,

$$|\omega_m - \omega_{m-1}| >> \frac{\mu_{m-1}\tau_m}{2\Delta t}\,, \tag{2.24}$$

hence constraining the spacing of the different frequencies we can compensate. Detailed calculations involving the complete tuner transfer function and the array of band pass filters are required to fully analyze the stability of the control system.

The complete stability analysis of the ANC system involves assessing the open loop transfer function $\mathcal{U}_m(\omega)$ over all frequencies using a Bode plot. Figure 2.5 shows an example of using the compensation system on an unstiffened cavity used in the main linac of the CBETA project. The solid lines represent

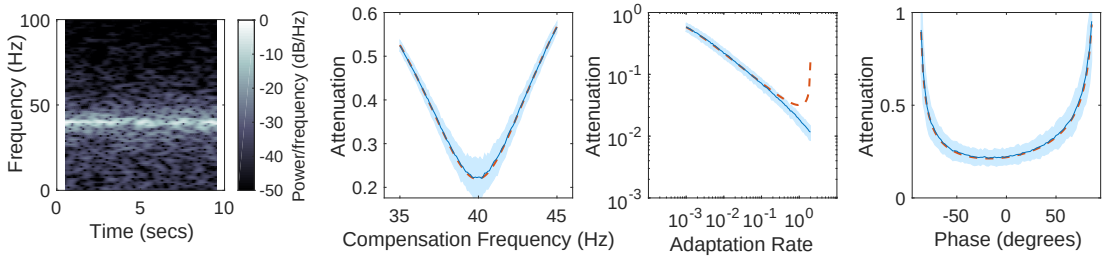

Figure 2.6: Simulation results of using ANC with an ideal tuner. From the left, the first panel shows the spectrogram of simulated vibrations and the others show dependence of the attenuation on frequency ω_m, adaptation rate μ_m and controller phase ϕ_m^{mod} respectively.

the effect of the ANC algorithm applied to frequencies 8 Hz and 40 Hz, illustrated by the notches in amplitude and expected phase swings of 180° at these frequencies. The open loop phase stays between −180° and 180° (orange dashed lines) for gains above 0 dB showing that the system is stable near these frequencies. The phase margins i.e the distances from the −180° line when the amplitude crosses unity gain (0 dB - blue dashed line) are 80° and 90° at 8 Hz and 40 Hz respectively as seen from the plot of $\phi_{\text{OL}} = \arg\{\text{H}(\omega)\tau(\omega)\}$ in Fig. 2.5. However, the gain seems to be close to 0 dB near the tuner resonances at frequencies around 250 Hz, when ϕ_{OL} crosses the −180° mark with a gain margin $\lesssim$ 2 dB. This prompts the use of a low pass filter with frequency response $F(\omega)$ to attenuate the transfer function at these frequencies as shown by the dotted lines of Fig. 2.5. The analysis illustrates the effect of tuner resonances far from the compensation frequencies ω_m signaling the need for additional filtering to ensure stability of the system.

2.3.3 Performance on a Single Resonance

The performance of the controller in suppressing microphonics detuning depends on the vibrating components. Assuming that the microphonics is generated by resonant processes for example through thermo-acoustic instabilities or through white noise excitations, the ensemble averaged power spectrum $\langle|\delta\tilde{f}_{\text{ext}}(\omega)|^2\rangle_{\text{E}}$ of mechanical eigenmodes is given by,

$$\langle|\delta\tilde{f}_{\text{ext}}(\omega)|^2\rangle_{\text{E}} \equiv \sum_v \frac{\Gamma_v^2}{\{1-(\frac{\omega}{\omega_v})^2\}^2 + (\frac{\omega}{Q_v\omega_v})^2}\,, \tag{2.25}$$

where ω_v, Q_v and Γ_v are the frequencies, quality factors and strengths of microphonics detuning. Using this prescription, we simulate the performance of the controller on vibrations generated by exciting a simple harmonic oscillator with frequency 40 Hz and quality factor 50 with Gaussian white noise from a random number generator with an arbitrary seed. The first panel of Fig. 2.6 shows a spectrogram of detuning used to test the ANC controller. Assuming that the tuner transfer function, $|\tau(\omega)| = 1$ over all frequencies, the compensated detuning in each iteration is $\delta f_{\text{comp}}(t_n) = \delta f_{\text{ext}}(t_n) + u_{\text{pz}}(t_{n-1})$. We simulate the mechanical performance of the controller-tuner system by iterating through Eq. (2.13) and (2.5) to calculate the control signal $u_{\text{pz}}(t_n)$ to the actuator, while the sampling and iteration process generates a group delay $D = 2\Delta t$. The performance of the system is calculated as $\sqrt{\langle\delta f_{\text{comp}}^2\rangle_t/\langle\delta f_{\text{ext}}^2\rangle_t}$ which represents attenuation of the microphonics detuning δf_{ext} excited by vibrations. To account for the randomness of the vibration signal, we perform the ensemble average of attenuation over 100 simulations using different random number seeds, each lasting for a duration of 10 seconds. While the average of attenuation is shown as the thin blue line, its 2σ confidence bounds are shaded light blue. We compare the results of the time domain simulations with the expected performance (orange dashed

line) of the algorithm calculated semi-analytically using the closed loop transfer function [Eq. (2.19)] along with the filter response in Eq. (2.16).

Figure 2.6 shows the simulated performance of the ANC algorithm under varying compensation parameters. The results show that the controller performs its best on average when $\omega_m = \omega_v$, with attenuation progressively getting worse as we go farther away from ω_v. The attenuation shows an asymmetric dependence on ϕ_m^{mod} about 0° reaching a minimum at some non-zero value. Finally, μ_m represents the gain in the system and compensation is expected to get better with larger gain up to the limit given by Eq. (2.23) beyond which the system becomes unstable. The expected attenuation estimated from the semi-analytical calculation clearly diverges at $\mu_m \gtrsim \pi/2$, however the results from the numerical simulations don't agree. In practice the maximum gain of the system will depend on the exact response of the tuner, especially the group delay. These simulations guide us on how to choose parameters of the ANC during operations.

2.3.4 Phase Adaptation

The compensation performance of a controller with fixed parameters is dependent on variations in the response of the tuner and fluctuations of the microphonics spectrum. The tuner response may vary from day to day due to pressure variation in the Helium bath while the vibration mechanism may also change frequency as a function of time. The controller as described in the previous section will not be able to adapt to such changes, which might limit performance in a dynamic environment. The simulation results in Fig. 2.6 suggests

that attenuation is a monotonously decreasing function of gain μ_m, with the system becoming unstable beyond a threshold. An adaptive algorithm to optimize for the value of μ_m might tend to drive the system towards instability. However, the controller frequency ω_m and phase ϕ_m^{mod} have positions where attenuation is minimum within the range of values which satisfy the stability conditions. Consequently, adapting ω_m and ϕ_m^{mod} to a changing excitation could potentially make the algorithm more robust, while making it easier to operate in practice since it would optimize itself.

The optimization of the ANC system translates to finding the minimum of the mean square of detuning $\langle \delta f_{\text{comp}}^2 \rangle$ with respect to the phases ϕ_m^{mod} and the frequencies ω_m. We can implement this optimization in the frequency domain using Parseval's theorem and Eq. (2.18) to establish a relation with $H_m(\omega)$.

$$\langle \delta f_{\text{comp}}^2 \rangle_t \propto \int_{-\infty}^{\infty} |\delta \tilde{f}_{\text{comp}}(\omega)|^2 \mathrm{d}\omega = \int_{-\infty}^{\infty} \left| \frac{\delta \tilde{\mathrm{f}}_{\text{ext}}(\omega)}{1 + \sum_{\mathrm{m}} \mathrm{H_m}(\omega)\tau(\omega)} \right|^2 \mathrm{d}\omega \tag{2.26}$$

We can use this expression with any numerical optimizer to calculate the best values for the ANC parameters provided that the detuning spectrum $\tilde{f}_{\text{ext}}(\omega)$ and the tuner transfer function $\tau(\omega)$ are known. We simulate the performance of this approach by exciting vibrations at 40 Hz in δf_{ext} with varying quality factors Q_v and different μ_m in H_m. We use the measured $\tau(\omega)$ from un-stiffened cavity 3 whose transfer function was shown in Fig. 2.1. Figure 2.7 shows the results from a simplex optimizer as orange dashed lines, with panels (b) and (d) showing the optimum values of phase ϕ_m^{opt} as a function of quality factor Q_v and adaptation rate μ_m respectively. Panels (a) and (c) show the minimum attenuation achieved by the optimizer.

In order to implement this optimization as a LMS scheme, we will need to adapt to changing characteristics of microphonics detuning in δf_{ext} and also

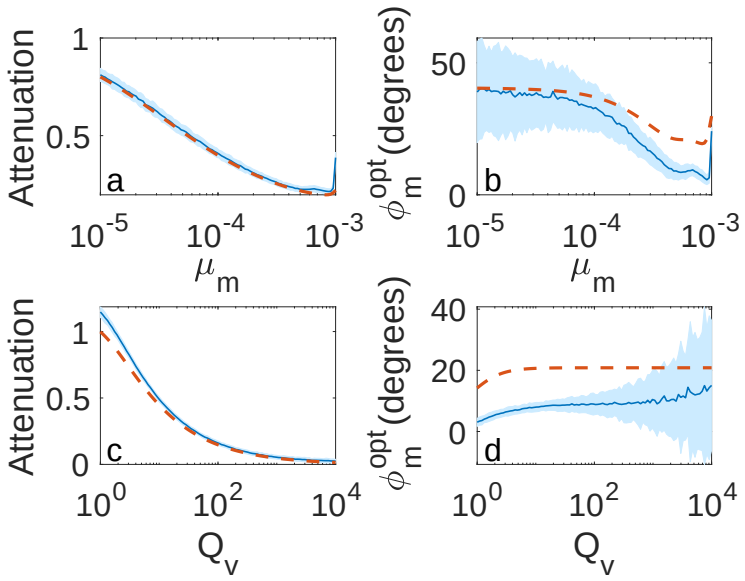

Figure 2.7: Comparison of controller phase optimization for different gains and quality factors of vibration. (a) and (c) show the best attenuation reached while (b) and (d) shows the optimum phase as functions of μ_m and Q_v respectively.

measure tuner response $\tau(\omega)$ over the relevant frequencies at the same time. We derive an alternative algorithm which achieves this by solely adapting the controller phase ϕ_m^{mod} in order to minimize the cost function through gradient descent, and at the same time, make the controller more robust to changes in the tuner. The partial derivative of the cost function given in Eq. (2.11) with respect to ϕ_m^{mod} is given by,

$$\frac{\partial C}{\partial \phi_m^{mod}} = 2\tau_m \delta f_{\mathrm{comp}}(t_n)\, \mathcal{R}\{\tilde{A}_m(t_n) \mathrm{e}^{\mathrm{i}(\omega_m t_n - \phi_m^{\mathrm{mod}}(t_n) - \pi/2)}\}\,. \tag{2.27}$$

This gives us the update rule

$$\phi_m^{mod}(t_{n+1}) = \phi_m^{mod}(t_n) - \eta_m \delta f_{\mathrm{comp}}(t_n)\, \mathcal{R}\{\tilde{A}_m(t_n) \mathrm{e}^{\mathrm{i}(\omega_m t_n - \phi_m^{\mathrm{mod}}(t_n) - \pi/2)}\}, \tag{2.28}$$

where η_m is the adaptation rate for ϕ_m^{mod}. Figure 2.7 also shows the results from simulations of this algorithm with microphonics at frequency $f_v = 40\,\mathrm{Hz}$, with a tuner response modeled on the same measured $\tau(\omega)$ for MLC cavity 3. We

initialized the simulations with the known microphonics frequency $f_m = f_v = 40\,\text{Hz}$, an initial guess for the tuner phase $\phi_m^{mod} = 0$ and phase adaptation rate $\eta_m = -0.0001$. We set the controller gain to $\mu_m = 0.0006$ for the simulations with varying Q_v, and set the quality factor of vibration source to $Q_v = 50$ for simulations with different μ_m. The thin blue lines representing the ensemble average over 80 simulations clearly show the LMS adapted phase deviates from the simplex optimization outlined in the previous paragraph. The shaded blue region represents the 2σ confidence bounds. The difference between the in-situ and the offline optimizations arises from the approximate model [Eq. (2.10)] of compensated detuning which we used to construct the partial derivative where the group delay and higher order terms in Eq. (2.7) were neglected. However, the attenuation obtained from gradient descent closely matches the ideal result, thus demonstrating the efficacy of this method.

2.4 Results

CBETA uses two SRF cryomodules, one for the injection system and the other used to execute energy recovery. The injector cryomodule[Liepe et al., 2012, 2011] consists of five 2-cell SRF cavities[Liepe et al., 2010] and is configured to provide 6 MeV of energy gain to the electron beam for injection into the CBETA loop and is operated with a low external quality factor due to high beam loading. The main linac[Eichhorn et al., 2014, 2015] on the other hand incorporates six 7-cell SRF cavities[Furuta et al., 2016] with a design energy gain of 36 MeV and will be used to execute energy recovery. Operated at $Q_L \approx 6 \times 10^7$ with solid state amplifiers, the peak detuning which can be tolerated by the main linac cavities is limited to 54 Hz with a 5 kW rf source, consequently micro-

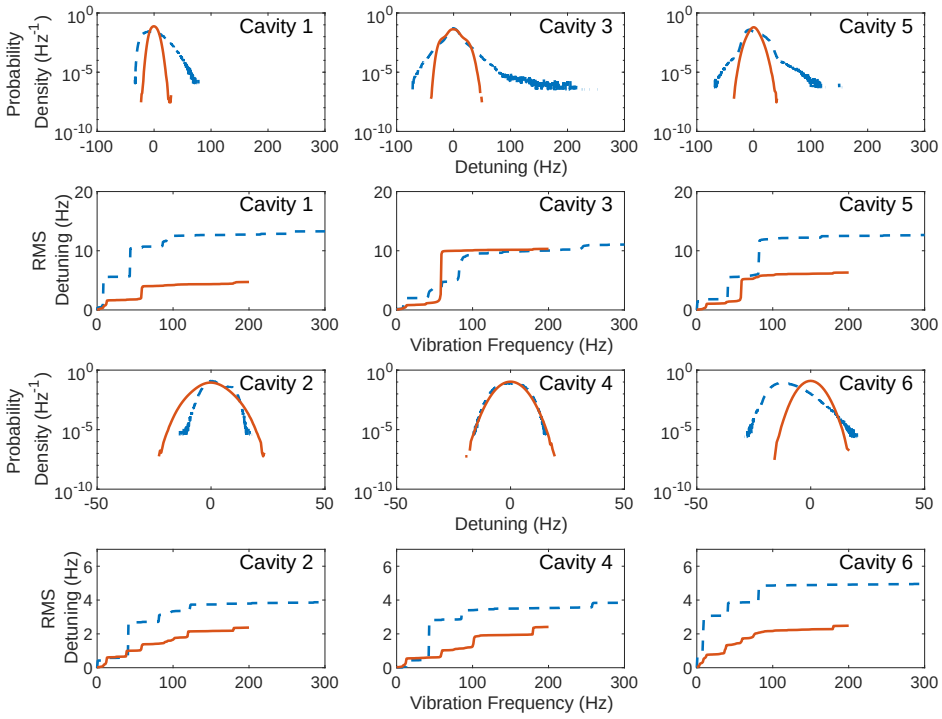

Figure 2.8: Microphonics measurements on all cavities of the main linac before (dashed blue lines) and after(solid orange) the modifications of the cryogenic system. The dashed lines represent data from the default configuration for cavities 2, 3, 5 and 6; while the data for cavities 1 and 4 were taken after making the JT and precool valves static. The solid lines indicate data after the JT and precool valves were made static and the 5 K adjust valve was fitted with sleeves.

phonics detuning presents a significant operational bottleneck and needs to be mitigated.

2.4.1 Passive Suppression

The initial microphonics measurements of the main linac cavities showed strong vibrations at frequencies 8 Hz, 41 Hz and 82 Hz as illustrated in the plots of RMS detuning in Fig. 2.8. Apart from steady vibrations at these frequencies,

sudden events resulting in large peak detuning of over 100 Hz were seen in the un-stiffened cavities 3 and 5 as evident from the histograms. Vibrations can mechanically couple into the cavities from sources both inside and outside the cryomodule. In an attempt to find them, we cross-correlated the microphonics detuning signal with vibration signatures from various machinery. We started with the rotary and turbo-molecular pumps maintaining the insulation vacuum in the cryomodule, looking at the effect of power cycling them for brief periods and eventually calculating the cross-correlation functions. Though the rotary pump didn't have any effect, the turbo-molecular pump does induce weak vibrations around 820 Hz, consistent with a rotation speed of 50000 rpm. There are large variable frequency induction motor water pumps on the experimental floor in the vicinity of the cryomodule, these were also shown to be of no effect to the microphonics detuning. Further we also measured vibrations from the large room temperature vacuum pumps controlling the vapor pressure of Helium inside the cryomodule, showing that these too don't contribute to peak detuning of the cavities directly. Besides direct mechanical coupling of vibrations through the cavity supports, pressure fluctuations in the liquid helium surrounding the cavity also give rise to microphonics detuning. Table 2.1 shows a summary of the different vibration sources and their relative contribution to the total RMS detuning in the main linac cavities. In the original configuration, the pressure variations in liquid Helium accounted for most of the microphonics in the main linac cavities.

Source	Cavity 1		Cavity 2		Cavity 3		Cavity 4		Cavity 5		Cavity 6	
	2017	2018	2017	2018	2017	2018	2017	2018	2017	2018	2017	2018
Low Frequency	0.1	0.1	1.2	0	0	0	0	0	1.3	0	2.2	0
Gas Flow 8 Hz	17	1.7	0.8	0.1	2.9	0.1	0	0.1	0.2	0.1	32.4	1.9
Valve 41 Hz	42.1	0.4	44.3	0.1	5.3	0.1	39.4	0.1	16.8	0.6	20.8	0.7
Waveguide 59 Hz	2.4	46.3	0.6	3.4	7.5	78.5	0.7	4.4	0.4	46.9	0.3	7.2
Valve 82 Hz	11.1	2.9	20	1.2	43.7	0.8	16.8	0.7	66	6.9	34.1	4.5
Miscellaneous	27.4	48.7	33.1	95	40.5	20.5	43.1	94.7	15.3	45.5	10.2	85.6

Table 2.1: Contribution from various microphonics sources, listed as percent of total mean square microphonics detuning.

The cryogenic system of the main linac cryomodule is a modified version of the TESLA design.[He et al., 2012] Separate vessels house the six cavities and are supplied with liquid Helium through chimneys by the 2K - 2 phase pipe and through the precool line connected to the bottom of the vessels. The pressure exerted by liquid Helium on the cavity walls influences the resonant frequency of the cavities and needs to be regulated. Slow trends in this pressure give rise to very low frequency microphonics detuning ($\lesssim$ 1Hz) and tight pressure regulation requires the interplay of two control mechanisms. A Joule-Thomson (JT) valve maintains the liquid level in the 2K - 2 phase pipe and an external pump maintains the vapor pressure near 12.5 Torr corresponding to 1.8 K. Two separate proportional integral feedback loops actuate the JT valve and control the pump to maintain the liquid level and vapor pressure at their set points respectively. The system also opens the precool valve when the liquid level goes below a threshold. Consequently, transients or instabilities in any of these components may give rise to vibrations in the cryomodule.

Measurements of microphonics detuning and various cryogenic control parameters showed that movement of the JT and movement of the precool valve both coincided with the large peak detuning events. The occasional actuation of the precool valve in response to the Helium liquid level going below a threshold correlated with spikes in a signal from a piezo-electric sensor. However the occurrence of peak detuning is more frequent, consequently we made both the precool and the JT valves static and the results of this test are shown in Fig. 2.9. In the default configuration, the microphonics histogram shows large peak events which are $\gtrsim$ 200Hz[2], while the peak microphonics detuning be-

[2]A slight offset in the phase calibration of the field probe signal might have led to this uncharacteristically large value of peak detuning. However all data shown in Fig. 2.9 were taken with the same calibration settings and so this is a valid verification of the valve actuation effect.

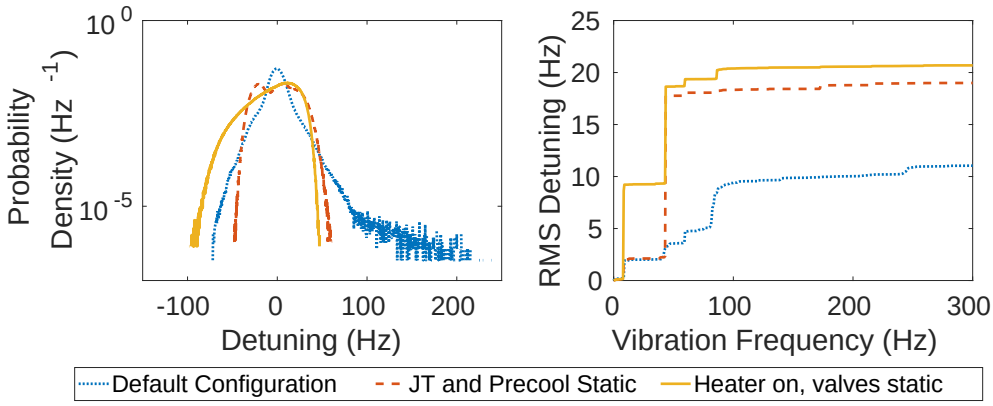

Figure 2.9: Influence of valve actuation on microphonics detuning of cavity 3 (unstiffened) showing the detuning histogram on the left panel and the RMS detuning on the right from measurements of duration 800 seconds.

comes ~ 50Hz with both valves static verifying the proposed mechanism. However, this configuration doesn't allow us to have active control on the liquid Helium level and if the boil off generated due to the thermal load from the cavities doesn't equal the rate of in-flow from the supply line, then the liquid level in the 2K - 2 phase pipe would steadily run away. To avoid this, a heater attached to the 2K - 2 phase pipe is put on a control loop to provide a minimum dynamic thermal load to substitute for when the cavities are not generating enough heat and thus boiling off suitable amounts of Helium while stabilizing the liquid level. This results in stable operation while limiting the peak detuning to ~ 100 Hz a definite improvement from the original configuration. Despite the additional detuning introduced due to the operation of the heater, this is still better than controlling the Helium level using the valves.

Peak detuning was greatly improved when the valves were made static, however we observed a strong enhancement of the steady state oscillations at 41 Hz which don't contribute much to the peak detuning but increase the RMS by a factor of 2. The liquid Helium level control using the heater enhances the

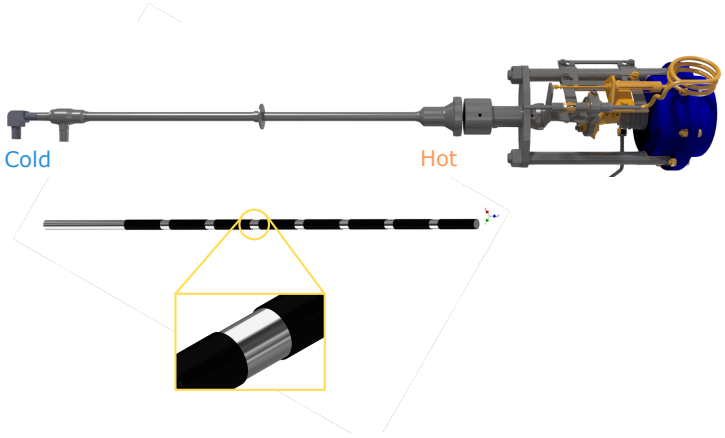

Figure 2.10: Cryogenic needle valve used to regulate Helium flow in the cryomodule and the electro-pneumatically actuated valve stem showing attached plastic sleeves filling the space between the stem and the inner surface of the stalk.

narrow band 8 Hz vibration line. This points to gas flow in the Helium Gas return Pipe (HGRP) as a possible source for the generation of the 8 Hz vibrations. Previous operations data further corroborated this fact by showing that the vibration amplitude at 8 Hz is an increasing function of the vapor flow through the Helium Gas Return Pipe possibly exciting a mechanical eigenmode of the structure. Pending further investigation into the source, the active compensation system has been successful in attenuating these vibrations.

Accelerometer measurements of vibration on the 5 K adjust cryogenic valve stalk yielded significant cross-correlation with the microphonics detuning measurement at 41 Hz and 82 Hz. Figure 2.10 is a schematic of the valve showing the cold region near the valve orifice which comes in contact with cold Helium and the warm region which extends outside the cold mass of the cryomodule and is at room temperature. Delayed heat transfer between the hot and the cold regions through convection of the Helium gas and conduction through the valve stalk leads to thermo-acoustic oscillations[Luck and Trepp, 1992] and the

resulting pressure waves resonate inside the closed space between the valve stem and the valve stalk. This mechanism of vibrations was first observed in the LCLS-II cryomodules while testing at Fermilab.[Hansen et al., 2017] Following discussions with the Fermilab team, we inserted sleeves made of a cryogenic compatible PEEK plastic material on the stem to restrict the gas flow and suppress vibrations.[Banerjee et al., 2018]

Cavity	Stiffened	df/dp	Peak Detuning (Hz)			RMS Detuning (Hz)		
		(Hz/Torr)	Original	JT and Precool Static	5 K Adjust Modified	Original	JT and Precool Static	5 K Adjust Modified
1	No	38	N/A	78	30	N/A	13.6	5.0 (4.7)
2	Yes	15	18	N/A	25	4.4	N/A	4.6 (2.4)
3	No	46	280[1]	100	50	11.2	20.8	10.7 (10.3)
4	Yes	17	N/A	17	20	N/A	4.4	3.7 (2.4)
5	No	33	163[1]	N/A	41	12.7	N/A	6.9 (6.3)
6	Yes	19	30	N/A	18	5.0	N/A	3.2 (2.5)

Table 2.2: Microphonics measurements before and after cryogenic system modifications for both stiffened and unstiffened cavities. The third column shows the pressure to detuning coefficient df/dp. RMS detuning is calculated from the detuning histograms except for the values in brackets which are obtained from the spectrum plots and are band limited to 200 Hz.

Table 2.2 shows a summary of the microphonics measurements on all cavities in different configurations of the cryogenic system. The peak detuning on all unstiffened cavities(Fig. 2.8) showed a significant reduction after the 5 K adjust valve was modified. Table 2.1 also demonstrates a significant reduction in the fractional contribution to the net mean square detuning from this instability at 41 Hz and 82 Hz. However, we measured a new vibration line at 59 Hz which wasn't seen during our previous tests. The results from cross-correlation measurements of the microphonics detuning and accelerometer signals indicate that 59 Hz vibrations from an external source are being mechanically coupled into the cryomodule through the newly installed waveguides. The new source significantly contributes to mean square detuning on all the unstiffened cavities as shown in Tab. 2.1. Cavity 3 is affected the most with the highest peak detuning ($\sim$ 50 Hz) among all others and this was an excellent candidate for testing the active compensation system. Nevertheless, these 59 Hz vibrations were eventually decoupled from the cryomodule as explained in Chap. 3.

Stiffened cavities did not show a significant reduction in peak microphonics detuning after the change in the cryogenic system, with an increase being shown by cavities 2 and 4 even when the RMS diminished for cavity 4. Figure 2.8 shows results from microphonics measurements on these cavities. The histogram of detuning for cavity 2 and cavity 4 shows a flat top, indicating deviations from Gaussian white noise. The spectrum plot shows substantial vibration energy localized around 41 Hz and the 82 Hz corroborating this observation and the thermo-acoustic oscillations are indeed the reason as discussed earlier. The spectrum plots further indicate a reduction of the energy after valve modification in the same frequency bands, along with a net decrease in RMS detuning up to a vibration frequency of 200 Hz which is the limit of the data set. How-

ever, the width of the histograms also related to the RMS seems unchanged for cavity 4 and shows an increase in cavity 2 after valve modification seemingly contradicting the frequency domain observations. This apparent disagreement of the RMS detuning obtained from the histogram and the spectrum plots are listed in Tab. 2.2. While the estimates agree for un-stiffened cavities, there is a significant difference for the stiffened cavities. The missing vibration energy could be accounted for by the excitation of high frequencies ($\gtrsim 200\,\mathrm{Hz}$), possibly the mechanical eigenmodes of the cavity along with measurement noise. Unfortunately the raw signals were not recorded during this experiment rendering us unable to analyze this in more detail.

2.4.2 Active Compensation

Passive measures of mitigating the vibration sources is the preferred method of reducing microphonics detuning. However active control is also necessary to temporarily restore operating gradient until the source is mitigated and to improve the margin of rf power consumption in the presence of existing microphonics detuning. We implemented the narrow band ANC algorithm in the Cornell Digital Low Level rf control system [Neumann et al., 2011, Liepe et al., 2005] for this purpose. Figure 2.11 presents a simplified diagram of the rf system showing the relevant signal paths. We mix the rf signals from the cavity with an internal frequency reference to generate a baseband signal at 12.5 MHz. The field control loop runs at this frequency in a Field Programmable Gate Array (FPGA) which measures the amplitudes and phases of the field and the forward power, while the difference of the phases is used to determine the net microphonics detuning δf_{comp}. The processed detuning and field data are then

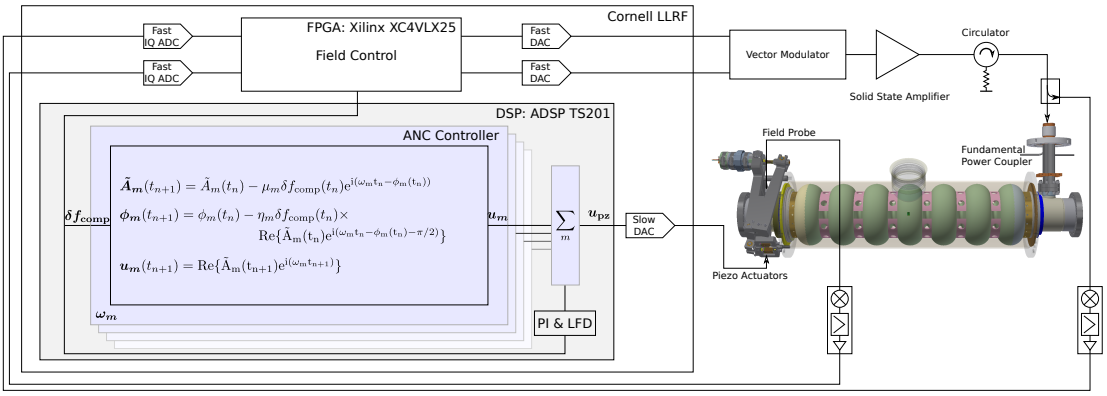

Figure 2.11: Simplified diagram of the setup used during routine Linac operations for CBETA showing the Cornell Low Level Radio Frequency control system and associated rf equipment.

transferred to a Digital Signal Processor (DSP) (ADSP TS201) which we use to execute resonance control. The modified ANC algorithm [Eq. (2.13), (2.28) and (2.5)] is executed inside the DSP for each microphonic spectral line at ω_m. The output of all the individual controllers u_m are summed and sent to the piezoelectric actuator. Besides the modified ANC algorithm proposed in this chapter, the DSP also incorporates LFD compensation and Proportional Integral control on low frequency microphonics.

The implemented ANC algorithm requires prior knowledge of the frequency content of external vibrations but does not require any measurement of the tuner transfer function at the frequencies of interest. We first measure the spectrum of microphonics detuning and determine which frequencies we want to compensate. The algorithm is then applied separately on each of these known excitations at ω_m. It requires two additional parameters, the gain μ_m and phase adaptation rate η_m as described in Eq. (2.13) and Eq. (2.28) respectively for each of these excitations. To determine an optimum setting, we start with small numbers for μ_m and η_m until we start observing some effects on the net microphonics detuning, increasing μ_m until the feedback loop becomes unstable. At the

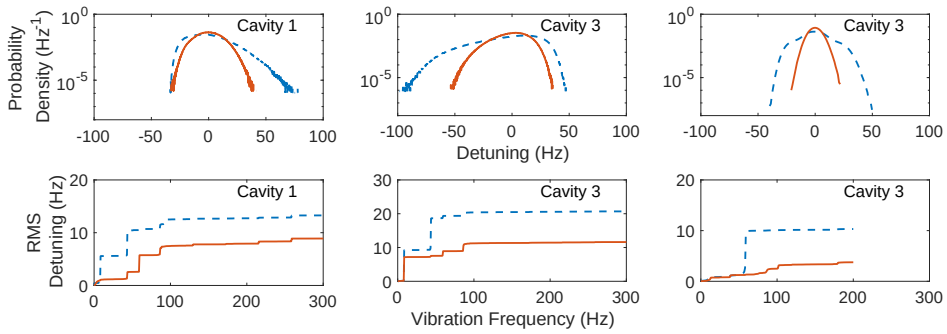

Figure 2.12: Effect of active microphonics compensation on two un-stiffened cavities of the main linac. The dashed lines represent data without active suppression while the bold lines show the performance with ANC turned on. The first two sets of data were taken before valve modification while the last data set was taken after.

same time, we minimize the peak detuning by optimizing the value of ω_m which strongly determines the performance. We set μ_m to half of the maximum stable value to give us a suitable gain margin, and observe the controller phase ϕ_m as a function of time. We set η_m so that the phase settles to the optimum value on average within a few minutes at the same time showing a noise level within $\pm 10^\circ$. This process is repeated for each frequency we want to compensate, while the overall performance of resonance control depends on the quality factors of vibrations as illustrated in Fig. 2.7.

We have used the ANC algorithm during various stages of rf commissioning to attenuate microphonics and the results from un-stiffened cavities of the main linac are shown in Fig. 2.12. Before we modified the 5 K adjust valve, compensation was applied to 41 Hz and 8 Hz on un-stiffened cavities 1 and 3. The algorithm was successful in attenuating 41 Hz in both cavities 1 and 3 but was not effective on 8 Hz vibrations in cavity 3 as illustrated by the spectrum plots probably because the compensation frequency was not set precisely. These narrow band vibrations were a major contribution to microphonics detuning and

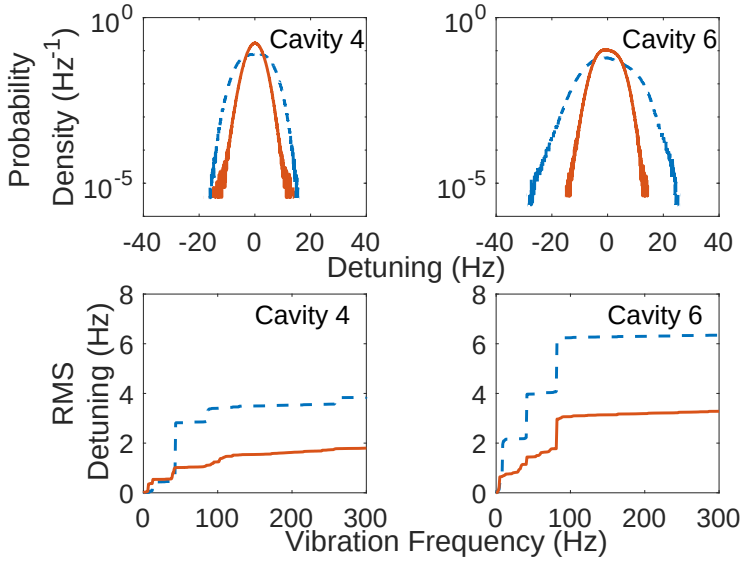

Figure 2.13: Effect of active microphonics compensation on two stiffened cavities of the main linac. The dashed lines represent data without active suppression while the bold lines show the performance with ANC turned on.

their decrease also reduced the peak detuning. After we modified the 5 K adjust valve, we found the major source of microphonics detuning to be at 59 Hz. The ANC algorithm was successful in suppressing these vibrations in cavity 3. The attenuation of spectral lines are further validated by the RMS detuning as listed in Tab. 2.3. The success of the algorithm indicates that those vibration lines were not in the vicinity of mechanical eigenmodes of the tuner-cavity system which would have limited the effectiveness of the system as explained in Sec. 2.3.

The results of using the system on stiffened cavities is shown in Fig. 2.13. The algorithm was applied to cavities 4 and 6 for the frequencies 8 Hz and 41 Hz with additional attenuation of 82 Hz on cavity 6. While the ANC successfully reduced peak detuning from 30 Hz to 15 Hz in cavity 6, the measurements on cavity 4 indicate no reduction of peak detuning even though the RMS detun-

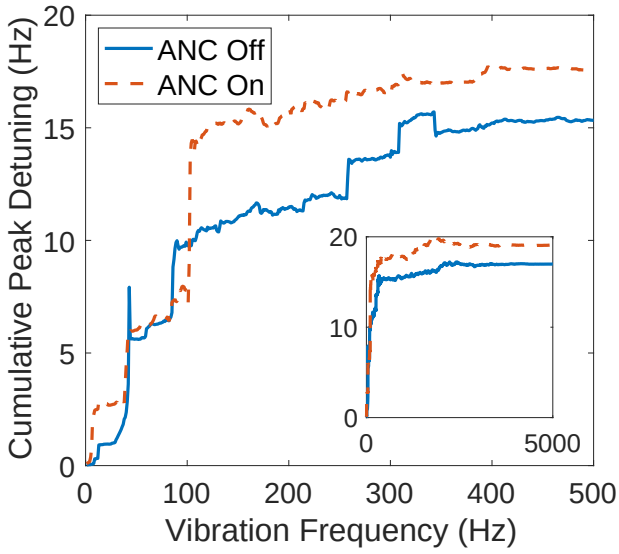

Figure 2.14: Cumulative peak detuning as a function of frequency for cavity 4 before valve modification showing the effect of active noise control system.

ing is attenuated as seen from both the histogram and the spectrum plot. To understand which frequencies actually contribute to peak detuning, we Fourier transform the raw signal and zero all components beyond a certain vibration frequency and then find the peak detuning of the inverse transformed signal. Figure 2.14 shows the cumulative peak detuning as a function of the vibration frequency threshold. When the ANC is off, 41 Hz and 82 Hz contribute most to the peak detuning as indicated by the large steps when we include these frequencies in the peak calculation. When we turn on compensation, the contribution from both these frequencies are reduced but a new mode at 102 Hz appears which accounts for almost half of the peak detuning but appears as a shallow step in the spectrum plot, illustrating it's transient nature. These additional spectral lines generated by the ANC controller point to transients possibly generated by the non-linear phase adaptation process. Nevertheless, the

Run Description	Peak Detuning (Hz)		RMS Detuning (Hz)	
	ANC Off	ANC On	ANC Off	ANC On
Cavity 1 with JT and precool static	78	45	13.6	9.1
Cavity 3 with JT and precool static	100	57	20.8	11.7
Cavity 3 with JT and precool static and 5 K adjust valve modified	50	22	10.7	4.6
Cavity 4 with JT and precool static	17	19	4.4	2.4
Cavity 6 in original configuration	30	15	6.4	3.4

Table 2.3: Results of using the Active Noise Control system on various cavities during different stages of commissioning.

ANC algorithm is well suited for compensating narrow band vibrations in both stiffened and un-stiffened cavities as evidenced from the performance listed in Tab. 2.3.

The stability and robustness of the algorithm is demonstrated by comparatively long periods of stable operation with the same settings on different days. The observations shown in Tab. 2.3 are taken from data sets of at least 800 seconds measured for cavities inside a cryomodule connected to a production level cryogenic system unlike previous work primarily focused on test facilities. We achieved stable operations of over a few hours without spontaneous trips on all cavities with the ANC system active. We also successfully used it on cavity 3 during beam operations for the CBETA Fractional Arc Test which helped us achieve an energy gain of 8 MeV using a forward power below 5 kW which would not be possible without it. Once the settings were determined using the procedure explained earlier, resonance control was turn key with no tweaking required on subsequent days of operation which highlights the robustness of

the system.

Lorentz Force Detuning (LFD) and mechanical coupling between different cavities in the cryomodule can be further sources of detuning which affect the operation of a resonance control system. The field dependence of LFD leads to decrease in the resonant frequency when the cavity field is ramped up. Large microphonics events generating a sudden increase in the resonance frequency of the cavity can lead to reduction in fields, LFD can in turn detune the cavity further in the positive direction amplifying the effect of the microphonics. Such an instability will lead to a catastrophic fall in cavity field and subsequent beam loss in an accelerator. However, in high Q machines the filling time of narrow bandwidth cavities can be sufficiently large, of the order of tens of milliseconds, slowing down the field decrease. This along with the presence of a high gain feedback loop on the field can be enough to avoid such an instability from developing. In all our operations till now, we have not used any feed-forward control of detuning and simple integral control of detuning has been enough to compensate for LFD when the field is ramped slowly. Further, the resonance control system of neighboring cavities did not interact with each other during the course of normal operation since we have bellows mechanically isolating the cavities. This eliminates the need to account for such effects. The resonance control system described in this chapter is thus a stable way of reducing peak detuning when mitigation of vibration sources is not an option and has been used in various stages of rf commissioning which is the subject of the next chapter.

CHAPTER 3

RF COMMISSIONING

The Main Linac Cryomodule (MLC) is responsible for accelerating the injected beam in CBETA and recovering the energy of the used beam. This chapter details the commissioning process of the first narrow bandwidth ($Q_L \gtrsim 10^7$) SRF linac ever operated with beam. While the previous chapter focused on the crucial aspect of active suppression of microphonics detuning, in this chapter we outline the major steps for commissioning this SRF linac including set up and operation of the high power rf system, the cryogenic system and finally the control system which regulates the accelerating fields in the cavities. The experimental measurement of the energy recovery process in the main linac is also presented which we use to calculate the power balance efficiency achieved in the current commissioning stage of CBETA.

3.1 Introduction

CBETA incorporates two SRF linacs operating in cw, one for the injection system and the other used for energy recovery. The injector cryomodule[Liepe et al., 2011, 2012] consists of five 2-cell SRF cavities[Liepe et al., 2010] and is configured to provide a 6 MeV electron beam for injection into the CBETA re-circulation loop. The injector cryomodule has been commissioned in multiple stages, finally reaching a peak operating current of 70 mA in 2013[Dunham et al., 2013]. The main linac[Eichhorn et al., 2014, 2015] on the other hand incorporates six 7-cell SRF cavities[Furuta et al., 2016] with a design energy gain of 36 MeV. Initial commissioning of the cryomodule included the first cool-down[Eichhorn et al.,

2016] during which various thermo-mechanical properties of the cryomodule were measured including precision alignment of the beam-line and the results were compared with model specifications. This was followed by initial cavity testing at the operating temperature of 1.8 K to determine Q_L and Q_0 v/s E[Furuta et al., 2017] followed by the first microphonics measurements[Ge et al., 2017]. These tests were followed by a warm-up for re-location of the cryomodule to it's final position for CBETA and a subsequent cool-down at the new position in preparation for beam operation.

The commissioning process started with testing the various linac subsystems involved in beam operations. The second section describes the evaluation of high level rf components used to provide rf energy to the cavities, the commissioning of the Low Level RF (LLRF) system and the cryogenic system. The next section details the process of rf commissioning, including cavity tuning, control system configuration and performance measurement of the main linac. The last section describes measurements of beam loading and energy recovery during 1-turn high-current operations of CBETA.

3.2 Linac Subsystems

The main linac cryomodule is based on the TESLA design but is optimized for cw energy recovery operation. The cryomodule incorporates six 7-cell SRF cavities operating in a Helium bath maintained at 1.8 K, each attached to a fundamental input coupler capable of providing cw 10 kW at 1.3 GHz. The beamline includes 7 dielectric absorbers to dissipate away the substantial Higher Order Mode (HOM) powers expected to be generated during operation at 320 mA of

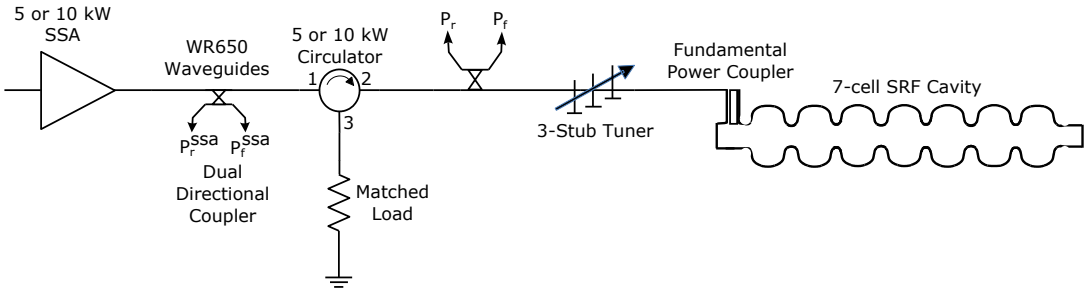

Figure 3.1: Typical rf power arrangement for one MLC cavity.

total re-circulating beam current through the cryomodule. For this initial phase of commissioning limited to tens of micro-amps, the critical milestones were the operation of the rf sources and the associated equipment, cavity resonance stabilization and the demonstration of the cryogenic system being able to handle the generated heat load from the fundamental mode.

3.2.1 High Level RF

All six cavities of the MLC are powered by individual Solid State Amplifiers (SSA) connected to the cavity through a directional coupler, circulator and a 3-stub waveguide tuner as shown in Fig. 3.1. There are two sets of high power rf components capable of 5 kW and 10 kW for stiffened and un-stiffened cavities (Fig. 3.10) respectively. All these components were tested to full power in order to understand their characteristics and verify operational readiness.

The solid state amplifiers manufactured by SigmaPhi Electronics are built using a modular approach as shown in Fig. 3.2. In each of the six amplifiers, the input signal is first amplified using a rf pre-amplifier module, the output is then split and sent to individual amplifier *modules* each capable of generating ≈ 2 kW.

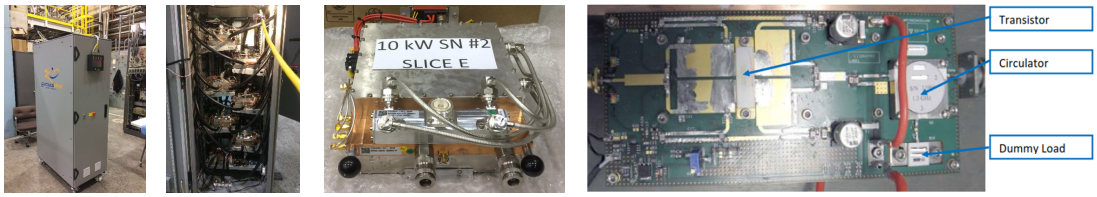

Figure 3.2: Individual components of the solid state amplifiers. From left to right: SSA cabinet, the placement of the power modules, a single water-cooled module and an internal pallet respectively.

The 10 kW SSA has six modules while the 5 kW unit has three. Each of the water-cooled 2 kW modules is comprised of four rf pallets, which are individual electronic boards with a single 500 W 1300 MHz power transistor, a circulator and matched load. The modular design of the SSA improves the reliability of the system since it can continue to operate with multiple failed rf power transistors. The power generated, P_o in the presence of multiple transistor failures is given by,

$$P_o = P_t\left(\frac{N - N_f}{N}\right)^2, \tag{3.1}$$

where P_t is total power without transistor failures, N and N_f are the total number and the number of failed transistors respectively. The power output from these modules are combined and routed through a waveguide directional coupler which is used by the SSA for internal monitoring and is also available to the cavity control system for measurement and control purposes.

In the presence of low beam loading, the fundamental input couplers reflect almost all the forward power sent into them which can be seen by plugging in $I_b = 0$ in Eq. (1.34) As a result, rf circulators are used with each SSA in order to protect them from a full power reflection and their arrangement is shown in Fig. 3.1. Typical rf power circulators are three port devices. Power goes into port 1 and out of port 2 while the reflected power comes back to port 2 and

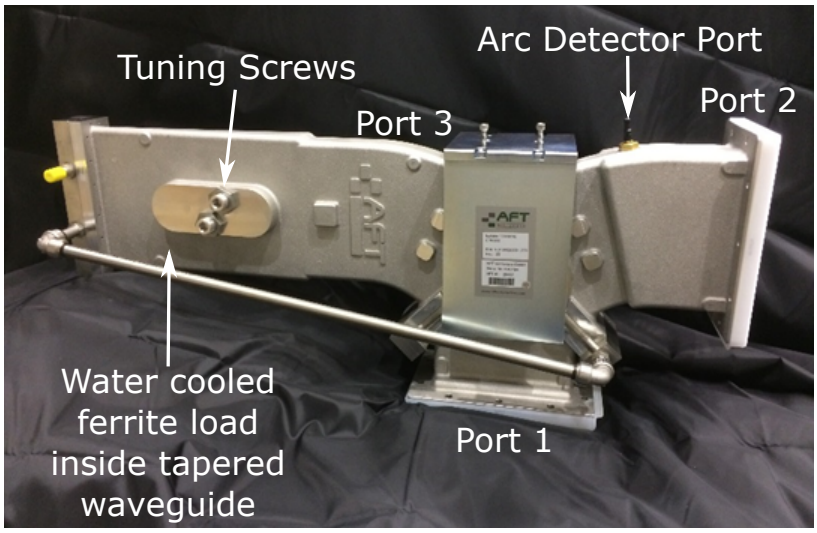

Figure 3.3: Rf circulator used for the MLC RF system.

gets directed to port 3 which is connected to an external matched load. The circulators used for the MLC shown in Fig. 3.3 use an integrated water-cooled ferrite load which forms an inner conductor installed in the tapered waveguide shown to the left of the image. It is fitted with two 1 inch aluminum screws for isolation tuning. The screws have a plastic piece on the internal end that prevent electrical shorting between the tapered waveguide and the ferrite load.

The high level rf system for each cavity were evaluated individually by injecting a cw drive signal from a standalone rf generator into the SSAs. In the test setup, the waveguide feeding the input coupler of the cavity was shorted to achieve full reflection back into the circulator. The forward and reflected powers were measured in 1 kW increments using the internal SSA directional coupler connected to external power meters. Several failures happened in the first stage of testing. A damaged internal RF cable (Fig. 3.4) led to the failure of a single rf power module on a 5 kW SSA. The initial power tests also exposed problems with the circulators

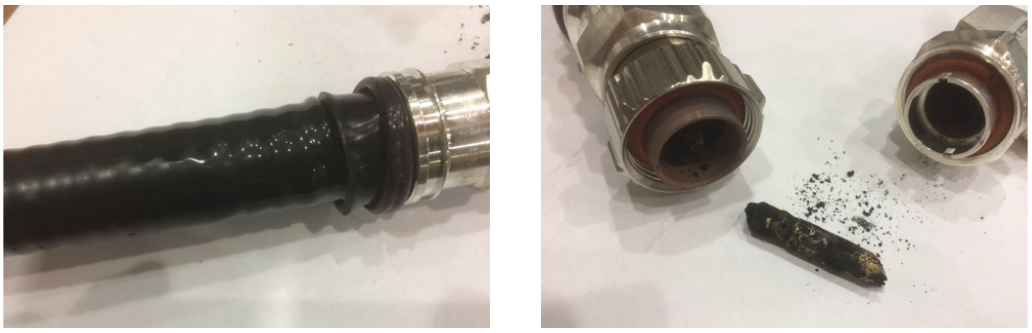

Figure 3.4: Damage to an internal cable connecting a single module to the power combiner in a 5 kW SSA which led to the failure of the associated power module.

As the power was increased during initial tests, we observed spikes in the temperature of the load tuning screws on all the circulators of as much as 90° C. This was accompanied by an increase in power routed back into the SSAs, shown as P_r^{ssa} in Fig. 3.1. A visual inspection of the internal surfaces of the circulator after the test showed severe disintegration of the plastic on the screws. In several circulators, the plastic was completely vaporized and condensed on the circulator ferrites as pictured in the first panel of Fig. 3.5. In addition, the ferrite loads were also damaged with the appearance of broken ferrite tiles (second panel) and in some cases severe pitting of the ferrite load substrate (third panel) caused by arcing triggered by the presence of the dielectric residue. The cause was eventually traced to a manufacturing error, where a dielectric with high loss tangent was used instead of the design material. Even though this damage severely limited the rf power which could be used for operations, we successfully completed the initial commissioning stage of CBETA with mitigation measures put in place.[Gulliford et al., 2019]

After the repair of the circulators and the damaged power amplifier, the high level rf system was successfully tested to full power. Figure 3.6 shows the final measurements. While odd numbered SSAs capable of 10 kW, power unstiffened

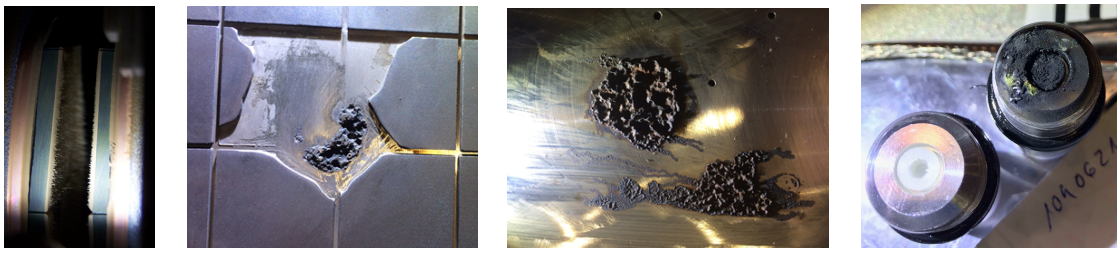

Figure 3.5: Images from damaged circulators. From the left, the panels show ferrites on a 5 kW circulator contaminated with plastic insulator material, damage to the load plates on a 10 kW and a 5 kW circulator respectively. The rightmost panel shows a damaged screw and its replacement.

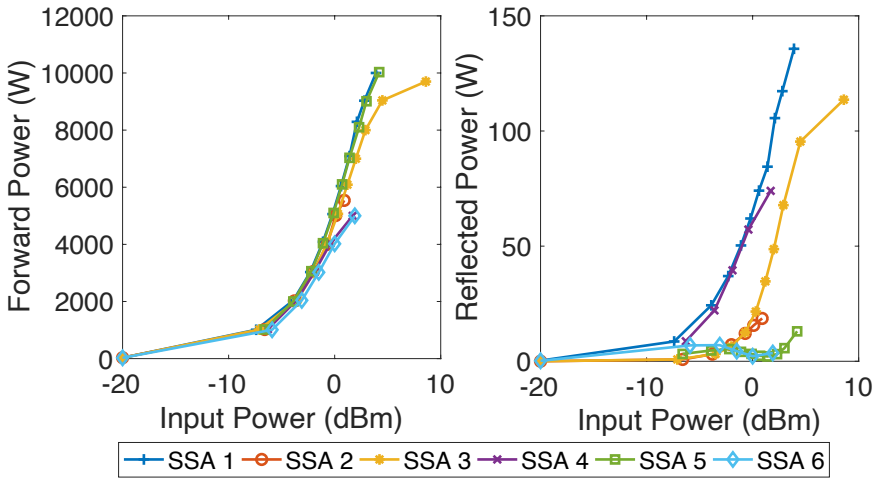

Figure 3.6: Transfer function measurement of the individual SSAs used for powering six 7-cell cavities after all components were repaired. The left and right panels show P_f^{ssa} and P_r^{ssa} as a function of input power respectively.

cavities, the even numbered ones capable of 5 kW power the stiffened cavities. The maximum power output of the SSAs in the left panel are consistent with the desired values, while the power reflected back into them is less than 150 W which is well within the capability of the circulators and the matched loads internal to the SSAs themselves. These measurements indicate satisfactory performance of all components of the high level rf system used to power individual cavities of the MLC.

3.2.2 Low Level RF

Figure 3.7 presents a simplified schematic of the MLC rf system, showing the Low Level Radio Frequency system, high power rf components and clock distribution with the important signal paths. The LLRF system is responsible for maintaining stable accelerating fields in each cavity with a constant amplitude close to a desired set-point and a constant phase with respect to the timing of the beam. This control is achieved using a Proportional Integral (PI) control loop implemented in the Cornell Digital LLRF system[Liepe et al., 2005, Neumann et al., 2011]. Until quite recently, directly digitizing and controlling a 1.3 GHz rf signal has not been possible. Hence, the LLRF works at an intermediate frequency (IF) of 12.5 MHz which is phase-locked to a 1.3 GHz master oscillator which also times the bunches generated by the photo-injector . All rf signals are mixed down to the IF and converted to phasors for processing in the system. The mixer responsible for the field signal is represented as the solid blue circle with a $\times$ symbol in Fig. 3.7. The PI control loop then uses the measured field phasor and outputs a drive phasor to restore the field to the set-point. The output phasor is then fed into a vector modulator which converts the phasor a back to 1.3 GHz which is sent to the amplifier.

The LLRF system uses the measured value of the field phasor $\tilde{V}_c$, the forward $\tilde{I}_+$ and reflected $\tilde{I}_-$ wave phasors which were discussed in Sec. 1.3. However, the actual measurements are in the form of integers corresponding to the digitized level of the input signal. Hence, a calibration process is required to determine the scale factors for the signals measured. In addition, the different cable lengths, mixers, circulators and other rf components introduce unknown phase shifts into the measurement which need to be accounted for to establish

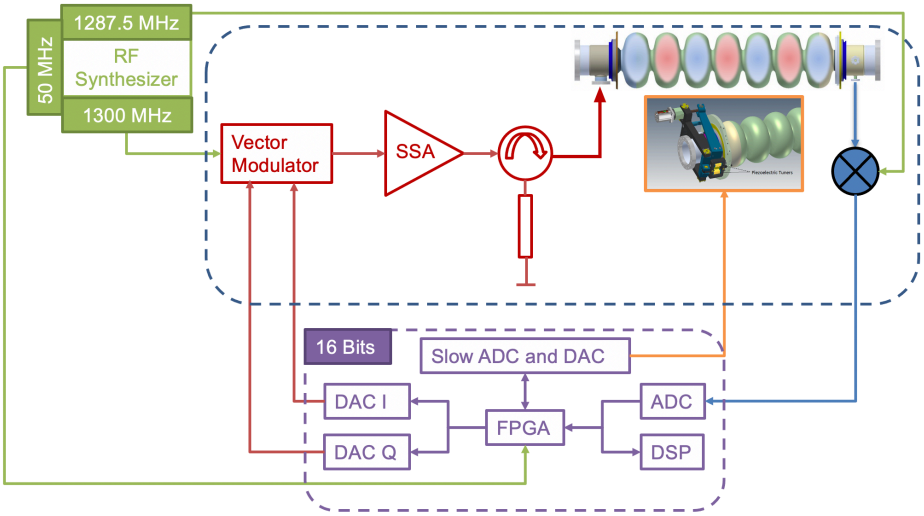

Figure 3.7: Simplified diagram of the MLC RF control system showing the various components of the LLRF system (purple dashed rectangle), the high power rf components (blue dashed rectangle) and the clock distribution system.(green)

control stability. Hence, the LLRF also incorporates adjustable rotation matrices which can be used to rotate the measured phasors before being used by the control loop. Control system commissioning includes setting all the the control parameters for optimum operation including rotations and feedback gains along with calibration of the various signal paths in the system.

The calibration of various signals used by the LLRF system involves finding the scale factors which are used to convert the raw Analog to Digital Converter (ADC) readings into physical units including various powers in kW and the cavity voltage in kV. We first calibrate the forward and reflected powers by using the same setup used to test the high power rf components, i.e leave the waveguide shorted so that power does not enter the cavity. To calibrate the forward power channel, we first measure the total attenuation of the signal path from the directional coupler into the mixer using a network analyzer. By applying a known excitation to the SSA, we then read the phasor measured by the LLRF

system in terms of ADC counts. Using these measurements we can evaluate the scale parameter K (in kW/count^2) as $K = P/A^2$, where P is the measurement from a calibrated power meter in kW and A is the time averaged un-scaled amplitude measured by an ADC channel in the LLRF system. We follow the same procedure for P_f, P_r and P_r^{ssa}. The field phasor on the other hand is calibrated later in the commissioning process using the beam.

3.2.3 Cryogenic System

The cryogenic system of the main linac cryomodule is shown in Fig. 3.8.[He et al., 2012] An external Heat Exchanger (HEx) and cryogenic distribution system supplies liquid Helium to the cryomodule through the *2K Supply (or precool)* line shown to the left of the schematic. Separate vessels house the six SRF cavities which are supplied liquid Helium (dark pink in schematic) on the top through chimneys by the 2 K - 2 phase pipe. The precool line at the bottom of the Helium vessels can also supply or vent Helium during warm-up and cool-down. The pressure exerted by liquid Helium on the cavity walls influences the resonant frequency of the cavities and needs to be regulated. Slow trends in this pressure give rise to very low frequency microphonics detuning ($\lesssim$ 1 Hz) and tight pressure regulation requires the interplay of two control mechanisms. The Joule-Thomson (JT) valve allows the flow of liquid into the 2 K - 2 phase pipe thereby controlling the liquid level in the Helium vessels, while the vapor rises through the chimney into the Helium Gas Return Pipe (HGRP). The vapor exits through the *1.8 K return* line into four warm compressors which maintain the vapor pressure (and temperature of the cavities) by pumping away the vapor created by the dissipated heat from the cavities. Two separate PI control loops

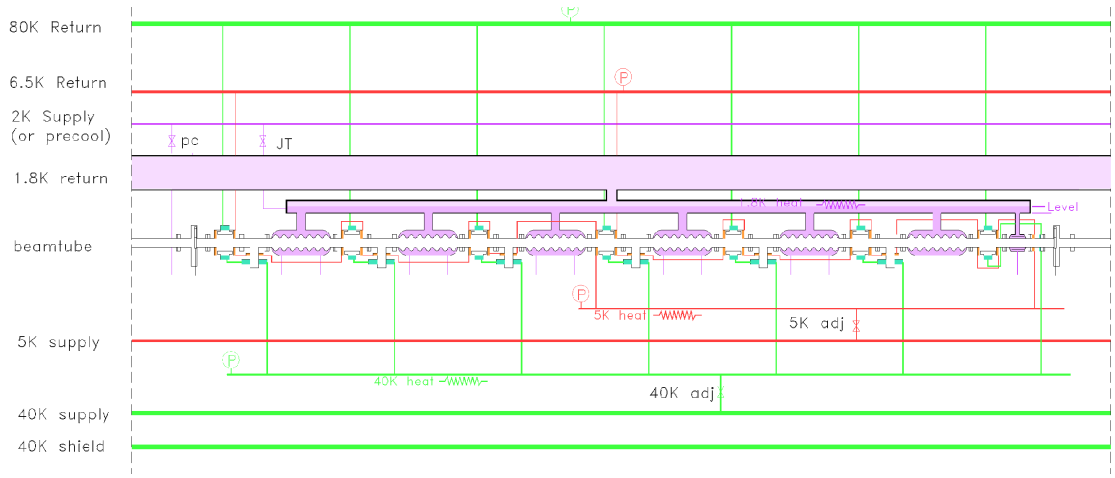

Figure 3.8: Schematic of the cryogenic system inside the MLC. Light and dark pink represent areas of gaseous and liquid Helium respectively which directly cools the cavity, while the lines colored green cool other parts of the cryomodule.

actuate the JT valve and controls the speed of the warm compressor to maintain the liquid level and vapor pressure in the 2 K - 2 phase pipe at their set points respectively. During operations these also induce mechanical vibrations.

The optimization of the cryogenic system aims to reduce microphonics detuning while maintaining a stable operating temperature and pressure for the cavities in the presence of variable heat loads. The modification of the cryogenic needle valves (JT, precool and 5 K adjust) to reduce thermo-acoustic oscillations have already been discussed in the previous chapter. In this section, we describe two separate procedures which are used to operate the cryomodule under the nominal heat load with minimum induced vibrations during operations and during idle times. While idling, the aim of the optimization is to maintain a fixed bath pressure of 12.5 Torr in order to maintain the resonance frequency of the cavity while using minimum effort from the refrigeration system. To this effect, the JT valve is kept open at a low setting to account for the static heat load and only one warm compressor is operated at its minimum speed setting

to pump the heat away. A bypass valve is used to optimize the flow of Helium gas and hence maintain the required pressure. During the start of CBETA operations, more warm compressors are turned on depending on the expected heat load and the JT valve is opened to a larger setting to allow more liquid into the Helium vessels. Initially, a heater is used to balance the total heat load while the cavities are ramped to their nominal fields. As the cavities reach their peak heat loads, this heater is turned off and a controller automatically adjusts the speed of the compressors in order to maintain the required operating pressure of 12.5 Torr. This arrangement minimizes microphonics detuning of the narrow bandwidth SRF cavities, which greatly improves stability of the accelerating field.

The ability of the cryogenic system in sustaining a heat load is indicated by the speed with which the warm compressors have to operate in order to sustain the fixed vapor pressure of 12.5 Torr. While there are four compressors available to handle the heat load, only two are used during routine operations. The performance of the cryogenic system during normal CBETA operations as illustrated in Fig. 3.9, show that both compressors never exceed 50 % of their maximum speed.

3.3 RF Commissioning

Once the operation of all the linac subsystems were validated, then each individual SRF cavity was commissioned to achieve the nominal accelerating gradient.

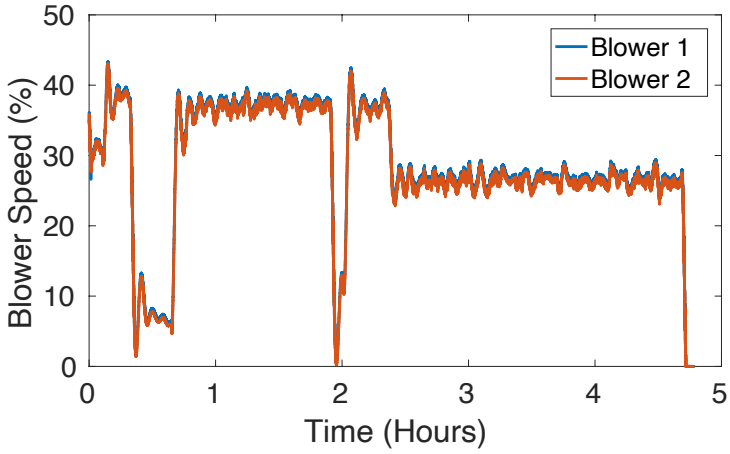

Figure 3.9: Warm compressor(blower) speeds (percentage of maximum) as functions of time during typical operations of the MLC at 36 MeV energy gain.

3.3.1 Cavity Tuning

The CBETA rf system and the photo-injector are synchronized to a master oscillator with a design frequency of 1.3 GHz and all SRF cavities need to be in resonance at this frequency. The tuning angle ϕ_t which is the phase difference between the field phasor $\tilde{V}_c$ and the forward power phasor $\tilde{I}_+$ is used to measure the detuning δf of the cavities. Using Eq. (**??**) and (1.31) from Chap. 1 we get,

$$\phi_t \equiv \arg \frac{\tilde{V}_c}{\tilde{I}_+} = \tan^{-1}\left\{Q_L\Big(\frac{\omega}{\omega_0} - \frac{\omega_0}{\omega}\Big)\right\}, \tag{3.2}$$

where ω and ω_0 are the master oscillator frequency and the resonance frequency of the fundamental mode respectively. In the regime of detuning $\delta\omega \equiv \omega - \omega_0$ much smaller than the resonant frequency of the fundamental mode,

$$\delta f = \frac{f}{2Q_L} \tan\phi_t\,, \tag{3.3}$$

where f is the clock frequency of the rf system. The cavities are adjusted using a tuner system which mechanically deforms them into resonance i.e. $\delta f = 0$. The tuning range of each cavity is different due to variability in fabrication and

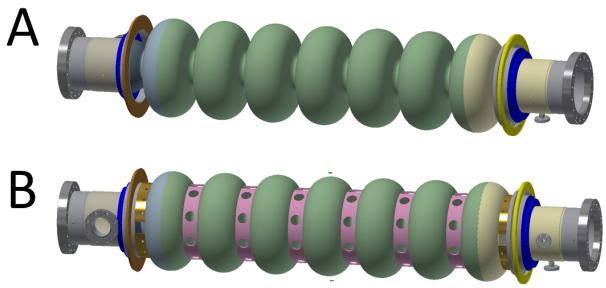

Figure 3.10: Main linac cavities used in the CBETA project. A is an unstiffened cavity, while B has stiffening rings welded on to it.

need to be measured. In the MLC, three out of the six cavities are mechanically stiffened by welding metal rings (Fig. 3.10) on to them which makes them less susceptible to pressure changes in the Helium bath.[Posen and Liepe, 2012b] However at the same time, the extra stiffness leads to a reduced tuning range and in MLC cavity 6, we couldn't tune it to above 1.3 GHz - 80 kHz. Except for one cavity in the SRF injector which we detuned far from resonance, we tuned all others to the new master oscillator frequency of 1.2999 GHz and re-optimized the beam optics for operation although with some minimal penalty on the emittance of the injected beam.

Apart from the mean resonance frequency, transient deformations can also detune the cavities. One source of time dependent forces is the interaction of the cavity magnetic field with the currents induced in the walls. This leads to Lorentz Force Detuning δf_{LFD} which is a function of accelerating gradient E_{acc} given by,

$$\delta f_{\mathrm{LFD}} = -K_{\mathrm{LFD}} E_{acc}^2 \tag{3.4}$$

where the minus sign indicates that the resonance frequency decreases with increase in field and K_{LFD} is a constant with a typical value of $1\,\mathrm{Hz/(MV/m)^2}$. Ramping up the accelerating field to the nominal value thus detunes the cav-

ity by $\approx$ 55 Hz which is more than twice the loaded cavity bandwidth. We use a piezo-electric actuator driven fast tuner to compensate for such transient changes.[Posen and Liepe, 2012a]

Vibration driven microphonics detuning is the most important transient perturbation in the rf system which leads to fluctuations primarily in the phase of the electric field. The maximum forward power P_+ required to sustain an accelerating voltage V_c under a detuning δf (revisited from Chap. 2) is given by,

$$P_+ = \frac{V_c^2}{8\frac{R}{Q}Q_L}\left\{1 + \left(\frac{2Q_L\delta f}{f}\right)^2\right\}. \tag{3.5}$$

Using the parameters for the MLC cavities ($Q_L \sim 6 \times 10^7$ and $R/Q \sim 387\,\Omega$), we can estimate that the peak microphonics detuning must be kept below 54 Hz in order to sustain a cavity voltage of 6 MV per cavity using a 5 kW power source. Chapter 2 details the microphonics suppression of the MLC cavities including the use of an active control system to compensate for narrow bandwidth vibrations.

One major source of microphonics detuning during the final stages of commissioning was mechanical coupling of external vibrations into the cryomodule through the waveguides. This source affected cavity 3 the most, generating the highest peak detuning ($\sim$ 50 Hz) among all others. While initially the resonance control system was used to actively compensate for the 59 Hz vibrations, we eventually reinforced the waveguide structure to reduce the vibration coupling. Damping material was also introduced in between the waveguide and its support to absorb the vibration energy. The reinforcements and the waveguide arrangement is shown in Fig. 3.11. Similar mitigation strategies were also applied to cryogenic pipelines and other structures in order to lower the peak microphonics detuning to 23 Hz among all cavities.

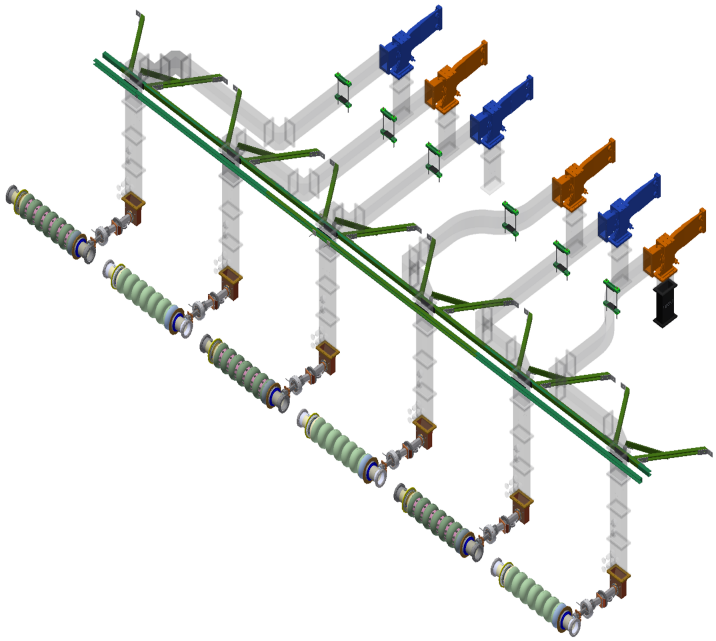

Figure 3.11: Arrangement of waveguides(gray) and reinforcements(green).

3.3.2 Control System Configuration

The initial commissioning of the MLC after setting up the high level RF and cryogenic systems involved calibrations of various signal paths, configuring the LLRF system with default parameters and then tuning the cavities to resonance from their warm-up positions. While this process needs to be done only once, we still need a daily start-up procedure to account for various drifts in the machine. This subsection documents the approach we follow to prepare the MLC for beam operations. While the initial commissioning was completed manually, most of these steps are automatically executed for routine operations using a dedicated sequencer capable of rudimentary error handling. Such automation has also been used elsewhere[Geng, 2017]. Repeating these procedures everyday ensures stable operations.

Step 1: Cavity tuning is initially achieved with the stepper motor based slow

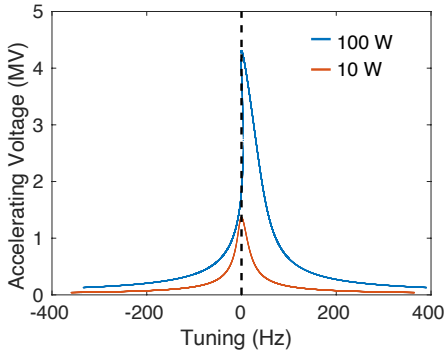

Figure 3.12: Theoretical calculation of accelerating voltage as a function of tuner position showing the effect of Lorentz Force Detuning (LFD) on the resonance curve.

tuner in order to obtain resonance at the clock frequency of 1299.9 MHz. We first used a network analyzer to tune the cavity within 10 kHz of the clock frequency at low field while we use the LLRF system in constant power mode to fine tune the cavity to within a few Hz of resonance on average. The aim of the tuning process is to maximize the field signal which gives us the resonance position. To highlight the effect of using different power settings, the resonance curve as influenced by LFD is illustrated in Fig. 3.12. At 100 W, a non-linear behavior is noted, where LFD self-consistently affects the resonance frequency of the cavity and the hence the field itself. With a forward power of 10 W, the effects of LFD are negligible, and the field at resonance is $\sim$ 1.3 MV making this the standard tuning procedure. An automatic tuning algorithm based on a decision tree approach was developed which is capable of handling the hysteresis of the tuner movement and includes safety features not to overdrive the tuner. Fig. 3.13 shows the performance of this algorithm on four cavities illustrating how the algorithm can recover even after going through the resonance peak. This step is a prerequisite for subsequent procedures which requires a well tuned cavity.

Step 2: The Digital to Analog Converter (DAC) output used in the LLRF sys-

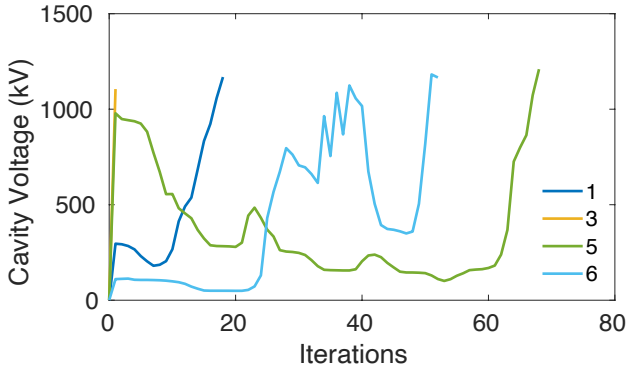

Figure 3.13: Performance of the automatic coarse tuning algorithm. The graph shows how the accelerating voltage changes as the algorithm progressively tunes four cavities of the MLC to resonance in multiple iterations.

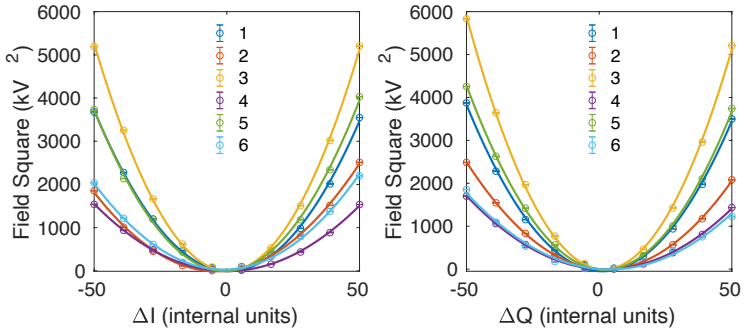

Figure 3.14: Square of the amplitude of parasitic field inside cavities as functions of change in DAC offsets for in-phase ΔI (left panel) and quadrature ΔQ (right panel) components of the output phasor.

tem to drive the vector modulator may have some offset due to manufacturing differences and temperature variations. This leads to some non-zero forward power being injected into the cavity even when the output is set to 0 leading to a parasitic field appearing in the cavity when the feedback loop is not active. To account for the offsets, both the in-phase I and the quadrature Q components of the output phasor are shifted by a programmable offset in the LLRF. We measure the square of amplitude of the parasitic field as a function of offset as shown in Fig. 3.14 setting the optimum value at the position of minimum residual field.

Step 3: The LLRF system implements various trips which turn off rf power going into the cavity in case of a situation which might damage the rf system. Setting the various trip parameters is an important step in commissioning the cavities. There are three categories of trip parameters which we have to set. The *Klystron (SSA)* trip parameters set the threshold for the maximum power reflected from the circulator into the SSA. The *Power* trip parameters are thresholds on the maximum forward and reflected power, while quench detection relies on a sudden but sustained fractional decrease in reflected power. Finally, we set the *Field* trip parameters which control the maximum field tolerated by the system after step 7. The important trip parameters and their usage are listed in Tab. 3.1.

Category	Name	Units	Description
Klystron (SSA)	SSA Reflected Power Scale	kW/count^2	Calibration factor for power reflected from the circulator into the SSA.
	Max. power	kW	Maximum power threshold for *Klystron* trip.
Power	Cavity Forward Power Scale	kW/count^2	Calibration factor for forward power into the cavity.
	Scale Factor Ratio Reflected to Forward		Ratio of reflected and forward power calibration factors.
	Max. Forward Power	kW	Maximum forward power threshold for *Cavity Max Forward* trip.
	Max. Reflected Power	kW	Maximum reflected power threshold for *Cavity Max Reflected* trip.
	Fractional Decrease Trip Level		The fractional decrease threshold for reflected power for a *Cavity Reflected Quench* trip.
	Max. Loop Count	Units of 10μs	Time to wait before declaring a *Cavity Reflected Quench* trip.
Field	Field Square Scale	(kV/count)^2	Calibration factor for square of field.
	Field Amp Square	(kV)^2	Threshold for *Max Cavity Power* trip.

Table 3.1: Trip parameters used in each SRF cavity of the MLC.

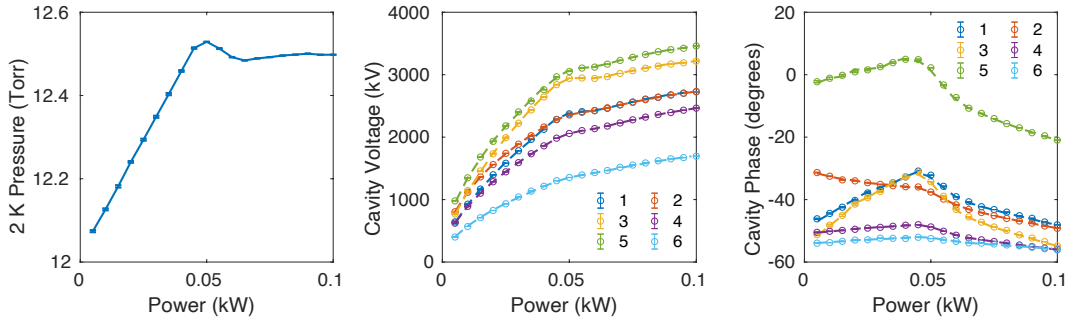

Figure 3.15: Data recorded to measure field rotation. The first panel shows the change in 2 K pressure as we increase the forward power. The second and the third panel show the voltage and phase as functions of forward power respectively on all cavities. The dashed lines represent fits to the data using Eq. (3.6) and (3.7).

Step 4: The phase rotation of the field signal due to the cable length between the field probe and the control system influences the stability of the field control loop. It also directly affects measurement of the tuning angle ϕ_t. Substituting Eq. (3.3) into Eq. (3.5) and including an unknown phase offset ϕ_0, we get

$$\frac{P_+}{V^2} = \frac{\sec^2(\bar{\phi}_t + \phi_0)}{8\frac{R}{Q}Q_L}\,, \tag{3.6}$$

where $\bar{\phi}_t$ is the tuning angle before correction. This relation is used to fit cavity voltage and phase data as a function of forward power as illustrated in Fig. 3.15, with phase offset ϕ_0 being one of the fit parameters. We have incorporated this procedure in our sequencer to set the phase rotation to ensure correct microphonics measurement and optimized field stability.

We can also use this same measurement to characterize LFD and pressure sensitivity of the cavities. Once the unknown phase offsets are determined, we can use it calculate net detuning as functions of cavity voltage V and 2 K Helium vapor pressure p. Consequently, we can fit the detuning to a model,

$$\delta f = \delta f_0 - K_{\mathrm{LFD}}\frac{V^2}{L^2} + \frac{\mathrm{d}f}{\mathrm{d}p}(p - p_0)\,, \tag{3.7}$$

where δf_0 is a constant offset, K_{LFD} is the LFD coefficient, L is the active length

Cavity	Stiffened	df/dp	K_{LFD}
		Hz/Torr	$\mathrm{Hz/(MV/m)^2}$
1	No	37.4 ± 0.6	1.52 ± 0.02
2	Yes	18.3 ± 0.2	1.35 ± 0.01
3	No	47.1 ± 0.4	1.41 ± 0.01
4	Yes	17.4 ± 0.2	1.21 ± 0.01
5	No	38.8 ± 0.4	1.30 ± 0.01
6	Yes	11.7 ± 0.7	1.57 ± 0.08

Table 3.2: Pressure sensitivity and Lorentz Force Detuning coefficients as calculated from cavity voltage and phase data shown in Fig. 3.15.

of the cavity and df/dp is the pressure sensitivity at the nominal pressure p_0 = 12.5 Torr. Typical results from the fit are summarized in Tab. 3.2 which shows that the stiffened cavities are less sensitive to pressure variations while they are equally sensitive to LFD which is consistent with the design.[Posen and Liepe, 2012b]

Step 5: Microphonics poses a major constraint on field stability for the MLC cavities which we operate with high Q_L as noted in the previous section. A tool was developed for the LLRF system which measures microphonics in the system as shown in Fig. 3.16. The LLRF measures the peak forward power and detuning with a time resolution of 10 μsec and 100 μsec respectively. We ensure that the peak microphonics detuning is $\lesssim$ 50 Hz for stable operations while the peak power should be less than the maximum output of the SSA connected to the cavities, 5 kW for stiffened and 10 kW for un-stiffened. If deemed necessary, we can use the spectrum measurement to determine the frequencies of strong vibrations in the cryomodule and then activate the active suppression algorithm on these sources.

Step 6: Jitter in the fundamental mode of the rf cavity depends on the pro-

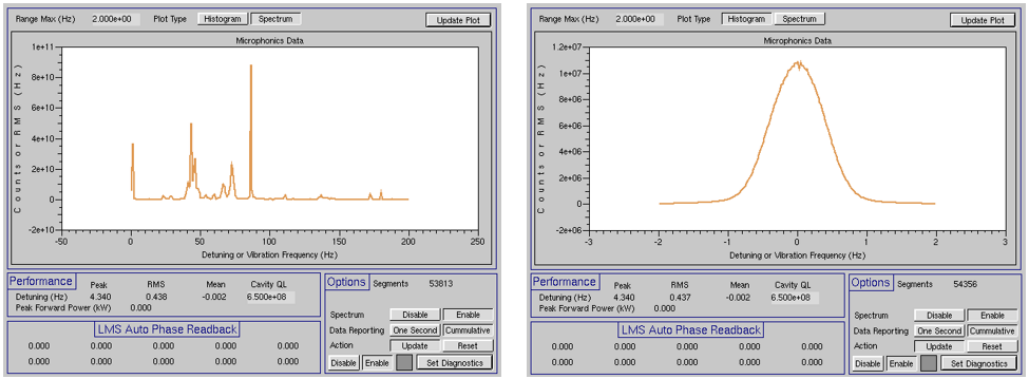

Figure 3.16: LLRF control interface showing microphonics diagnostics running on a piezo sensor signal. The left panel shows the power spectrum while the right shows the histogram of measured values.

portional and integral gains of the field control loop along with the external sources of noise, most notably microphonics detuning. While steps 4 and 5 are completed with some default parameters for the control loop, namely with a normalized proportional gain of 100 and an integral gain of 0, operations with beam need to be optimized. Measurement of standard deviation in field amplitude and phase is necessary to ensure that the energy gained or recovered from the recirculating beam is within tolerances set by the lattice. For CBETA, the field stability measurement relies on data sampled at 12.5 MHz by the LLRF system and is a critical indicator of system performance.

Step 7: Beam based measurements and calibration are the final steps of the initialization process. Finding the phase for maximum acceleration, or the *on-crest phase* is done on a daily basis to account for phase drifts in the rf and clock distribution system. Such a measurement is also used to determine the voltage calibration of the field signal on the LLRF since a purely rf based calibration suffers uncertainties greater then the tolerance of the beam. Beam based measurements are also crucial in checking the alignment and position of the cryomodule with the rest of the beam line. A thorough discussion of these procedures is

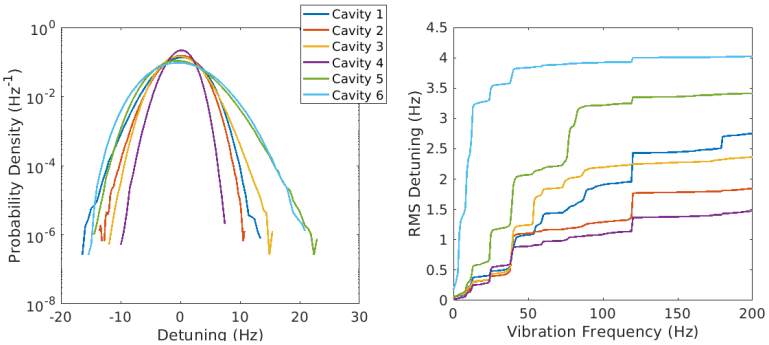

Figure 3.17: Most recent microphonics measurements from the MLC. The left panel shows a histogram of detuning while the right panel shows RMS detuning as a function of vibration frequency.

given in Gulliford et al. [2019].

3.3.3 Performance

Cryogenic stability and microphonics detuning are the most important aspects of narrow bandwidth SRF cryomodule operation. As already stated, the heat dissipation in the MLC when all cavities are operating at their nominal field is well within the limits of using two warm compressors to handle the heat load. A measurement of microphonics detuning in the current stage of commissioning is shown in Fig. 3.17. Table 3.3 compares the original values of peak detuning at the start of commissioning to the current values. Current measurements indicate that peak detuning is limited to 23 Hz among all cavities which is comparable to the cavity bandwidth $f_{1/2} = f_0/Q_L \sim 21.7$ Hz. This enables stable operations with peak power requirements within the capability of the SSAs. The beam on the other hand is primarily sensitive to the accelerating field.

After the control system optimization discussed in the last section, the primary sources of jitter in the accelerating voltage are microphonics detuning and

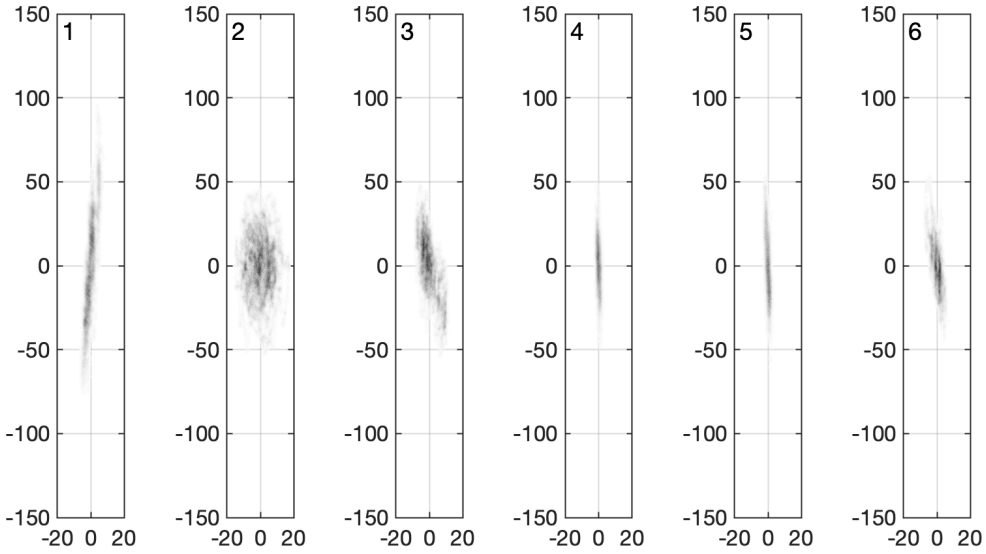

Figure 3.18: Measured probability distribution (darker represents higher probability) of the jitter in voltage phasor in the six cavities of the MLC. The axes are in units of kV.

noise in the measured field. Microphonics detuning primarily gives rise to fluctuations in the phase of the accelerating field leaving the amplitude relatively unaffected. While other sources of noise, such as cross-talk between different LLRF boards or ambient noise result in jitter where the real and complex part are uncorrelated. In order to analyze the sources of fluctuation, a measurement of the probability distribution of the voltage phasor in the MLC cavities is shown in Fig. 3.18. In these plots, the voltage phasor is rotated so that the mean phasor is along the real axis, and the mean is subtracted so that we are only looking at fluctuations around the steady state. The distributions for cavities 4 and 5 correspond to the ideal situation, where microphonics detuning gives rise to phase fluctuations, and hence results in a single streak pattern aligned to the imaginary axis. The small angle between the streaks and the imaginary axis in other cavity data is caused by imperfect setting of phase rotations in step 4 indicating that such observations can be a new method of setting this parameter. Cavities

Cavity	Stiffened	Peak Detuning (Hz)		Voltage (MV)	Amplitude Stability	Phase Stability (degrees)
		Old	New			
1	No	78	17	6 (8.5)	3.9×10^{-4}	0.26
2	Yes	18	15	6 (8.5)	1.0×10^{-3}	0.16
3	No	280	16	6 (9.5)	8.0×10^{-4}	0.18
4	Yes	18	11	6 (10)	1.7×10^{-4}	0.15
5	No	163	23	6 (10)	1.8×10^{-4}	0.17
6	Yes	55	22	6 (10)	4.5×10^{-4}	0.15

Table 3.3: MLC rf performance parameters in the current stage of CBETA commissioning. The values in parenthesis in the voltage column represent the maximum values reached while $\approx$ 6 MV is the design value.

1 and 6 fall under this category, but show larger fluctuations with multiple separated streaks. Cavities 2 and 3 show much larger amplitude fluctuations which are correlated among the real and imaginary axes. Further analysis is needed to understand the cause of these features.

The short term stability and microphonics detuning of the cavities in the MLC are listed in Tab. 3.3. All the cavities have been able to operate at the desired fields to generate a nominal energy gain of 36 MeV in the MLC without many spontaneous trips. In addition, we were able to extract 54 MeV of energy gain from the MLC during a tune scan experiment for the re-circulation loop.[Bartnik et al., 2020] Most rf trips are related to detuning events triggered by the movement of various unrelated devices coupled to the CBETA vacuum chambers such as the path length adjustment system. During operations, drifts in the energy gain of the MLC was observed as orbit drifts in the machine. A measurement of the amplitude of the voltage phasor on cavity 1 as a function of time is shown in Fig. 3.19. While the blue line representing the measurement by the LLRF system stays constant, an alternate source of measurement (orange) shows drifts and sudden changes. During operations orbit measurement has

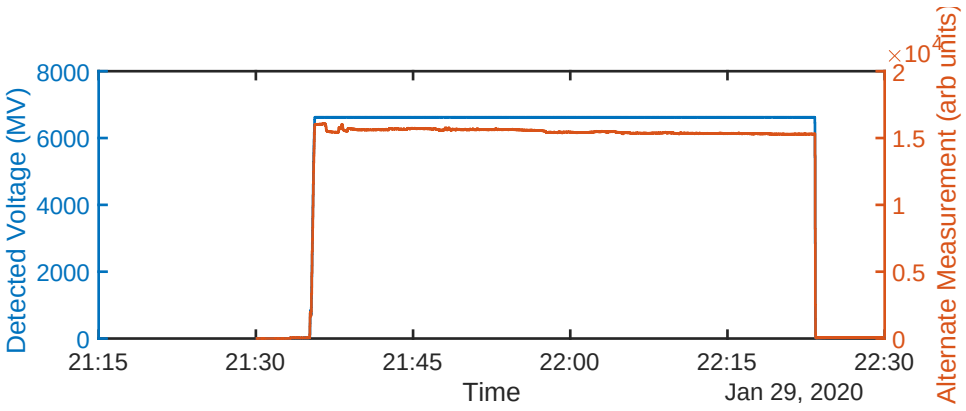

Figure 3.19: Voltage detected by the field control system (blue) and voltage detected by an alternate measurement (orange) for MLC cavity 1 as a function of time.

been used to estimate the energy drift and corrections were applied to the set point of cavity 1 to compensate for this effect. Regardless of these shortcomings in the main linac, CBETA has been operated to demonstrate energy recovery.

3.4 Energy Recovery

The measurement of the energy recovery process in CBETA was done in a 1-turn configuration at a beam current up to 10 μA. The amount of energy transferred to the beam from the fundamental mode can be estimated in terms of the forward power P_+, reflected power P_-, the power dissipated in the cavity walls P_c, the beam current I, and the single particle voltage gain ΔV. Following from the steady state analysis given in Chap. 1, we obtain,

$$P_b = P_+ - P_- - P_c = I \cdot \Delta V \,, \tag{3.8}$$

which follows from Eq. (1.34). The energy gain in this case is $\Delta V = V_c \cos\phi$ where V_c is the cavity voltage and ϕ is the phase of arrival of the particle with

respect to maximum acceleration. In the case of 1-turn energy recovery, the beam is recirculated through the MLC twice resulting in,

$$P_b^{\mathrm{ER}} = P_+ - P_- - P_c = I_\uparrow \Delta V_\uparrow + I_\downarrow \Delta V_\downarrow \,, \tag{3.9}$$

where $I_\uparrow$, $\Delta V_\uparrow$ and $I_\downarrow$, $\Delta V_\downarrow$ are the beam currents and energy gains during the accelerating and deceleration passes respectively. In the case of perfect energy recovery $I_\uparrow = I_\downarrow$ (no beam loss), $\Delta V_\downarrow = -\Delta V_\uparrow$ (no timing error), and the energy recovered from the beam equals the energy delivered during acceleration. The presence of non-zero beam loading P_b^{ER} indicates a departure from the ideal situation.

The power balance efficiency ϵ_P per cavity, as well as the efficiency for the full 1-turn configuration $\epsilon_P^{\text{1-turn}}$ can be defined as, (Eq. (1.37) revisited)

$$\epsilon_P \equiv 1 - \frac{P_b^{\mathrm{ER}}}{P_{b,\uparrow}} \,, \quad \epsilon_P^{\text{1-turn}} \equiv 1 - \frac{\langle P_b^{\mathrm{ER}} \rangle}{\langle P_{b,\uparrow} \rangle} \,, \tag{3.10}$$

where $\langle\rangle$ represents the average over all the cavities in the main linac. It follows from Eq. (3.8) and (3.9) that,

$$P_{b,\uparrow} = I_{inj}(1-\epsilon_\uparrow)\Delta V_\uparrow \,, \quad P_b^{\mathrm{ER}} = I_{inj}(1-\epsilon_\uparrow)\Delta V_\uparrow - I_{inj}(1-\epsilon_\uparrow-\epsilon_\downarrow)(\Delta V_\uparrow + \delta V) \,, \tag{3.11}$$

where I_{inj} is the injector current and we write the voltage gain during deceleration as $\Delta V_\downarrow = -\Delta V_\uparrow - \delta V$ where δV arises from the combination of relativistic effects as well as phasing error, both of which are assumed to be small. The phasing of the beam can be such that both the efficiencies are greater than unity, but beam loss will keep these numbers less than 1 in a real measurement. The fraction of beam lost before the first pass through the MLC and before the second pass are denoted by $\epsilon_\uparrow$ and $\epsilon_\downarrow$ respectively. Since the powers are linearly related to the injector current, an alternative estimate for the efficiencies are,

$$\epsilon_P = 1 - \frac{\partial P_b^{\mathrm{ER}}/\partial I_{inj}}{\partial P_{b,\uparrow}/\partial I_{inj}} \,, \quad \epsilon_P^{\text{1-turn}} = 1 - \frac{\langle \partial P_b^{\mathrm{ER}}/\partial I_{inj} \rangle}{\langle \partial P_{b,\uparrow}/\partial I_{inj} \rangle} \,, \tag{3.12}$$

which exhibit smaller uncertainties since they are an aggregate of power measurements taken at different beam currents. Hence to estimate the power balance efficiency, we need to measure the beam loading as a function of beam current in the accelerating only and the 1-turn energy recovery configuration.

In practice, the measurement of forward and reflected powers is subject to imperfect isolation of the dual directional coupler used to measure them. Accordingly, a forward traveling wave will excite a signal both in the forward coupled port and the reverse coupled port, while the reverse traveling wave will do the same. It can be shown in this case that (see appendix A), the difference between imperfectly measured forward and reflected power is given by,

$$\tilde{P}_+ - \tilde{P}_- = \tilde{P}_c + \chi \Delta V I + \mathrm{O}(I^2)\,, \tag{3.13}$$

where the tilde represent the fact that the quantities generally differ from those in Eq. (3.8) due to the imperfect nature of the dual directional coupler. The term $\tilde{P}_c$ is a constant independent of beam current I and χ is a constant independent of beam current and cavity voltage. The quadratic term here is negligible when we are in the regime of $\frac{I}{V_c}\frac{R}{Q}Q_L << 1$, where Q_L is the loaded quality factor of the cavity. Based on the cavity parameters used in CBETA[Hoffstaetter et al., 2017], we expect $\tilde{P}_+ - \tilde{P}_-$ to be a linear function of beam current up to the order of 10 μA. The power delivered to the beam as determined by the dual directional coupler measurement is thus

$$\tilde{P}_b = \chi I \Delta V + \mathrm{O}(I^2) = \chi P_b + \mathrm{O}(I^2)\,, \tag{3.14}$$

which can be extracted from a measurement of $\tilde{P}_+ - \tilde{P}_-$ as a function of current I. For the estimation of power balance efficiency ϵ_P on a single cavity, χ cancels out, but it is required in the calculation of 1-turn efficiency. The calibration factor χ may be estimated by setting the energy gain of the cavity to a known quantity

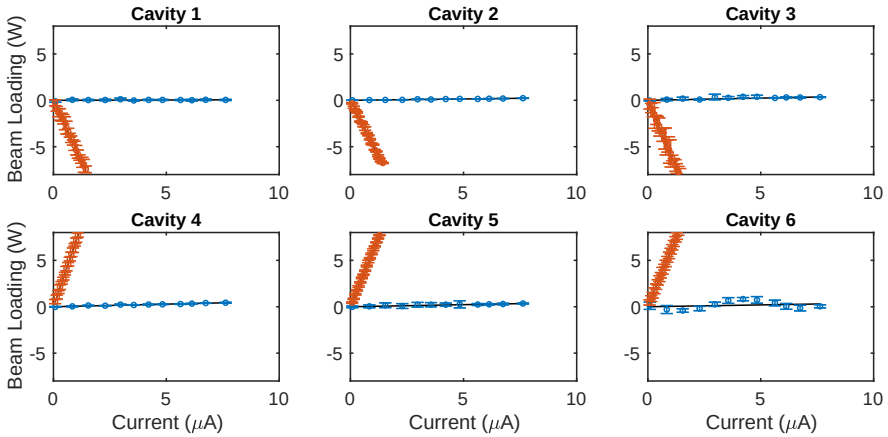

Figure 3.20: Beam loading $\tilde{P}_b$ as a function of current I in all six MLC cavities. Data points in orange indicate loading in the 3 up, 3 down configuration while the blue represents measurements during ER operation. Linear fits to the data are shown in black.

and measuring the beam loading as a function of current. Then the calibration factor can be extracted from the slope as $\chi = (\partial \tilde{P}_b/\partial I)/\Delta V$. Finally, using these values in Eq. (3.12) gives,

$$\epsilon_P^{\text{1-turn}} \approx 1 - \frac{\langle \frac{1}{\chi} \frac{\partial \tilde{P}_b^{\text{ER}}}{\partial I_{inj}} \rangle}{\langle \frac{1}{\chi} \frac{\partial \tilde{P}_{b,\uparrow}}{\partial I_{inj}} \rangle}, \tag{3.15}$$

where we have used Eq. (3.14) to substitute for P_b.

Figure 3.20 shows the beam loading data obtained during μA current operations of CBETA. Beam loading measurements were done for two configurations. In order to measure χ, the first set of measurements shown in orange involved the beam getting accelerated by the first three cavities of the MLC by $\Delta V^{(3\uparrow,3\downarrow)} = 6$ MV each and then getting decelerated by the next three by the same amount. Consequently, the beam was transported from the injector through the MLC directly into the dump. The plots accordingly show a positive slope for cavities 6, 5 and 4 transferring energy to the beam, while 3, 2 and 1 show a negative slope indicating energy recovery. This serves as a calibration measurement to estimate the constants $\chi_i = (\partial \tilde{P}_{b,i}/\partial I)/6$ MV as seen in Eq. (3.13). Table 3.4

Cavity	χ	ϵ_P
6	0.99±0.02	99.2
5	1.004±0.001	99.2
4	1.18±0.01	99.2
3	0.96±0.05	99.2
2	0.809±0.001	99.4
1	0.87±0.03	99.9
1-turn		99.4

Table 3.4: Energy recovery measurements for CBETA in the one turn configuration.[Gulliford et al., 2020]

shows the resulting dual directional coupler coefficients. The estimated uncertainty in the table reflects the uncertainty in the measured slopes, and does not include the error in the assumed 6 MV energy gain/loss per cavity. The beam loading traces shown in blue represents data in the 1-turn energy recovery configuration. The power balance efficiencies for individual cavities are collected in Tab. 3.4 while the net 1-turn efficiency has been measured to be 99.4 % [Gulliford et al., 2020] thus demonstrating energy recovery operation of CBETA in 1-turn. The injector current during 1-turn operation was successfully raised to 70 μA. Even though the average radiation measurements at the permanent magnet arc and outside the shielding perimeter at 70 μA suggested that currents up to 1 mA was achievable, it was deemed unsafe since the fast beam loss monitoring system was not installed yet. It is important to note that all these measurements assume a steady state configuration of the machine. The next chapter explains the operation of high-current ERLs in the presence of transient beam loading.

CHAPTER 4

TRANSIENT BEAM LOADING

The main linacs of SRF ERLs can operate with little average rf power. However the high beam currents in these machines can potentially lead to field transients and subsequent high peak power demands. This chapter explores a novel approach to quantifying transient beam loading valid for arbitrary beam energies and verifies it with the conventional circuit model and experimental data. We use the model to analyze the effect of bunch patterns, current ramps and beam loss while employing CBETA as an example. We predict the existence of reactive beam loading in main linac cavities arising out of relativistic effects at low injection energies even in the presence of perfect energy recovery. Detuning the cavities is one way of minimizing the resulting forward power requirements.

4.1 Introduction

The energy transfer between the beam and the field in the accelerating rf cavities play a vital role in ERL design and operations. In general, when a bunch passes through a resonant structure, it gets accelerated by the electric fields while also exciting wakefields which transfer energy into the various eigenmodes of the cavity. This phenomenon is called *beam loading*. As a simple approximation, fundamental mode beam loading may be calculated as the amount of energy transferred between the bunch and the fundamental eigenmode of the cavity, while energy recovery implies zero average fundamental mode beam loading in all the rf cavities of the main linac. While optimization techniques adjusting cavity voltages, phases and beam re-circulation times can achieve target beam

energies while maintaining zero average fundamental mode beam loading in each cavity during stable operation[Koscica et al., 2019], Higher Order Mode (HOM) beam loading cannot be compensated in this way. The simple approximation using energy transfer has two drawbacks: firstly it does not specify the phase of the electric field exited by the decelerating bunch which is relevant from a field control perspective, and secondly it doesn't address transients in beam current which could arise from special bunch patterns, and common events such as machine turn on, turn off and beam loss. This motivates the need for a dynamic model of beam loading.

To further illustrate the importance of transients, we can estimate the energy transferred to the beam while turning on an ERL. We consider CBETA, which is a four turn (4 accelerating and 4 decelerating passes) machine with a length of the re-circulation arc being $T_p \approx 0.26\,\mu$s for each pass. The main linac houses six SRF cavities with a nominal energy gain of $eV_c \approx 6$ MeV each. If in a hypothetical scenario, we turn on $I = 40$ mA of beam current from the injector all at once, then the beam has to complete 8 passes through the main linac before equilibrium can be established. During this time, the average beam loading from each pass is equivalent to the loading resulting from the acceleration of half of the injection current. As a result, the total energy extracted from a single cavity before achieving equilibrium will be $\mathcal{E}_{\text{beam}} = 0.5I \cdot 4V_c \cdot 8T_p \approx 1$ J. This is comparable to the stored energy of the cavity of about 5.69 J and will lead to a 9.2 % decrease in accelerating field if it remains unchecked. The rf control system not being fast enough to compensate for this rapid dip ($8T_p \approx 2.1\,\mu$s) in accelerating field, will lead to beam loss. In this chapter, we analyze transient beam loading in detail and develop operations procedures necessary for high-current SRF ERL

operation.

Existing methods of modeling beam loading for rf control and stability is based on the notion of shunt impedance and loss factors.[Chao et al., 2013] In the presence of an ultra-relativistic beam, the beam-cavity interaction follows a linear second order differential equation. Commonly, this is modeled as a LRC circuit driven by a current source which stands in for the beam as explained in Chap. 1. Changing the time structure of the source, for instance to account for gaps or special fill patterns, can be used to design optimal rf control in circular machines[Byrd et al., 2002, Yamamoto et al., 2018, Karpov and Baudrenghien, 2019] and design optimal bunch patterns in high energy ERLs.[Setiniyaz et al., 2020] In contrast, many ERLs use low injection energies (5-10 MeV) and hence the first cavity in the path of the beam is subject to bunches which undergo considerable slip in rf phase as it travels through a cavity. For example the injected beam in CBETA gets accelerated from 6 MeV to approximately 12 MeV in the first 7-cell SRF cavity of the main linac in the first pass. During its passage, the bunch slips by $\approx$ 2.9 degrees with respect to the accelerating field which changes the phase of the beam induced voltage and subsequently power requirements, when compared to the ultra-relativistic case. This motivates us to derive a model of beam loading which is valid for arbitrary beam energies.

In the next section, we introduce beam loading from first principles and derive a self-consistent method of calculating the longitudinal dynamics of a bunch passing through a cavity. In section 4.3, we develop a model linear in bunch charge to quantify field transients and power requirements in the main

linac cavities. In section 4.4 we verify the validity of the model by comparing it with experimental data and then apply it to various operational states of the machine.

4.2 Beam Loading

A bunch passing through a resonant cavity, excites electromagnetic field in the cavity and at the same time is acted upon by the electric field inside the cavity. Hence, the field and the charge distribution of the bunch evolve self-consistently as the bunch makes it's way through the cavity. One method of accurately modelling this process is to couple the Finite Difference Time Domain (FDTD) algorithm to calculate fields along with a particle-in-cell (PIC) algorithm to quantify the dynamics of the charge distribution.[Pukhov, 2016] This technique comes with a high computational cost associated with spatially resolving the longitudinal distribution of individual bunches. A procedure which instead tracks the evolution of the cavity eigenmodes self-consistently with the kinematics of the particles in the bunch leads to a practical algorithm to simulate beam loading in accelerating cavities. One documented method involves using the principle of least action to derive a symplectic algorithm which calculates the field inside the cavity.[Abell et al., 2017] In our chapter, we use a simple approach based on a technique first used to describe rf couplers[Condon, 1941], which starts with the Maxwell's equations and ends up with coupled ordinary differential equations for the eigenmodes and the motion of the charged particles.

We first derive the partial differential equation which describes the cavity

field in response to a beam passing through it. We specify the field in terms of the scalar and vector potentials, ϕ and $\vec{A}$ respectively with the usual definitions of electric ($\vec{E}$) and magnetic ($\vec{B}$) field,

$$\vec{E} \equiv -\vec{\nabla}\phi - \frac{\partial \vec{A}}{\partial t}\,, \tag{4.1a}$$

$$\vec{B} \equiv \vec{\nabla} \times \vec{A}\,, \tag{4.1b}$$

while assuming the Coulomb gauge, $\vec{\nabla} \cdot \vec{A} = 0$. Then we plug these definitions into the Maxwell–Ampere equation,

$$\vec{\nabla} \times \vec{B} = \mu_0 \vec{J} + \mu_0 \epsilon_0 \frac{\partial \vec{E}}{\partial t}\,, \tag{4.2}$$

where $\vec{J}$ is the current density inside the cavity and, μ_0 and ϵ_0 are the permeability and permittivity of vacuum respectively. Using the identity $\vec{\nabla} \times \vec{\nabla} \times \vec{A} = \vec{\nabla}(\vec{\nabla} \cdot \vec{A}) - \vec{\nabla}^2 \vec{A}$ and the Coulomb gauge leads to,

$$\frac{1}{c^2}\frac{\partial^2 \vec{A}}{\partial t^2} - \vec{\nabla}^2 \vec{A} = \mu_0 \vec{J} - \frac{1}{c^2}\frac{\partial \vec{\nabla}\phi}{\partial t}\,, \tag{4.3}$$

where c is the speed of light in vacuum and the scalar potential is calculated from Poisson's equation, $\vec{\nabla}^2 \phi = -\rho/\epsilon_0$. Inside a resonant cavity, Eq. (4.3) is subject to boundary conditions which restrict the possible solutions of $\vec{A}$ to a linear superposition of an infinite set of eigenmodes.

In the absence of beam inside the cavity, we can assume that the solution to Eq. (4.3) is of the form $\vec{\mathcal{A}}_k(\vec{r})\mathrm{e}^{i\omega_k t}$, where $\vec{\mathcal{A}}_k$ satisfies

$$\vec{\nabla}^2 \vec{\mathcal{A}}_k + \frac{\omega_k^2}{c^2}\vec{\mathcal{A}}_k = 0\,, \tag{4.4}$$

and is subject to the boundary condition $\vec{\mathcal{A}}_k \times \mathrm{d}\vec{S} = \vec{0}$ at the surface of the cavity denoted by S. The above equation defines a set of orthogonal eigenmodes, and

we choose a normalization so that each mode contains 1 J of stored energy. Since we are considering a lossless system, without the loss of generality, we can assume that $\vec{\mathcal{A}}_k$ is purely real, leading to a simple expression for ortho-normality given by,

$$\frac{\epsilon_0 \omega_k^2}{2} \int \vec{\mathcal{A}}_j \cdot \vec{\mathcal{A}}_k \mathrm{d}V = \delta_{jk} \,. \tag{4.5}$$

Here j and k represent different cavity eigenmodes, while ω_k is the resonant frequency of the mode k. In the presence of beam, the vector potential can be expressed as a superposition of these eigenmodes in the form, $\vec{A}(\vec{r}, t) = \sum_k a_k(t)\vec{\mathcal{A}}_k(\vec{r})$, where $a_k(t)$ are the time-dependent modal amplitudes.

Inserting in the eigenvalue decomposition into Eq. (4.3) yields,

$$\sum_k \Big(\frac{\ddot{a}_k + \omega_k^2 a_k}{c^2} \Big) \vec{\mathcal{A}}_k = \mu_0 \vec{J} - \frac{1}{c^2} \frac{\partial \vec{\nabla} \phi}{\partial t} \,, \tag{4.6}$$

where we have used Eq. (4.4) to substitute for $\vec{\nabla}^2 \vec{A}$. To extract the governing equation for a single eigenmode m, we integrate the dot product of both sides with $\vec{\mathcal{A}}_m$ over the volume of the cavity. This gives,

$$\ddot{a}_m + \omega_m^2 a_m = \frac{\omega_m^2}{2} \int \vec{J} \cdot \vec{\mathcal{A}}_m \, \mathrm{d}V - \frac{\epsilon_0 \omega_m^2}{2} \int \frac{\partial \vec{\nabla} \phi}{\partial t} \cdot \vec{\mathcal{A}}_m \, \mathrm{d}V \,, \tag{4.7}$$

where we have used the ortho-normality relation expressed in Eq. (4.5). This ordinary differential equation in $a_m(t)$ describes the evolution of the eigenmodes driven by arbitrary current distributions inside a resonant cavity and was first used to describe couplers.[Condon, 1941] While the first term is driven by current, the second term represents the field generated by the charge distribution. We can further simplify the second term as,

$$\int \frac{\partial \vec{\nabla} \phi}{\partial t} \cdot \vec{\mathcal{A}}_m \, \mathrm{d}V = \frac{\partial}{\partial t} \int_S \phi \vec{\mathcal{A}}_m \cdot \, \mathrm{d}\vec{S} \,, \tag{4.8}$$

where we have used the vector identity $\vec{\nabla} \cdot (f\vec{A}) = \vec{A} \cdot \vec{\nabla} f + f\vec{\nabla} \cdot \vec{A}$, the Coulomb gauge $\vec{\nabla} \cdot \vec{\mathcal{A}}_m = 0$ and the assumption that the open ports of the cavity including the beam tube and the coupler have extremely low field in their vicinity. The metal which forms the cavity itself, is kept at a constant potential, usually at ground, same as the whole accelerator vacuum system. Since ϕ and $\vec{\mathcal{A}}_m$ are both time independent at the cavity surface, the second term in Eq. (4.7) simplifies to 0. The eigenmode coupling equation reduces to,

$$\ddot{a}_m + \omega_m^2 a_m = \frac{\omega_m^2}{2} \int \vec{J} \cdot \vec{\mathcal{A}}_m \, \mathrm{d}V \,. \tag{4.9}$$

This equation determines the evolution of the fields inside a resonant cavity in response to the passage of beam.

A description for how the fields inside the cavity affect the beam, and as a result the current distribution $\vec{J}(\vec{r})$, is required to complete the model of beam loading. One approach to calculating the current density of a bunched beam is to model it as a collection of many macro-particles each having charge q. A collection of point particles each having position $\vec{r}_p$ and velocity $\vec{v}_p$ give rise to a current density $\vec{J}(\vec{r}, t) = \sum_p q\vec{v}_p \delta(\vec{r} - \vec{r_p})$. In this chapter, we are mostly interested in fundamental mode beam loading, so we can focus our attention to particles traveling along the axis of the cavity having velocities $\vec{v}_p = \dot{z}_p \hat{z}$. Neglecting the current contribution from resistive walls and the input coupler, plugging in the beam current density into Eq. (4.9), we get,

$$\ddot{a}_m + \omega_m^2 a_m = \frac{\omega_m^2}{2} q \sum_p \dot{z}_p \mathcal{A}_{z_m}(z_p(t)) \tag{4.10}$$

where $z_p(t)$ and $\dot{z}_p(t)$ are the time dependent position and velocities of the macro-particles in a 1D model. The motion of the particles are controlled by the total

longitudinal component of the electric field, E_z. The rate of change of energy of a single particle p in the lab frame is given by,

$$mc^2 \frac{\mathrm{d}\gamma_p}{\mathrm{d}t} = qE_z(z_p, t)\dot{z}_p \,, \tag{4.11}$$

where $\gamma_p mc^2$ is the energy of the particle. Neglecting the space charge component $-\vec{\nabla}\phi$, summing the contributions from all eigenmodes and using Eq. (4.1a), the net on-axis electric field is $E_z = -\sum_m \dot{a}_m \mathcal{A}_{z_m}$, where $\mathcal{A}_{z_m}$ is the z-component of the vector potential of mode m. Combining this with Eq. (4.11), we get,

$$\frac{\mathrm{d}\gamma_p}{\mathrm{d}t} = -\frac{q}{mc}\sqrt{1 - \frac{1}{\gamma_p^2}} \sum_m \mathcal{A}_{z_m}(z_p)\dot{a}_m \,, \tag{4.12}$$

where we have used the relation,

$$\frac{\mathrm{d}z_p}{\mathrm{d}t} = c\sqrt{1 - \frac{1}{\gamma_p^2}} \,. \tag{4.13}$$

Eq. (4.10), (4.12) and (4.13) form a self-consistent 1D model of beam loading and longitudinal dynamics inside a resonant cavity.

The eigenmode evolution excited by the beam can also be expressed in terms of the electric field instead of the vector potential formulation put forth in Eq. (4.9). In this case, we consider the eigenmode expansion of the electric field $\vec{E}(\vec{r}, t) = \sum_k e_k(t)\vec{\mathcal{E}}_k(\vec{r})$, where each resonant mode with frequency ω_k satisfies the corresponding Helmholtz equation $\vec{\nabla}^2\vec{\mathcal{E}}_k + \omega_k^2\vec{\mathcal{E}}_k/c^2 = 0$ subject to the boundary conditions $\vec{\mathcal{E}}_k \times \mathrm{d}\vec{S} = 0$. Plugging these into the Maxwell's equations, we obtain:

$$\ddot{e}_m + \omega_m^2 e_m = -\frac{1}{2}\int \frac{\partial \vec{J}}{\partial t} \cdot \vec{\mathcal{E}}_m \,\mathrm{d}V \,, \tag{4.14}$$

where e_m is the modal amplitude and the source term depends on the first time derivative of beam current instead of directly depending on the current itself.

This unfortunately leads to numerical issues, so we use the vector potential formulation in the rest of our chapter.

The transfer of energy between the charged particles and the electromagnetic field inside the cavity is an important aspect of beam loading. To quantify the total energy contained in the field, $\mathcal{E}_{\text{fld}}$, we start with,

$$\mathcal{E}_{\text{fld}} = \frac{\epsilon_0}{2} \int \vec{E} \cdot \vec{E} \, \mathrm{d}V + \frac{1}{2\mu_0} \int \vec{B} \cdot \vec{B} \, \mathrm{d}V \,, \tag{4.15}$$

where we substitute the fields in terms of the potentials. Applying vector identities, the divergence theorem and imposing the boundary conditions, $\mathrm{d}\vec{S} \times \vec{A} = 0$ and $\phi(S) = 0$, we get,

$$\mathcal{E}_{\text{fld}} = \frac{1}{2} \int \phi \rho \, \mathrm{d}V + \frac{\epsilon_0}{2} \int \frac{\partial \vec{A}}{\partial t} \cdot \frac{\partial \vec{A}}{\partial t} \, \mathrm{d}V - \frac{1}{2\mu_0} \int \vec{A} \cdot \vec{\nabla}^2 \vec{A} \, \mathrm{d}V \,. \tag{4.16}$$

Subsequently, we decompose the vector potential $\vec{A}$ into the cavity eigenmodes and simplify using Eq. (4.4) and (4.5) to give,

$$\mathcal{E}_{\text{fld}} = \frac{1}{2} \int \phi \rho \, \mathrm{d}V + \sum_m \left\{ a_m^2 + \frac{\dot{a}_m^2}{\omega_m^2} \right\} . \tag{4.17}$$

The first term is the electric potential energy arising from the charge distribution, while each term in the sum accounts for the energy stored in one unique eigenmode.

A simple application of the 1D model is to calculate the excitation of all the modes in the TM010 pass-band of a multi-cell cavity. In the case of an ultra-relativistic beam, the fundamental mode exhibits a rf phase advance of exactly π radians from cell to cell, which maximizes the energy transferred between the beam and the cavity. However, the other modes in the pass-band could also

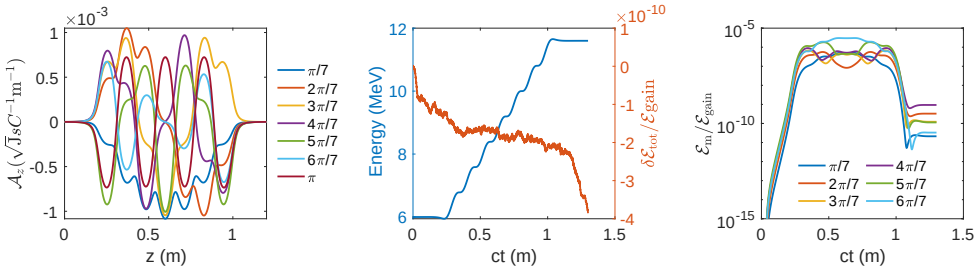

Figure 4.1: TM010 pass-band excitation as a single bunch travels through the first 7-cell cavity used in the main linac of CBETA. The first panel shows the longitudinal component of the vector potential $\mathcal{A}_z$ for the 7 TM010 modes (see Eq. (4.4)). In the second panel, the blue line shows the energy of the bunch as a function of time as it passes through the cavity. The red line shows the numerical fluctuation of total energy of the system, $\delta\mathcal{E}_{\text{tot}}$, as a fraction of net energy gain of the bunch, $\mathcal{E}_{\text{gain}}$. Finally, the third panel shows the evolution of energy contained in the first 6 modes as a fraction of $\mathcal{E}_{\text{gain}}$.

present non-zero beam loading especially in the presence of low energy beams. In CBETA, this situation might occur when the 6 MeV injected beam gets accelerated in the first 7-cell SRF cavity of the main linac[Eichhorn et al., 2015] in the first pass.[Hoffstaetter et al., 2017]. The cavity has it's π-mode tuned to 1300 MHz, and it has six other TM010 modes within 30 MHz of the fundamental. Accordingly, we simulate the passage of a single 6 MeV bunch with charge 123 pC, through a cavity whose π mode is excited according to the design lattice parameters. Figure 4.1 shows the result of this simulation, depicting the evolution of energy of the bunch along with excitation of the first 6 modes. The blue trace in the second panel shows the dynamics of the energy of the bunch as it traverses the cavity. The numerical performance of the model is depicted by the red trace in the second panel, which shows fluctuation of total energy of the system, $\mathcal{E}_{\text{tot}} \equiv \mathcal{E}_{\text{fld}} + \sum_p \gamma_p mc^2$ as a function of time. The third panel shows that among the 6 modes, the $4\pi/7$ mode absorbs the most energy, $\approx 10^{-9}$ times the energy gain of the bunch.

The data in Fig. 4.1 showcases the strengths of the self consistent model of beam loading. Firstly, it includes detailed tracking of the bunch inside the cavity, which replaces the concept of shunt impedance which is only valid for ultra-relativistic beams. In addition, as the energy of the bunch increases during its passage through the cavity, the stored energy in the fundamental mode decreases, with our numerical implementation demonstrating energy conservation at a 10^{-9} level, when compared to the net energy gained by the bunch, $\mathcal{E}_{\text{gain}}$. This clearly demonstrates self consistent evolution of the bunch energy and the cavity field. Further we can conclude that the total energy lost by the bunch into the 6 modes is within the level of numerical noise in the simulation and hence this contribution is exceedingly small when compared to the fundamental accelerating mode. This simple calculation can be extended to include longitudinal higher order modes with non-trivial impedance illustrating the use of this 1D model of beam loading in the context of an ERL.

4.3 RF Model

In this section we characterize the operation of SRF linac cavities, by developing a linearized model of beam loading while including dissipation, the effect of the input coupler and the field control loop.

4.3.1 Linearized Beam Loading

The complete self-consistent model accounting for the change in the cavity field during the transit of the bunch is only relevant when the amount of energy transferred between the beam and an eigenmode, $\mathcal{E}_{gain}$ is comparable to the energy already contained in the mode, $\mathcal{E}_{fld}$. In most situations, including current and proposed ERLs, the amount of energy gained or lost by a single bunch in the main linac cavities is negligible when compared to the stored energy of the fundamental mode i.e. $\mathcal{E}_{gain}/\mathcal{E}_{fld} << 1$. In such a situation, we can solve the self-consistent model, in an iterative fashion, by treating the source term in Eq. (4.10) as a perturbative excitation. Ignoring this excitation and assuming no resonance detuning, we get the 0^{th} order solution $a_m^{(0)}(t)$ given by,

$$a_m^{(0)}(t) \equiv a_m(t_0)\cos\omega_m(t-t_0) + \frac{\dot{a}_m(t_0)}{\omega_m}\sin\omega_m(t-t_0)\,, \tag{4.18}$$

where $a_m(t_0)$ and $\dot{a}_m(t_0)$ are the initial conditions for the eigenmode m at time t_0, just when the bunch enters the cavity. Considering the bunch as a single macro-particle with charge q, plugging this into Eq. (4.12) and (4.13), we get the 0^{th} order solution for the bunch position, $z_p^{(0)}(t)$ and velocity, $\dot{z}_p^{(0)}(t)$. Inserting these solutions into the perturbative source term and solving Eq. (4.10), we get a better approximation for the eigenmode amplitude, $a_m^{(1)}(t)$. This is correct up to the first order of bunch charge and is given by,

$$a_m^{(1)}(t) = a_m^{(0)}(t) + \frac{q\omega_m}{2}u(t-t_0)\int_{t_0}^{t}\mathcal{A}_{z_m}(z_p^{(0)}(\tau))\dot{z}_p^{(0)}(\tau)\sin\omega_m(t-\tau)\,\mathrm{d}\tau\,, \tag{4.19}$$

where the second term represents the impulse response of the system to the passage of a single bunch with charge q and $u(t)$ is the Heaviside step function. In order to compactly represent the dynamics, we define a mode phasor $\tilde{\mathcal{F}}_m(t)$ as

$$\tilde{\mathcal{F}}_m(t) \equiv \{\dot{a}_m(t) + i\omega_m a_m(t)\}\mathrm{e}^{-i\omega_m t}\,, \tag{4.20}$$

which is valid for $t > 0$. The mode phasor remains constant in a loss-less cavity, only getting perturbed by a passing bunch which generates an excitation $\tilde{\mathcal{G}}_m$, defined as,

$$\tilde{\mathcal{G}}_m(t) \equiv \frac{\omega_m^2 u(t-t_0)}{2} \int_0^{t-t_0} \mathcal{A}_{z_m}(z_p^{(0)}(t_0+\tau))\dot{z}_p^{(0)}(t_0+\tau)\mathrm{e}^{-i\omega_m(t_0+\tau)}\,\mathrm{d}\tau\,. \tag{4.21}$$

Using the definitions of the mode phasor $\tilde{\mathcal{F}}_m$ and the single bunch excitation $\tilde{\mathcal{G}}_m$, we can represent the first order solution in Eq. (4.19) as,

$$\tilde{\mathcal{F}}_m(t) = \tilde{\mathcal{F}}_m(t_0) + q\tilde{\mathcal{G}}_m(t)\,. \tag{4.22}$$

The linear model is easily extendable to the passage of multiple bunches through the cavity, since individual perturbations $\tilde{\mathcal{G}}_m$ on the eigenmode can be linearly superimposed to yield a full time dependent solution of the fields.

The energy transferred to the bunch under this linear approximation is important in characterizing the energy recovery process. The work done by the electric field on a bunch with charge q is,

$$\mathcal{E}_{gain} = q\int_0^T E_z(z_p(t_0+\tau), t_0+\tau)\dot{z}_p(t_0+\tau)\,\mathrm{d}\tau\,, \tag{4.23}$$

where t_0 and T are the time of entry and the transit time of the bunch respectively. Assuming that the fundamental mode is the major contribution to the accelerating field, we can approximate the longitudinal electric field as $E_z(z,t) \approx -\dot{a}_0(t)\mathcal{A}_{z_0}(z)$, where the subscript 0 denotes the fundamental mode. Using the linear approximation for eigenmode amplitude in Eq. (4.19) and expanding E_z, we get,

$$\begin{aligned}\mathcal{E}_{gain} = &-q\mathcal{R}\Big[\{\dot{a}_0(t_0) + i\omega_0 a_0(t_0)\}\mathrm{e}^{-i\omega_0 t_0}\int_0^T \mathcal{A}_{z_0}(z_p^{(0)}(t_0+\tau))\dot{z}_p^{(0)}(t_0+\tau)\mathrm{e}^{i\omega_0(\tau+t_0)}\,\mathrm{d}\tau\Big] \\ &-\frac{\omega_0^2 q^2}{4}\left|\int_0^T \mathcal{A}_{z_0}(z_p^{(0)}(t_0+\tau))\dot{z}_p^{(0)}(t_0+\tau)\mathrm{e}^{-i\omega_0(\tau+t_0)}\,\mathrm{d}\tau\right|^2,\end{aligned} \tag{4.24}$$

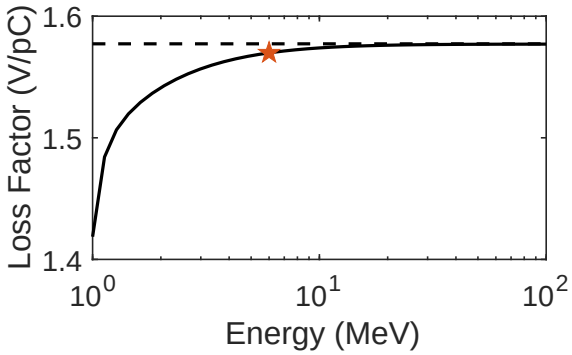

Figure 4.2: Fundamental mode loss factor as a function of incident energy for the first main linac cavity of CBETA. The dashed line represents the ultra-relativistic value of loss factor calculated from the shunt impedance the cavity, while the solid black line represents the result from the linear model. The star represents the nominal operating point of the cavity as used in CBETA.

where $\mathcal{R}[]$ represents the real part of the complex number. Using Eq. (4.20) and (4.21), we can represent the energy gain with,

$$\mathcal{E}_{gain} = -\frac{2q}{\omega_0^2}\mathcal{R}\{\tilde{\mathcal{F}}_0\tilde{\mathcal{G}}_0^*(T)\} - \frac{q^2|\tilde{\mathcal{G}}_0(T)|^2}{\omega_0^2}, \tag{4.25}$$

where $\tilde{\mathcal{G}}_0(T)$ is net excitation of the fundamental mode after the bunch passes through the cavity. The energy gain in the linear approximation consists of two terms, the first term which is linear in bunch charge, dominates. The second term quadratic in charge accounts for the energy lost to the longitudinal wake-field, which we identify as $k_0 q^2$, where $k_0 \equiv |\tilde{\mathcal{G}}_0(T)|^2/\omega_0^2$ is the loss factor[Chao et al., 2013] corresponding to the fundamental mode. This model accurately considers the effect of a low energy beam up to second order of charge.

The linearized model gives a direct method of calculating the change of the modal amplitudes induced by a passing bunch irrespective of particle energy. While this is used later in the chapter to estimate rf power requirements for op-

erating an ERL, it can also be used to calculate the variation of modal loss factor as a function of energy. In the ultra-relativistic limit, the fundamental mode loss factor may be calculated as $k_0 = 0.5\omega_0 R/Q$, where R/Q is the ratio of the shunt impedance and the quality factor of the eigenmode. Figure 4.2 illustrates this with the first 7-cell SRF cavity used in the main linac of CBETA. The fundamental mode loss factor is a monotonous increasing function of energy, eventually reaching the ultra-relativistic value shown as the dashed line, while the star represents the operating point for the cavity. The mismatch between the phase velocity of the mode and the velocity of the bunch results in the lower value of loss factors for low energies. Even though the energy lost by a single bunch due to this effect is very small, the net change in the modal phasor is non-trivial and needs to be compensated by the control system.

4.3.2 Dissipation and Input Coupling

A real SRF main linac is subject to losses at the cavity walls and at the fundamental power coupler, hence a model incorporating these effects along with the action of the rf control system is necessary to analyze ERL operation. The cavity wall and the coupler give rise to two additional source terms in Eq. (4.9). The current density flowing through the cavity wall denoted by $\vec{J}_{\text{wall}}(\vec{r})$ causes an average power dissipation, defined as $< P_{\text{wall}} > \equiv \omega_0 U_0/Q_0$, where U_0 is the energy stored in the fundamental mode of the cavity and Q_0 is called the intrinsic quality factor of the cavity. The time averaged heat dissipated in the walls caused by the fundamental mode depends on the electric field through the relation, $< P_{\text{wall}} > = < \int \vec{J}_{\text{wall}} \cdot \vec{E}_0 \, \mathrm{d}V >$. Combining the different expressions for

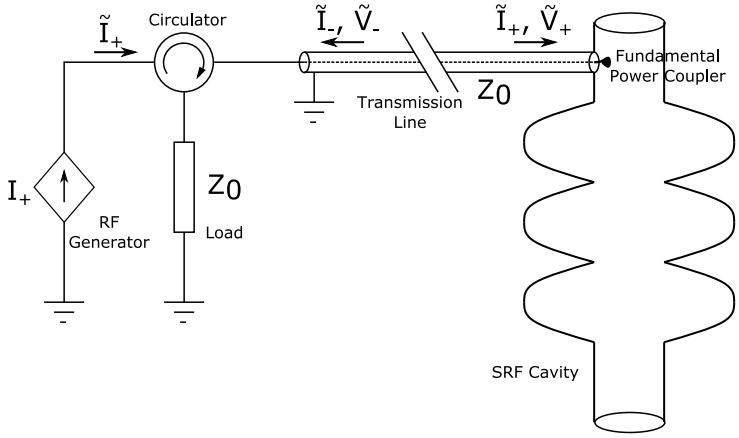

Figure 4.3: Schematic of the transmission line model for a fundamental input coupler feeding into a SRF cavity. (Fig. 1.5 revisited.)

power dissipation in a situation, when the fundamental mode contains $U_0 = 1$ J of energy, gives a relation,

$$\int \sigma(\vec{r})|\vec{\mathcal{A}}_0|^2(\vec{r})\,\mathrm{d}V = \frac{2}{\omega_0 Q_0}\,, \tag{4.26}$$

where $\sigma(\vec{r})$ is the electrical conductivity of the walls. This calculation allows us to simplify the source term due to dissipation in the cavity walls to,

$$\frac{\omega_0^2}{2}\int \vec{J}_{\text{wall}}\cdot\vec{\mathcal{A}}_0\,\mathrm{d}V = -\frac{\omega_0\dot{a}_0}{Q_0}\,, \tag{4.27}$$

which gives our first damping term to the otherwise loss-less system.

The fundamental power coupler injects energy into the cavity while introducing more dissipation. We augment our existing description of beam loading with a transmission line model of the coupler as depicted in Fig. 4.3. The rf generator is represented as a controlled source generating current $I_+(t)$ which propagates through a circulator into a waveguide connecting to the coupler.

Inside the transmission line with characteristic impedance of Z_0, the propagating waves are denoted using their corresponding current and voltage phasors. These are $\tilde{I}_+$, $\tilde{V}_+$ and $\tilde{I}_-$, $\tilde{V}_-$ for the forward and the reflected traveling waves respectively with their phases referenced to the coupler tip. The load resistor connected to the circulator is matched to the transmission line and has the same characteristic impedance Z_0, thus acing as a sink for the wave reflected from the cavity. The current induced in the coupler tip $\vec{J}_{\text{coup}}$ gives rise to a new source term for Eq. (4.9), defined as:

$$\frac{\omega_0^2}{2} \int \vec{J}_{\text{coup}}(\vec{r}, t) \cdot \vec{\mathcal{A}}_0 \, \mathrm{d}V \equiv \frac{\omega_0^2 \kappa_{\text{coup}} I_{\text{coup}}(t)}{2} \,, \tag{4.28}$$

where I_{coup} is the net current in the transmission line flowing towards the cavity and κ_{coup} is a real constant which depends on the coupler geometry. Taking the time derivative of the fundamental mode energy term in Eq. (4.17), we can calculate the the power transferred into the fundamental mode as $P_0 = \kappa_{\text{coup}} \dot{a}_0 I_{\text{coup}}$, where we have used Eq. (4.9) to eliminate $\ddot{a}_0$. Comparing this expression of power to $P_0 = I_{\text{coup}} V_{\text{coup}}$, we can quantify the voltage at the coupler tip as $V_{\text{coup}} = \kappa_{\text{coup}} \dot{a}_0$. The relationships between the eigenmode amplitudes and the transmission line quantities I_{coup} and V_{coup} make it possible to construct a complete model for evaluating forward power requirements in the presence of beam loading.

The potential difference between the coupler tip and the outer conductor of the transmission line can be treated as a superposition of the forward and reverse traveling waves as $V_{\text{coup}}(t) = \mathcal{R}\{(\tilde{V}_+ + \tilde{V}_-)\mathrm{e}^{i\omega_0 t}\}$. Substituting for $\tilde{V}_+$ and $\tilde{V}_-$ using the corresponding current phasors and $V_{\text{coup}} = \kappa_{\text{coup}} \dot{a}_0$, we get $I_-(t) = \kappa_{\text{coup}} \dot{a}_0 / Z_0 - I_+(t)$, where we used the phasor definitions $I_\pm(t) \equiv \mathcal{R}\{\tilde{I}_\pm \mathrm{e}^{i\omega_0 t}\}$. Combining this expression of I_- with the definition of net current traveling through

the transmission line into the cavity ($I_{\text{coup}} = I_+ - I_-$), we get,

$$I_{\text{coup}}(t) = 2I_+(t) - \frac{\kappa_{\text{coup}}\dot{a}_0}{Z_0}\,, \tag{4.29}$$

Plugging this into Eq. (4.28) yields two source terms: $\omega_0^2\kappa_{\text{coup}}I_+(t)$ which is the contribution from the rf power source and $-\omega_0^2\kappa_{\text{coup}}^2\dot{a}_0/(2Z_0)$ which is a dissipative term accounting for the power emitted from the fundamental mode through the power coupler. The external quality factor Q_{ext} is used to quantify the amount of dissipation in a manner similar to Eq. (4.27). This allows us to estimate the unknown parameter κ_{coup} as,

$$\kappa_{\text{coup}} = \sqrt{\frac{2Z_0}{\omega_0 Q_{ext}}}\,. \tag{4.30}$$

Combining Eq. (4.10), (4.27), (4.28), (4.29) and (4.30), we get the complete rf model:

$$\ddot{a}_0 + \frac{\omega_0\dot{a}_0}{Q_L} + \omega_0^2 a_0 = \frac{\omega_m^2}{2}q\sum_p \dot{z}_p\mathcal{A}_{z_m}(z_p(t)) + \sqrt{\frac{2Z_0\omega_0^3}{Q_{ext}}}I_+(t)\,, \tag{4.31}$$

where we have defined the loaded quality factor as $Q_L^{-1} \equiv Q_0^{-1} + Q_{ext}^{-1}$. The power generated by the rf source corresponding to the source term is $P_+ = I_+^2 Z_0$. Quantifying the actual power required by the control system to maintain stable field during ERL operation requires a description of the control loop in addition to the transmission line model of the coupler.

4.3.3 Control and Power Requirements

The purpose of active control in SRF Linacs is to damp perturbations of the accelerating field inside a cavity when it is subject to disturbances from the beam, mechanical detuning or drifts in the system. In the case of SRF cavities operating with high Q_L, simple high gain proportional feedback is commonly used

to stabilize the field[Wibowo et al., 2018] along with automatic resonance control in the presence of large unmitigated microphonics detuning.[Banerjee et al., 2019] An ideal implementation of the feedback loop not accounting for finite bandwidth or signal propagation delays can be written as:

$$\sqrt{\frac{2Z_0\omega_0^3}{Q_{ext}}}I_+(t) = \frac{\omega_0 K_p}{Q_L}\mathcal{R}\{(\tilde{\mathcal{F}}_{sp} - \tilde{\mathcal{F}}_0(t))e^{i\omega_0 t}\}\,, \tag{4.32}$$

where K_p is the dimensionless proportional gain, $\tilde{\mathcal{F}}_{sp}$ is the phasor set point and $\tilde{\mathcal{F}}_0(t)$ is the fundamental mode phasor. Enforcing this feedback loop in the rf system gives an effective description of the response of accelerating field towards perturbations. Accordingly, plugging in Eq. (4.32) into Eq. (4.31) gives:

$$\ddot{a}_0 + (1+K_p)\frac{\omega_0\dot{a}_0}{Q_L} + \omega_0^2 a_0 = \frac{\omega_m^2}{2}q\sum_p \dot{z}_p\mathcal{A}_{z_m}(z_p(t)) + \frac{\omega_0 K_p}{Q_L}\mathcal{R}\{\tilde{\mathcal{F}}_{sp}e^{i\omega_0 t}\}\,, \tag{4.33}$$

where the control system effectively enhances dissipation, leading to faster decay of fluctuations.

In the absence of any excitation from the beam and no resonance detuning, the steady state of the system can be estimated by assuming $\ddot{a}_0 + \omega_0^2 a_0 = 0$ in Eq. (4.33) to yield,

$$\tilde{\mathcal{F}}_0(t\to\infty) = \frac{K_p\tilde{\mathcal{F}}_{sp}}{1+K_p}\,, \tag{4.34}$$

where the fundamental mode phasor always tends to settle at the value given by $\tilde{\mathcal{F}}_0(t\to\infty)$ as it recovers from a perturbation. The time dependent behavior of the phasor in the presence of the dissipative term is given by,

$$\tilde{\mathcal{F}}_0(t) = \tilde{\mathcal{F}}_0(t_0) + q\tilde{\mathcal{G}}_0(T)e^{-(1+K_p)\frac{\omega_0}{2Q_L}(t-t_0)}\,, \tag{4.35}$$

where t_0 is the time of entry and $q\tilde{\mathcal{G}}_0(T)$ is the net excitation to the fundamental mode, when a single bunch passes through the cavity as given by Eq. (4.21).

This equation valid for $t - t_0 >> T$ can be used to linearly combine the effect of a bunch train passing through the cavity. The power required by the control system to compensate for the disturbance is:

$$< P_+ >=< I_+^2 > Z_0 = \frac{K_p^2 Q_{ext}}{4\omega_0 Q_L^2} |\tilde{\mathcal{F}}_{sp} - \tilde{\mathcal{F}}_0(t)|^2 \,, \tag{4.36}$$

where we have combined the loop output given in Eq. (4.32) with the definition of forward power $P_+ = I_+^2 Z_0$. Equations (4.21), (4.34), (4.35) and (4.36) form the basis of our estimations of power requirements in multi-turn ERLs.

4.4 Results

The linear model derived in the previous section can be used to describe beam loading and power requirements for arbitrary bunch patterns. However, we first determine a relation between the mode phasor $\tilde{\mathcal{F}}_m$ and commonly used cavity parameters. Using Eq. (4.17) and (4.20), the stored energy in the fundamental mode is,

$$U_0 = a_0^2 + \frac{\dot{a}_0^2}{\omega_0^2} = \frac{|\tilde{\mathcal{F}}_0|^2}{\omega_0^2} \,. \tag{4.37}$$

Equivalently, the fundamental mode amplitude is commonly expressed in terms of cavity voltage V_c, which is the maximum energy gain of an ultra-relativistic particle when it passes though the cavity. The energy in the fundamental mode can be written in terms of V_c as $U_0 = V_c^2/(2\omega_0 R/Q)$, where R/Q is the ratio of shunt impedance and the quality factor. Comparing these two definitions of stored energy, we get the amplitude of the mode phasor as,

$$|\tilde{\mathcal{F}}_0| = \sqrt{\frac{\omega_0}{2R/Q}} V_c \,, \tag{4.38}$$

while the proper phase can be determined by evaluating the on-crest phase of the fundamental mode and then adding the corresponding bunch phase ϕ. Now

we apply this model to various scenarios of cavity operation.

4.4.1 Normal Linac Operation

In the presence of a regular bunch pattern, we can analytically determine the mean forward power consumption in the absence of microphonics. Following from Eq. (4.35), the time averaged value of the fundamental mode phasor is given by,

$$< \tilde{\mathcal{F}}_0 >= \frac{K_p \tilde{\mathcal{F}}_{sp}}{1+K_p} + < q \sum_p [\tilde{\mathcal{G}}_0(T)]_p \mathrm{e}^{-(1+K_p)\frac{\omega_0}{2Q_L}(t-t_p)} > , \tag{4.39}$$

where <> represents the time average, the first term is the steady state phasor in the absence of beam (Eq. (4.34)) and $[\tilde{\mathcal{G}}_0(T)]_p$ represents the phasor induced by bunch p which enters the cavity at time t_p. If all bunches are phased exactly the same with respect to the fundamental mode, then the second term simplifies as,

$$< q \sum_p [\tilde{\mathcal{G}}_0(T)]_p \mathrm{e}^{-(1+K_p)\frac{\omega_0}{2Q_L}(t-t_p)} >= \frac{2 I_b Q_L}{\omega_0 (1+K_p)} \tilde{\mathcal{G}}_0(T) , \tag{4.40}$$

where for a total number of bunches N_b, the relationship $< q N_b \mathrm{e}^{-t/\tau} >= I_b \tau$ holds with I_b representing the average beam current. Plugging in the average phasor into Eq. (4.36) yields the forward power as,

$$P_+ = \frac{Q_{ext}}{4\omega_0 Q_L^2} \left| \tilde{\mathcal{F}}_0(t \to \infty) - \frac{2 I_b Q_L K_p}{\omega_0 (1+K_p)} \tilde{\mathcal{G}}_0(T) \right|^2 , \tag{4.41}$$

where we have substituted the set point $\tilde{\mathcal{F}}_{sp}$ in terms of $\tilde{\mathcal{F}}_0(t \to \infty)$. In the presence of high feedback gain K_p and low beam currents, this simplifies to,

$$P_+ \approx \frac{V_c^2 Q_{ext}}{8 \frac{R}{Q} Q_L^2} - \frac{Q_{ext}}{Q_L} I_b \frac{\mathcal{R}\{\tilde{\mathcal{F}}_0(t \to \infty) \tilde{\mathcal{G}}_0^*(T)\}}{\omega_0^2} , \tag{4.42}$$

where we have used Eq. (4.38) to write the first term in terms of the steady state cavity voltage V_c. The forward power consists of a constant term accounting for

dissipation and a term linear in beam current representing power transferred to the beam.

We can use the above result to verify our linear model with low current measurements of beam loading for the main linac cavities of CBETA, and also compare with the predictions of the circuit model. Using Eq. (1.34), the forward power required to operate a perfectly tuned standing wave linac ($\omega = \omega_0$) in the presence of beam is given by,

$$\begin{aligned} P_+ &= \frac{V_c^2}{8\frac{R}{Q}Q_L}\frac{(1+\beta)}{\beta}\left\{\left(1+\frac{2I_b}{V_c}\frac{R}{Q}Q_L\cos\phi\right)^2+\left(\frac{2I_b}{V_c}\frac{R}{Q}Q_L\sin\phi\right)^2\right\} \\ &\approx \frac{V_c^2}{8\frac{R}{Q}Q_L}\frac{(1+\beta)}{\beta}+\frac{\beta+1}{2\beta}I_b V_c\cos\phi\,, \end{aligned} \tag{4.43}$$

where $\beta \equiv Q_0/Q_{ext}$, $I_b = I_{\text{beam}}/2$ is the average beam current and ϕ is the phase of arrival of the bunch with respect to the phase of maximum energy gain. The expression for forward power from the circuit model matches with the linear model derived in this chapter except for the different ways for quantifying energy transferred by a bunch into the cavity.

Figure 4.4 shows measurements of forward power at the CBETA main linac in the presence of low beam current. In this measurement, cavities 6, 5 and 4 accelerate the beam by about 6 MeV each, while cavities 3, 2 and 1 decelerate the beam by the same amount. The calibration factors for the power measurement and the loaded quality factors Q_L of the cavities were unknowns during this experiment. By fitting the power estimations from both models to the experimental data, we obtained these unknown parameters. The estimated values of Q_L range between 4.9×10^7 to 5.6×10^7 compared to the nominal design value of 6×10^7 for the cavities accelerating the beam. However in the case of decel-

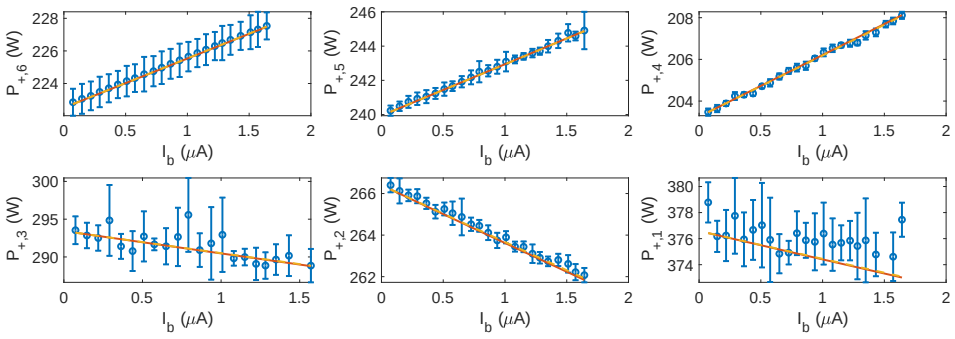

Figure 4.4: Average forward power as a function of beam current for the six main linac cavities of CBETA in the up-down configuration. The blue circles with error bars represent observed data, while the solid red and the dashed yellow lines represent power estimations from the linearized model and the circuit model respectively.

eration, the measurements for cavities 3 (bottom left) and 1 (bottom right) are quite noisy due the presence of substantial microphonics detuning measured on them. Within the measurement uncertainty both models are consistent with the data while being virtually indistinguishable from one another.

4.4.2 Stable Energy Recovery

In the presence of a regular bunch pattern with little gap, phased for perfect energy recovery in each cavity, the dynamics of the equilibrium mode phasor is dominated by resonance detuning. We use linear superposition of the rf excitation from the source and from the beam to analyze the net mode phasor. When the detuning $\delta\omega$ is small compared to the resonance frequency of the cavity, the induced phasor from a single bunch rotates in time with respect to the phasor coordinate system and becomes $\tilde{\mathcal{G}}_0(T)\exp\{i\delta\omega(t-t_0)\}$ for $t - t_0 >> T$ where $\tilde{\mathcal{G}}_0(t)$

is defined in Eq. (4.21). The time averaged contribution from the injected beam current I_{inj} is,

$$< q \sum_p [\tilde{\mathcal{G}}_0(T)]_p e^{\{i\delta\omega - (1+K_p)\omega_{1/2}\}(t-t_p)} >= \frac{I_{inj} \sum_p [\tilde{\mathcal{G}}_0(T)]_p}{\omega_{1/2}(1+K_p) - i\delta\omega}\,, \tag{4.44}$$

which is similar to Eq. (4.40) except for a phase shift due to detuning and we have defined the half-bandwidth as $\omega_{1/2} \equiv 0.5\omega_0/Q_L$. In the same way, the steady state in the absence of beam also gets a phase shift from detuning which may be explained by examining the LHS of Eq. (4.33) which is given by,

$$\ddot{a}_0 + (1+K_p)\frac{\omega_0 \dot{a}_0}{Q_L} + (\omega_0 + \delta\omega)^2 a_0 \approx \mathcal{R}\Big[\tilde{\mathcal{F}}_0\Big\{\frac{\omega_0}{Q_L}(1+K_p) - 2i\delta\omega\Big\}e^{i\omega_0 t}\Big], \tag{4.45}$$

where we have assumed a constant detuning $\delta\omega << \omega$. Equating this with the steady source term $\omega_0 K_p \mathcal{R}\{\tilde{\mathcal{F}}_{sp} e^{i\omega_0 t}\}/Q_L$, and adding the contribution from the beam, we obtain,

$$< \tilde{\mathcal{F}}_0 >= \frac{K_p \tilde{\mathcal{F}}_{sp}}{1 + K_p - i\frac{\delta\omega}{\omega_{1/2}}} + \frac{I_{inj} \sum_p [\tilde{\mathcal{G}}_0(T)]_p}{\omega_{1/2}(1+K_p) - i\delta\omega}\,. \tag{4.46}$$

The control loop effectively reduces the effect of the recirculating bunches on the accelerating field inside the cavity by a factor of approximately $1 + K_p$.

The net phasor induced by the recirculating bunches determines the equilibrium beam loading of the fundamental mode. Figure 4.5 shows the phasors induced by the recirculating bunches in the first main linac cavity of CBETA in two phasing configurations. The amplitudes are scaled as $\chi_p \equiv q\sqrt{\omega_0/(2R/Q)}[\tilde{\mathcal{G}}_0(T)]_p$ for convenience and the phases are referenced to the time averaged phasor of the fundamental mode. The first panel shows the induced phasors from the 8 recirculating bunches (4 accelerating and 4 decelerating) each receiving an exact energy gain or loss of 6 MeV. The second panel shows the induced phasors from the 8 recirculating bunches phased according to the baseline design lattice

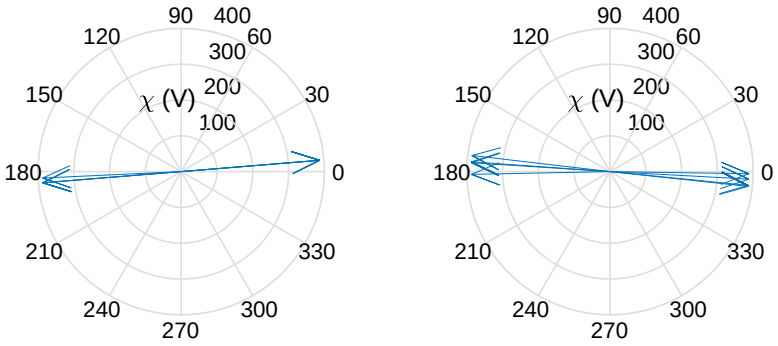

Figure 4.5: Fundamental mode phasors induced by the recirculating bunches in the first main linac cavity of CBETA with the phases referenced to the cavity set point phasor. The left plot represents an ideal phasing condition with perfect energy recovery while the right uses settings from the current design lattice of CBETA.

of CBETA. The imaginary component of the resultant phasor $\sum_p \chi_p$ in the two cases are 14.6 V and -17.2 V for the ideal phasing and the baseline design respectively. The substantial imaginary component of the resultant phasor indicates that the beam tends to rotate the mode phasor with respect to the average thus creating a reactive load for the rf power source.

In the absence of stored energy inside the fundamental mode, a bunch passing through the cavity excites field phased for maximum deceleration, since all the energy transferred from the bunch has to be injected into the induced field. The phase of maximum deceleration depends on the velocity of the bunch as it travels through the cavity. Under the first order approximation in bunch charge used in this chapter, existing field inside the cavity gives rise to a modified velocity profile $\dot{z}_p^{(0)}$, which changes the phase for maximum deceleration and by extension the induced phasor. Hence the resultant phasor depends on the phas-

ing of the beam with respect to the fundamental mode. At higher energies, the beam becomes more rigid resulting in a velocity profile closer to the speed of light, which keeps this phase constant. As a result only the first and the last cavity of the CBETA main linac for instance have an appreciable amount of reactive beam loading. In order to compensate for the rotation in the mode phasor, the control loop would use additional power to keep the phasor near the set-point, about 36.5 kW for the baseline phasing of the first cavity in the CBETA main linac (right panel in Fig. 4.5). To reduce power requirements during stable operations, the imaginary component of the net induced phasor may be mitigated either by optimal phasing or by detuning the cavity.

Detuning a cavity changes the effective response of the fundamental mode phasor to the forward power phasor emitted from the rf source.[Padamsee et al., 2008] While this impedance approach is used to calculate optimum detuning for cavities operating in storage rings, we use an equivalent approach using mode phasors. The net effect of beam loading can be encoded into a complex angular frequency given by,

$$\omega_{l,r} + i\omega_{l,i} \equiv \frac{I_{inj}}{< \tilde{\mathcal{F}}_0 >} \sum_p [\tilde{\mathcal{G}}_0(T)]_p \tag{4.47}$$

where the phasor is referenced to the steady state accelerating field inside the cavity. Using this definition in Eq. (4.46) and rearranging we get,

$$\frac{< \tilde{\mathcal{F}}_0 >}{\tilde{\mathcal{F}}_{sp}} = \frac{K_p}{1 + K_p - \frac{\omega_{l,r} + i(\omega_{l,i} + \delta\omega)}{\omega_{1/2}}} \,. \tag{4.48}$$

To compensate for reactive beam loading, the time averaged mode phasor $< \tilde{\mathcal{F}}_0 >$ should exactly be in the same direction as the set point phasor $\tilde{\mathcal{F}}_{sp}$, i.e $\mathcal{I}\{< \tilde{\mathcal{F}}_0 > / \tilde{\mathcal{F}}_{sp}\} = 0$, where $\mathcal{I}\{\}$ represents the imaginary part of the complex argument. The amount of detuning required to enforce this constraint is $\delta\omega_{opt} =$

$-\omega_{l,i}$. The required detuning for the two situations in Fig. 4.5 are approximately -125 Hz and 158 Hz respectively. In practice, an automatic tuning system which can change the resonance frequency of the cavity in response to reactive loading is required for stable operations with little available rf power.

Microphonics detuning dominates the power requirements during steady state ERL operations once reactive beam loading is counteracted. The equilibrium mode phasor in the presence of constant detuning $\delta\omega = \delta\omega_{opt} + \delta\omega_{ext}$ is given by,

$$< \tilde{\mathcal{F}}_0 >= \frac{K_p}{1 + K_p - \frac{\omega_{l,r} + i\delta\omega_{ext}}{\omega_{1/2}}} \tilde{\mathcal{F}}_{sp}\,, \tag{4.49}$$

which follows from Eq. (4.48) under the assumption of perfect compensation of reactive loading. Assuming high proportional gain $K_p >> 1$ and substituting the amplitude of the set point phasor with the corresponding cavity voltage V_{sp}, the average forward power $< P_+ >$ supplied by the control loop is,

$$< P_+ > \approx \frac{V_{sp}^2 Q_{ext}}{8\frac{R}{Q}Q_L^2}\left\{\left(1 - \frac{\omega_{l,r}}{\omega_{1/2}}\right)^2 + \left(\frac{\delta\omega_{ext}}{\omega_{1/2}}\right)^2\right\}. \tag{4.50}$$

Here we have used Eq. (4.36) under the assumptions $\delta\omega_{ext}, \omega_{l,r} << K_p\omega_{1/2}$. This expression is consistent with the circuit model. (see Eq. (1.35)) Plugging in measurements of peak microphonics detuning give estimates of peak power requirements for the main linac rf systems during stable ERL operations.

4.4.3 Phasing Optimization

Besides detuning the cavity to mitigate for the reactive beam loading, optimizing the phases of the recirculating bunches can be another strategy to reduce the

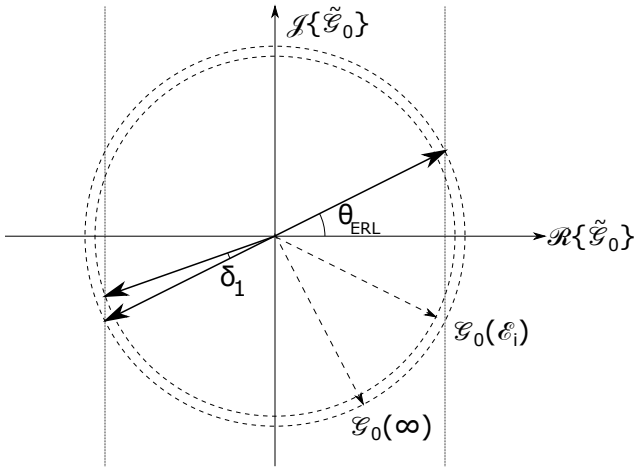

Figure 4.6: Schematic of the fundamental mode phasors induced by the recirculating bunches in the first main linac cavity in an ideal phasing situation.

forward power requirements. The simple phasing scenario illustrated in the left panel of Fig. 4.5 can be used to analyze the emergence of reactive beam loading. Figure 4.6 shows a schematic of the induced phasors in the first cavity of a main linac in an ERL, where all bunches arrive at a phase of approximately $\theta_{\rm ERL}$ ahead of the on-crest phase (positive direction of real axis) and the deceleration phase (negative direction of real axis), except for the first pass, which arrives at an angle $\theta_{\rm ERL} - \delta_1$ to account for relativistic effects. Based on the diagram, an estimate of the net phasor induced by the passage of all the recirculating bunches for a single injected bunch is given by,

$$\begin{aligned}\sum_p [\tilde{\mathcal{G}}_0(T)]_p =& \{\mathcal{G}_0(\infty)\cos\theta_{\rm ERL} - \mathcal{G}_0(\mathcal{E}_i)\cos(\theta_{\rm ERL}-\delta_1)\} + \\ & i\{\mathcal{G}_0(\infty)\sin\theta_{\rm ERL} - \mathcal{G}_0(\mathcal{E}_i)\sin(\theta_{\rm ERL}-\delta_1)\}\,,\end{aligned} \tag{4.51}$$

where $\mathcal{G}_0(\mathcal{E}_i) = |[\tilde{\mathcal{G}}_0(T)]_1|$ is the amplitude of the induced phasor for the first bunch which arrives with a low injection energy $\mathcal{E}_i$, while $\mathcal{G}_0(\infty) \approx |[\tilde{\mathcal{G}}_0(T)]_p|$ is the induced phasor amplitude for all higher energy passes. Assuming that the steady state phasor of the accelerating field is $\mathcal{F}_0$, and the induced phasors are

$[\tilde{\mathcal{G}}_0(T)]_p$, the net energy transferred to the fundamental mode for each injected bunch is $2q\mathcal{F}_0\mathcal{R}\{\sum_p[\tilde{\mathcal{G}}_0(T)]_p\}/\omega_0^2$ which follows from Eq. (4.25). This simple approximation is valid since the energy lost by the bunches due to the loss factor is much smaller than the typical energy gained or lost due to the term linear to the phasor. For perfect energy recovery this leads to $\mathcal{R}\{\sum_p[\tilde{\mathcal{G}}_0(T)]_p\} \approx 0$, which implies,

$$\mathcal{G}_0(\infty)\cos\theta_{\mathrm{ERL}} - \mathcal{G}_0(\mathcal{E}_i)\cos(\theta_{\mathrm{ERL}} - \delta_1) = 0 \implies \cos(\theta_{\mathrm{ERL}} - \delta_1) = \sqrt{\frac{k_0(\infty)}{k_0(\mathcal{E}_i)}}\cos\theta_{\mathrm{ERL}}\,, \tag{4.52}$$

where $k_0 = \mathcal{G}_0^2/\omega_0^2$ are the loss factors of the fundamental mode for different pass energies. As an example, using the loss factor values from Fig. 4.2 and using $\theta_{\mathrm{ERL}} \approx 4.67°$, δ_1 can be estimated to be 2.05° which approximately matches the value calculated numerically as shown in the left panel of Fig. 4.5. The imaginary part of the complex angular frequency defined in Eq. (4.47) may be evaluated as,

$$\omega_{l,i} = \frac{\omega_0 I_{inj} R/Q}{V_c}\left[\sin\theta_{\mathrm{ERL}} - \sqrt{\frac{k_0(\mathcal{E}_i)}{k_0(\infty)} - \cos^2\theta_{\mathrm{ERL}}}\right], \tag{4.53}$$

where we have used Eq. (4.38), (4.51) and (4.52). Plugging in the values corresponding to the $\theta_{\mathrm{ERL}} \approx 4.67°$, we obtain $\omega_{l,i} \approx 2\pi \cdot 120$ Hz which closely matches the numerical calculation. Hence, reactive beam loading even in the situation of perfect energy recovery in multi-turn ERLs can be directly attributed to diminishing loss factors at lower beam energies.

Keeping the energy change of bunches traveling through the cavity constant, the amount of detuning required to mitigate reactive beam loading reduces with increasing V_c in the case of perfect energy recovery as shown in Eq. (4.53). The increase in V_c however inflates forward power requirements to maintain stable field and also enhances the sensitivity of particle energies to field jitter. On the

other hand, a different value of δ_1 may be calculated which doesn't necessarily lead to perfect energy recovery but does reduce the overall power requirements. Combining Eq. (4.36), (4.47) and (4.48), the forward power required to maintain stable field in the presence of steady state energy recovery with large K_p and zero detuning ($\delta\omega = 0$) is given by,

$$P_+ = \frac{V_c^2 Q_{ext}}{8\frac{R}{Q}Q_L^2}\left|1 - \frac{I_{inj}}{\omega_{1/2}\mathcal{F}_0}\sum_p [\tilde{\mathcal{G}}_0(T)]_p\right|^2. \tag{4.54}$$

Plugging in the estimate of the sum of phasors from Eq. (4.52) we get the power as a function of δ_1 given by,

$$\begin{aligned} P_+(\delta_1) = \frac{V_c^2 Q_{ext}}{8\frac{R}{Q}Q_L^2}\Bigg[&\left\{1 - \mathcal{L}\cos\theta_{\text{ERL}} + \mathcal{L}\sqrt{\frac{k_0(\mathcal{E}_i)}{k_0(\infty)}}\cos(\theta_{\text{ERL}} - \delta_1)\right\}^2 + \\ &\left\{\mathcal{L}\sin\theta_{\text{ERL}} - \mathcal{L}\sqrt{\frac{k_0(\mathcal{E}_i)}{k_0(\infty)}}\sin(\theta_{\text{ERL}} - \delta_1)\right\}^2\Bigg] \\ = \frac{V_c^2 Q_{ext}}{8\frac{R}{Q}Q_L^2}\Bigg[&1 + \mathcal{L}^2 - 2\mathcal{L}\cos\theta_{\text{ERL}} + \frac{k_0(\mathcal{E}_i)}{k_0(\infty)}\mathcal{L}^2 + \\ &2\sqrt{\frac{k_0(\mathcal{E}_i)}{k_0(\infty)}}\{\mathcal{L}\cos(\theta_{\text{ERL}} - \delta_1) - \mathcal{L}^2\cos\delta_1\}\Bigg], \end{aligned} \tag{4.55}$$

where we have defined $\mathcal{L} \equiv 2Q_L I_{inj} R/Q/V_c$. In the presence of large injection beam current, the minimum forward power is achieved for $\delta_1 \approx \sin\theta_{\text{ERL}}/\mathcal{L}$. As an example, in the ideal phasing situation with $\theta_{\text{ERL}} \approx 4.67°$ and $I_{inj} = 40$ mA, whereas $\delta_1 = 2.05°$ gives perfect energy recovery with large reactive beam loading represented by $\omega_{l,i} \approx 2\pi \cdot 120$ Hz, $\delta_1 = 0.015°$ leads to a total forward rf power requirement of 18.2 W in the absence of microphonics detuning which is much smaller than the 195 W required in the absence of any beam current. This remarkable decrease in power requirement for the first cavity in the main linac arises from the optimal phasing which *reduces* the energy gain $\Delta\mathcal{E}_1$ of the bunch in the first pass to,

$$\Delta\mathcal{E}_1 = \Delta\mathcal{E}_{\text{ERL}}\sqrt{\frac{k_0(\mathcal{E}_i)}{k_0(\infty)}}, \tag{4.56}$$

where $\Delta\mathcal{E}_{\mathrm{ERL}}$ is the nominal energy change in all other passes. In the same way, the optimal phasing of the last cavity of the main linac will ensure a slightly lower energy loss in the last pass compared to the energy change in the other passes, which in contrast leads to an *increase* in rf power requirement when compared to the zero current situation. As an example, in an ideal phasing situation with $\theta_{\mathrm{ERL}} \approx 4.67°$, the last cavity in the main linac of CBETA will consume 565.8 W for $I_{inj} = 40$ mA. Hence the optimal phasing situation which requires no cavity detuning requires a slightly less energy gain/loss in the lowest energy pass compared to the other passes and hence a corresponding increase in injection energy and final beam energy at the beam stop. In general, an optimization which minimizes P_+ given by Eq. (4.54) for all cavities instead of average fundamental mode beam loading can lead to ERL settings which don't require mechanical detuning to mitigate reactive beam loading.

4.4.4 Special Bunch Patterns

ERL operation may require special bunch patterns for specific operational modes or applications where not all linac buckets contain a bunch and may consist of large gaps between the accelerating and the decelerating bunches. Panel (a) of Fig. 4.7 shows a typical regular bunch pattern used for general operations. It is characterized by three time-scales, the time between consecutive bunches T_{b}, the total length of a single continuous bunch train T_{train}, and time period after which the pattern repeats T_{rep}. The time between consecutive bunches is determined by the laser frequency of the photo-injector used in the ERL. This can be set to $T_b = N/f_0$ to fill all accelerating and decelerating buckets of the main linac, where N is the total number of times a bunch passes through the main linac

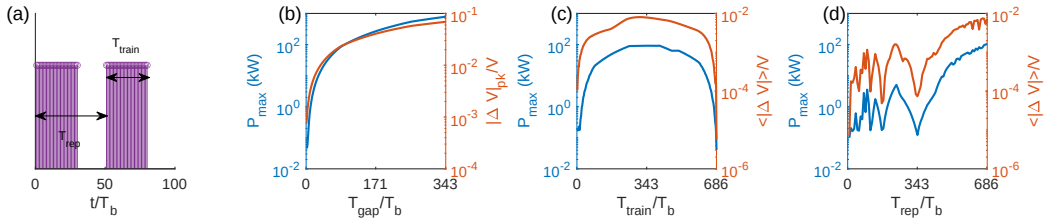

Figure 4.7: Influence of bunch pattern on field stability and power requirements of the first main linac cavity in CBETA assuming no microphonics detuning. (a) Typical bunch pattern. Peak power and field amplitude fluctuations as functions of (b) train gap T_{gap}, (c) train length T_{train} and (d) repetition time T_{rep}.

and f_0 is the operating frequency. While the average mode phasor and steady state power requirements given by Eq. (4.49) and (4.50) respectively are valid for regular bunch patterns with little gap, in general we need to solve Eq. (4.33) numerically to fully compute transients in an arbitrary situation.

We use CBETA as our model ERL to demonstrate the influence of bunch patterns on field stability and power requirements. A bunch in CBETA, passes through the main linac 8 times, while each re-circulation pass takes 343 rf periods. At the highest energy, the path length is offset by 2.5 rf periods to move the bunches into decelerating buckets. The design laser frequency ($1/T_{\text{b}}$) is 325 MHz which ensures that all buckets of the main linac can be filled without overlap at the full design current of 40 mA. Using the design lattice parameters and the induced phasors for the first cavity in the main linac shown in the right panel of Fig. 4.5, the average power requirement (Eq. (4.50)) at full current is 40.4 W assuming that the cavity is detuned by 158 Hz to compensate for reactive beam loading and there is no additional microphonics detuning. At zero current the average power required is 170.4 W, which is higher than in the presence of full current since this cavity is phased to recover more energy than it

transfers into the beam. We solve Eq. (4.33) numerically for the first main linac cavity in CBETA to evaluate the power requirements and field stability under various bunch patterns.

Gaps in otherwise full-current operation may be used to inject diagnostic (pilot) bunches in various applications. Panel (b) in Fig. 4.7 shows the peak amplitude of the voltage transient with respect to the set point and the associated peak power requirement ($K_p = 1000$) as a function of gap illustrating that such gaps can cause large voltage fluctuations leading to beam loss. Consequently, the ERL should be operated in dedicated low current modes for diagnostic purposes rather than using pilot bunches.

The average current in an ERL can be controlled by varying T_{train} and T_{rep}. Panel (c) of Fig. 4.7 represents a situation when the repetition rate is kept constant with $T_{\text{rep}} = 686T_{\text{b}}$ and the number of bunches in the train varies from 0 to 686. At both limits, the maximum power requirement matches the average estimates from Eq. (4.50). In between, the mean amplitude of the voltage transients steadily increase with the number of bunches since the accelerating and the decelerating bunches are spaced apart. Above a duty cycle of 50%, the decelerating bunches come often enough to start cancelling out the transients from the accelerating ones, which leads to a subsequent decrease in field transients and peak power requirements. This also suggests that peak power is not only a function of beam current but also T_{rep}. Panel (d) shows peak power and field stability as a function of T_{rep} for a fixed beam current of 20 mA corresponding to a 50% duty cycle. The time required for a bunch to travel through each re-circulation

pass creates a non-trivial dependence on the repetition rate with multiple values where the transients reach a minimum. This result demonstrates the need to optimize bunch patterns in order to reduce the field transients and peak power requirements for a given operational mode of the ERL. The optimization of fill patterns in a high energy 6-turn ERL is extensively investigated in Setiniyaz et al. [2020].

4.4.5 Beam Current Ramps

When an ERL starts up, there exists a finite time period when the linac has to provide more energy than it recovers. Ramping the beam current constrains the number of additional bunches injected into the ERL per unit time, thus reducing the rf forward power required to damp the transients resulting from this process. The injected beam current can be ramped in two ways, either by gradually increasing the train length of the bunch pattern or by changing the bunch charge while keeping the pattern constant. Due to various optics and beam dynamics effects related to changing bunch charge, we only explore ramping by increasing train length in this discussion. In the slow ramping regime where the time between the injection of each additional bunch is more than time the beam takes to traverse the whole ERL, the maximum change in the accelerating mode phasor is determined by the net phasor induced by the accelerating bunches i.e. $\mathcal{F}_0^{pk} \approx < \mathcal{F}_0 > + q \sum_{p=\{1..N/2\}} [\tilde{\mathcal{G}}_0(T)]_p$. Assuming that the reactive beam loading is compensated by gradually detuning the cavity during the ramp, we can calculate the peak power requirement by plugging in the peak phasor into Eq. (4.36).

Scaling the phasor to voltage units according to Eq. (4.38), we obtain,

$$P_{+}^{pk} \approx < P_{+} > -\frac{K_p Q_{ext} V_{sp}}{4R/QQ_L^2} \sum_{p=\{1..N/2\}} \mathcal{R}\{\chi_p\}\,, \tag{4.57}$$

where the average power $< P_{+} >$ given by Eq. (4.50) depends on the average beam current at the time when the new bunch is introduced. Hence each additional injected bunch generates a transient which is suppressed by the control system by injecting a peak power proportional to the loop gain K_p.

Figure 4.8 illustrates the dynamics of the mode phasor and the time dependence of forward power in the first main linac cavity of CBETA during a current ramp from 0 mA to 40 mA in 10 ms. The numerical solution assumes perfect compensation of reactive beam loading applied using a fast resonance tuner. The first panel shows a 2D histogram quantifying the time spent by the mode phasor at different positions away from the set point denoted by the origin. Such a plot can be used to gauge the likelihood of beam loss due to field transients during the ramp process by informing tracking calculations. On the other hand, the right panel shows the power drawn by the control system during the entire ramp process, clearly illustrating the effect of transients. In this particular case, the cavity is phased to recover more energy than it transfers to the beam, hence the maximum peak power is drawn right at the beginning of the ramp and is approximately 294.4 W which is close to the estimate of 264.4 W from Eq. (4.57). This is a relatively modest power requirement when compared to microphonics related transients. Consequently, the ramp rate will likely be limited by how fast a resonance tuner can detune the cavity to compensate for the increasing reactive beam loading generated during the ramp unless an optimum phasing solution is chosen which dramatically reduces reactive beam

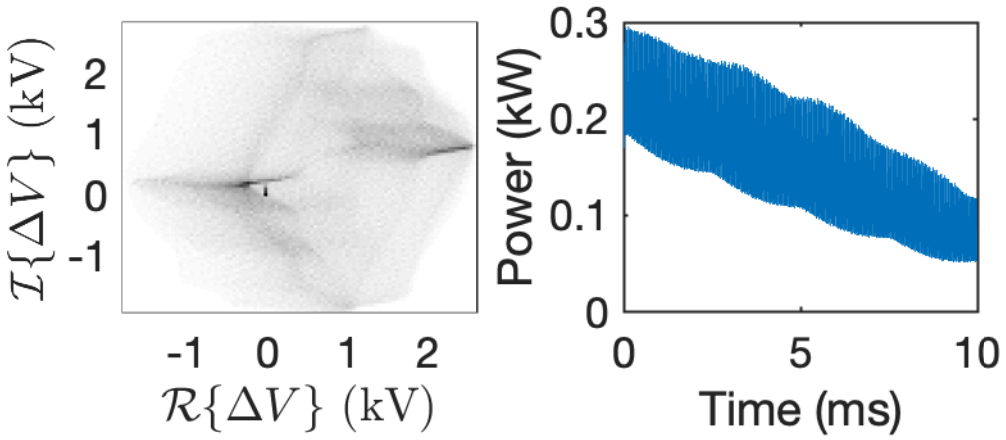

Figure 4.8: Dynamics of the accelerating mode phasor and time dependence of power in the first main linac cavity of CBETA while ramping the injector current from 0 mA to 40 mA within 10 ms. The left panel shows a 2D histogram illustrating the time spent (darker means more time) by the mode phasor at various positions in the complex plane, where the origin designates the set point of the control loop.

loading.

4.4.6 Beam Loss

In the event of catastrophic beam loss, a large portion of the stored beam may deposit all its energy into the cavities of the main linac in the absence of low energy beam to be accelerated. In the worst case, all the stored beam in the $N/2$ re-circulation arcs can travel through the main linac $N/2$ times, where N is the total number of passes through the main linac. The total charge stored in a single re-circulation arc is $I_{inj}T_p$, where I_{inj} is the injection beam current and T_p is the time required for a bunch to travel through a single pass. Assuming that the

stored energy in the cavity doesn't change much during this process i.e. V_c is almost constant, the maximum energy deposited is $\delta U = N^2 I V_c T_p/4$, where qV_c is the energy transferred from a single bunch of charge q. This additional energy deposited into the accelerating mode of the cavity could lead to a maximum increase in voltage δV_c^{max} given by,

$$\delta V_c^{max} = \frac{\pi N^2}{2}\frac{R}{Q} I h\,, \tag{4.58}$$

where we have used the definition $R/Q \equiv V_c^2/(2\omega_0 U_0)$ and substituted $\omega_0 T_p = 2\pi h$, where h is the harmonic number for re-circulation loop. If the increase in gradient is large enough to quench the SRF cavity, then the ERL should incorporate fast kickers to loose the beam in the highest energy pass, so that the energy of the residual beam can not be recovered. It is important to note that this estimate does not include any additional beam injected into the ERL before the Machine Protection System (MPS) deactivates the injector and it is crucial to keep this response time small.

A simulation of the fundamental mode voltage in the first cavity of the main linac in CBETA assuming a $1\,\mu$s response time of the MPS, for various scenarios of beam loss is shown in Fig. 4.9. The scenarios considered are loss in the injection line (equivalent to turning off the injector) and loss in the beginning of the various energy loops. In the case of loss in the injection line and the first pass, more energy is deposited into the cavity than transferred back into the beam which leads to a sudden positive jump in the voltage, while the opposite holds true for the other cases. The jump in the case of loss in the injection line is ≈ 0.53 MV which agrees with the estimate from Eq. (4.58). Since the maximum field reached is much smaller than the quench field of the SRF cavities, fast kickers are not required for high-current operation in CBETA. The simulation

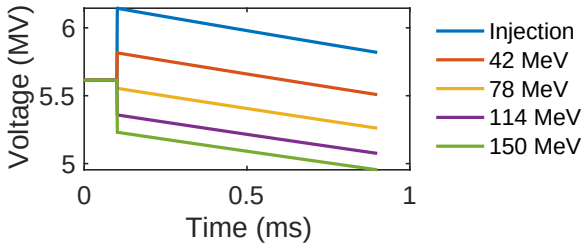

Figure 4.9: Cavity voltage transient as a function of time for various beam loss scenarios.

assumes that the induced phasors calculated using Eq. (4.21) stay constant for a brief period after the loss event. While this assumption is valid in the regime where the cavity voltage, time of arrival and energy of the bunches stay almost constant, a full simulation considering time of flight and R_{56} is required for large machines capable of storing more beam.

CHAPTER 5

DYNAMIC TEMPERATURE MAPPING

The rf to beam multiplication factor (Eq. (1.36)) which is the ratio of beam power in an ERL to the amount of rf power used in all the accelerating cavities is dependent among other things on heat dissipation of the cavity surface. The onset of local heating on top of the nominal Ohmic dissipation in SRF cavities constrains efficiency and the maximum accelerating gradients which can be reached during operations. Dynamic temperature mapping is a tool for diagnosing the various mechanisms of local heating which appear on SRF cavities. This chapter reports on the design and operation of a new data acquisition system which can enable the creation of heat maps of the cavity's outer surface at up to 50 ksps. We discuss the various sources of uncertainty in the system and illustrate an example observation of processing of field emission in a Niobium-Tin cavity.

5.1 Introduction

Thermal dissipation on the surface of SRF cavities is an essential indicator of performance which determines the amount of refrigeration capacity required for a linac. During normal operation, heat dissipated per unit area on the cavity surface is given by $R_s|H|^2/2$, where R_s is the *surface resistance* and $|H|$ is the amplitude of the surface magnetic field. The heat dissipated has to be transported away to keep the cavity at the operating temperature. However, when SRF cavities are cooled by liquid Helium, there is a finite interfacial thermal resistance (*Kapitza resistance*) at the interface between the cavity outer surface and the Helium bath, which leads to small increases in surface temperature during

operation.[Boucheffa et al., 1994, Amrit and Antoine, 2010] Temperature mapping entails spatially resolved measurements of temperature increases on the outer surface of the cavity.[Padamsee et al., 2008] This technique has been used throughout the years to diagnose non-uniformity of the cavity surface, appearance of field emission[Knobloch, 1999], multipacting and other phenomenon which causes local heating or thermal breakdown.[Antipov et al., 2013] Since the maximum accelerating gradient which can be sustained in a SRF cavity is often limited by thermal breakdown or *quenching* brought about by local heating, temperature mapping has become an important tool to understand these mechanisms.

Niobium-Tin (Nb_3Sn) which exhibits lower surface resistance and higher superheating fields when compared to Niobium[Liarte et al., 2017] is an excellent candidate to be studied using a thermometry system. Experimental studies of Nb_3Sn have revealed quench fields much lower than the theoretical superheating fields.[Posen and Hall, 2017] This observation can be explained by the onset of local heating due to the penetration of magnetic vortices[Liarte et al., 2018, Carlson et al., 2020], which eventually leads to thermal breakdown. Evidence of quantized vortex entry obtained from dynamic temperature measurements is consistent with this hypothesis.[Hall et al., 2018] Time-resolved temperature measurements over the entire cavity outer surface can thus image local heating, thermal breakdown and allow us to quantify the power dissipation arising out of magnetic vortex entry. This makes dynamic thermometry an important tool in characterizing Nb_3Sn cavities.

Temperature, spatial and temporal resolution are the primary design parameters of a dynamic temperature mapping system. The temperature resolution

limits the minimum local heat flux which can be observed on the surface. The temporal resolution limits our view of quench propagation and contributes to the measurement uncertainty of the field threshold which triggers vortex entry. There is however a trade-off between temperature and temporal resolution since more averaging (lower sampling frequency) improves the statistical uncertainty of a temperature measurement. Finally, the spatial resolution restricts our ability to point to the exact location of vortex entry which limits microscopy studies of the surface. While the enhancement of spatial resolution requires a redesign of the temperature sensing elements themselves, improvement of the acquisition system can help us achieve better time and temperature resolutions.

Existing thermometry systems are limited in their ability to obtain time-dependent information from a large number of temperature sensors simultaneously. This constraint arises from the design of the data acquisition systems which are based on multiplexing.[Antipov et al., 2013, Knobloch, 1997] In such a system, a single Analog to Digital Converter (ADC) channel is used to digitize data for a number of temperature probes. This effectively reduces the sample rate of the data to f_s/N, where f_s is the sample rate of the ADC and N is the number of thermometer channels to one ADC channel. Multiplexing further staggers the acquisition time window of each channel, which can be a significant constraint when observing dynamics happening at time scales comparable to the effective sample rate.[1] Hence acquisition systems with a large number of channels each sampled by separate ADCs is essential in improving resolution and avoiding artifacts due to different acquisition windows.[Schmitz et al., 2018]

In this chapter we report on a new dynamic thermometry system capable of

[1] This is similar to the rolling shutter effect in video cameras.

sampling 768 channels at a rate of 50 ksps. The next section describes the instrumentation, including the thermometer setup and the new acquisition system. Section 5.3 details the analysis of the temperature data and the various sources of uncertainties. The procedure for estimating thermal flux and the associated uncertainties is presented in Sec. 5.4. Finally, Sec. 5.5 gives some example data obtained on a Nb_3Sn cavity using this system.

5.2 Instrumentation

The temperature mapping (T-map) system is used in concert with a complete vertical test setup in order to obtain both rf and thermal information simultaneously during a test. The thermometry system consists of many thermometers attached to the outer surface of a cavity and an associated acquisition system to record all the data. The new system presented here uses the original temperature sensing elements designed at Cornell for use with a single cell 1.3 GHz TESLA cavity, but uses a new acquisition system.

5.2.1 Temperature Sensors

The temperature sensors are arranged in a fixed grid covering the entire outer surface of the cavity. The sensors are distributed among 38 thermometer boards spanning the entire azimuth of the cavity with each board holding 17 sensors as shown in panels (a) and (b) of Fig 5.1. This arrangement ensures a spacing of $\sim$ 1 cm between each sensor which is the spatial resolution of the system. The density of packing is limited not only by the space required to securely

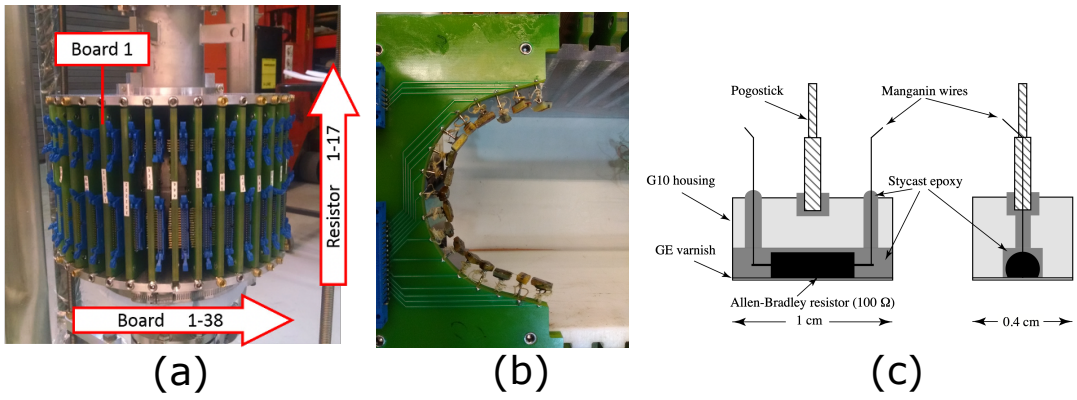

Figure 5.1: Major components of the thermometry system. (a) The arrangement of 38 resistor boards around a 1.3 GHz single cell. (b) A single resistor board. (c) Schematic for a single temperature sensor. Reproduced from Knobloch [1997].

mount each sensor on to the cavity surface but also due to thermal dissipation concerns. The sensors are designed to stay in good thermal contact with the cavity, thereby isolating a fraction of the cavity surface from the Helium bath and redirecting the thermal flux. As more sensors are used to cover the outer surface of the cavity, the equilibrium temperature on the surface will tend to be higher and thus affect the measurement itself. This imposes a limit on the minimum thermometer spacing achievable. A few additional sensors immersed in the bath isolated from the surface of the cavity are used as bath temperature sensors which can be used to account for Helium temperature drifts or other global effects. A complete description of the system and the design considerations can be found in Knobloch [1997].

The temperature sensors are carbon resistors from Allen-Bradley with a nominal resistance of 100 Ω (5 %, 1/8 W) at room temperature. These resistors consist of powdered carbon (graphite) mixed with an insulator and binder material to achieve the desired resistance. Graphite is a semi-metal, while the powdered form acts as a very small band gap (~ 0.1 meV) semiconductor resulting in an

exponential dependence of resistance on temperature, which forms the basis of the measurement system. The resistance R of a sensing element as a function of temperature T is given by,

$$R(T) = R_\infty e^{\frac{\mathcal{E}_g}{k_B T}}, \tag{5.1}$$

where R_∞ is the resistance at high temperatures, $\mathcal{E}_g$ is the band gap of the material and k_B is the Boltzmann constant. However this simple equation is unable to fully characterize the resistance of the sensor material and a modified regression model is generally used in practice for calibration purposes.[Rudtsch and von Rohden, 2015, Steinhart and Hart, 1968] The resistors as manufactured are not suitable for direct use for thermometry and they are specially mounted and prepared for best thermal characteristics.

Panel (c) of Fig. 5.1 shows the construction of a single temperature sensor with the resistor as the active component. The design is optimized to increase the thermal contact of the resistor while reducing heat dissipated into the bath. A G-10 housing along with epoxy potting compound encases the resistor providing a thermal insulating barrier so that the resistor is not cooled directly by the bath. The insulating case of the resistor as manufactured, is ground away to expose the graphite inside, and a thermal grease is used to increase contact of the graphite with the cavity surface. The elements are attached to the thermometer boards using spring loaded sticks, which further ensure good contact. Even with these measures, the temperature rise detected by a sensor is a fraction of the actual rise of temperature on the cavity surface. Each of the 646 resistors in contact with the cavity are connected separately to the acquisition system which sits outside the cryostat.

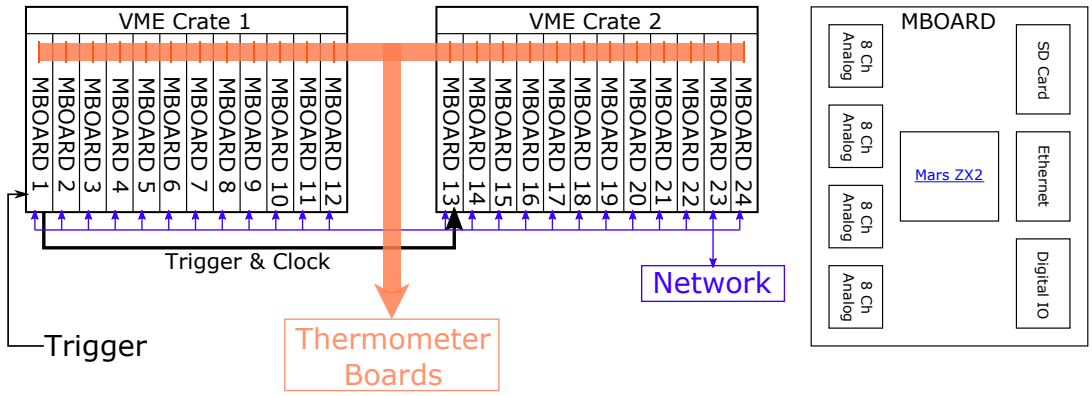

Figure 5.2: Data acquisition architecture for the thermometry boards.

5.2.2 Acquisition System

The acquisition system connects to each resistor separately, providing a bias current and measuring the potential difference across them. To simplify the design of the data acquisition system, the 768 channels are divided into 24 identical modules called MBOARDs each capable of acquiring signals from 32 resistors. A schematic of the T-map acquisition system is shown in Fig. 5.2. The 24 MBOARDs are arranged in two VME crates each with a custom designed backplane for inter-board communication. Further each MBOARD contains four identical analog acquisition boards which acquire data from 8 channels each. Signal processing, data acquisition and storage is controlled by a Mars ZX2 SoC module[Enclustra FPGA Solutions] on each board. These devices run an embedded Linux operating system and connect to the lab network via Ethernet allowing them to be administered by a separate client application which initiates and monitors the acquisition process. Each crate has one MBOARD designated as the crate *leader* which synchronizes all other boards designated as *followers* and provides a trigger signal to initiate acquisition. MBOARD 1 acts as the leader board of the whole system receiving a hardware trigger and distributing

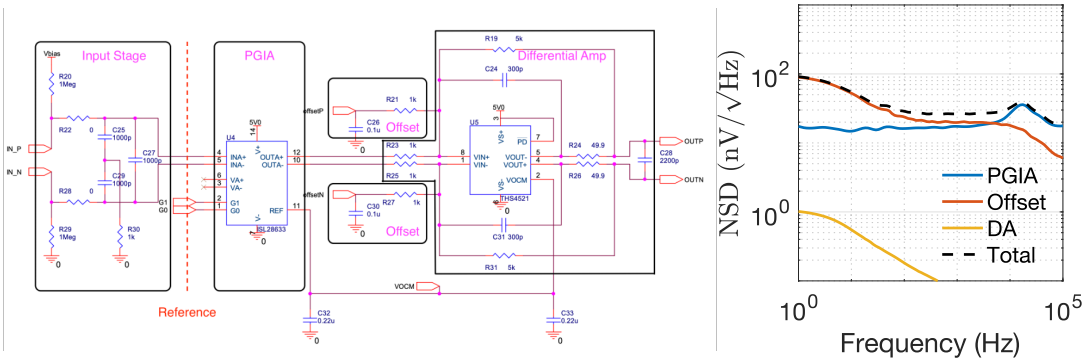

Figure 5.3: Analog front end circuit and noise estimation. The left panel shows a simplified circuit with the major components annotated and the right panel shows noise spectral density as a function of frequency as estimated from the circuit.

the clock and trigger signals to MBOARD 13. The analog boards themselves are designed to be configurable by the user to adjust gains and offsets in order to maximize the dynamic range of the measurement.

Both terminals of the temperature sensing resistors connect to twisted pair cables which travel from the thermometry boards to identical analog circuits shown in the left panel of Fig. 5.3. The circuit amplifies the signal in two stages, first by a Programmable Gain Instrumentation Amplifier (PGIA) which can be configured by the user. A programmable offset is applied to the differential output of this stage to adjust the range of the amplified signals. Then a fixed gain (gain = -5) differential amplifier sends the signal into the ADC. While the noise contributed by the 24-bit ADC is negligible compared to the detected signal, the thermal noise from the resistor, the noise from the amplification stages and the offset is a significant source of statistical uncertainty in the temperature measurement. The right panel of Fig. 5.3 shows the contributions of the different components of the analog circuit and the net noise spectral density of the signal fed to the ADC. Noise spectral density n is defined as the square root of the

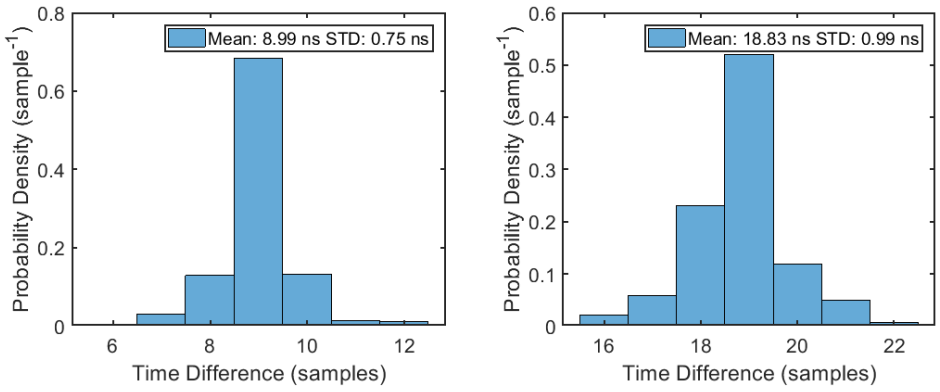

Figure 5.4: Clock jitter on the acquisition boards. Left panel shows histogram of time difference between rising edge of the clock signals on MBOARDs 1 (leader) and 13 (crate 2 leader). Right panel shows the histogram of time difference between MBOARDs 1 and 14 (crate 2 follower).

differential power of the signal per unit bandwidth i.e. $n(f) \equiv \sqrt{\mathrm{d}P/\mathrm{d}f}$, where P is the power contained in the signal measured in nV^2 and f is the frequency in Hz. The total noise as a function of frequency shows a hump at high frequencies, which is the primary source of temperature uncertainty at short acquisition time scales. In addition to amplification, the signals also undergo some low pass filtering before it is digitized by the 24-bit ADC, in order to avoid sampling artifacts.

The sampling time window (aperture) of all the thermometer channels must be aligned with each other to ensure minimum temporal uncertainty of the measured dynamic temperature maps. Synchronization of all the ADCs in the acquisition system is done in two stages. First, all the ADCs receive an universal clock signal generated by the leader board (MBOARD 1), which is distributed via the backplane in crate 1 and through a coaxial cable to crate 2. Second, the acquisition time windows of all the ADCs are aligned using a special aperture trigger, which induces the ADCs to start sampling the signals at the same time. A measurement of sampling time jitter and offset is shown in Fig. 5.4 indicating

a jitter of about 1 ns and maximum offset of 20 ns between the sampling apertures. While the jitter is less than 1 ns on all boards the offset depends on the distance the clock and trigger signals have to travel before they reach the ADCs. However, the time differences involved are still a lot smaller compared to the minimum sample time of 20 μs for the T-map system. In effect, the timing jitter and offset between the different sensor channels is negligible when compared to the time resolution of the acquisition system. The timing of the data is also an essential factor in the software design for the system.

The software and firmware architecture employed by the T-map acquisition system is divided into three layers and is optimized for high volume data flow. Programmable Logic (PL) in the form of a Field Programmable Gate Array (FPGA) is used for deterministic control of the ADCs in order to acquire the signals at the requested sample rate and store it into a fast Block RAM (BRAM) buffer. However, this small buffer which can only store data equivalent to a fraction of a second is continuously overwritten. The next level of firmware running on the Programmable System (PS) in turn copies the data into a much larger DDR3 RAM. It is crucial that the data saved to the limited BRAM be copied over to the large DDR3 RAM at least as fast as the data is created. The maximum memory speed thus imposes an upper limit to the sample rate of the system. In the current design, the maximum sample rate of 50 ksps allowed by the ADCs on all 32 channels on each board leave the PS with plenty of speed overhead. During the acquisition, all the raw voltage data is stored in the DDR3 RAM, which constrains the maximum duration of the acquisition to $\approx$ 60 seconds. Once the acquisition is complete, all the data is written to a remote disk on the laboratory network for permanent storage. This whole process is administered remotely by a client application which is the third level of software for

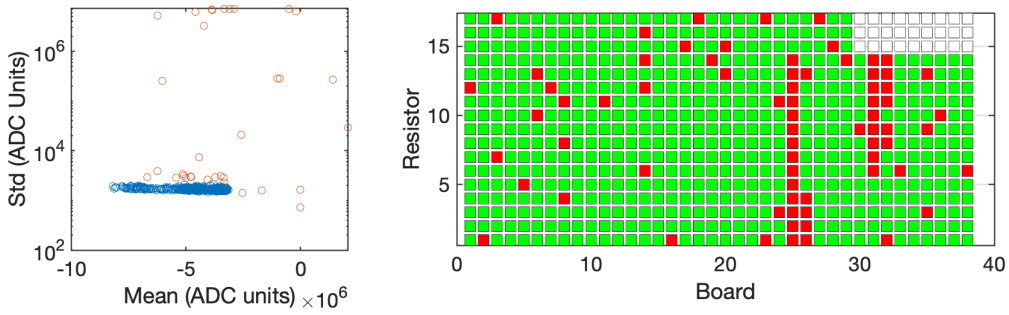

Figure 5.5: Channel selection from raw data taken at 2 K. The left panel shows the standard deviation v/s the mean for each channel with selected and discarded points colored blue and red respectively. The right panel shows the distribution of the selected (green) and discarded points (orange) on the surface of the cavity, while white squares represent disconnected channels.

the T-map acquisition system.

5.3 Temperature Analysis

The first step towards analyzing a dynamic temperature map is to determine which channels are functioning properly and discard the faulty data. One method of selecting the functioning channels is to visualize the statistics of the raw data when there is no heating on the cavity surface, i.e rf is turned off. In this case, most temperature sensors should report similar mean voltage and noise levels, since the temperature of the cavity and the bath is uniform in the absence of significant additional thermal flux. Resistors with damaged thermal or electrical contact or which are connected to acquisition channels with faulty analog processing circuits are going to be outliers. Figure 5.5 shows the statistics of a raw rf off data set at 2 K. The left panel shows a scatter plot of the standard deviation as a function of mean for all the acquisition channels. There is clearly a

dominant cluster of points (colored blue), which represents channels which are working properly, while the others have been discarded. The right panel shows the distribution of discarded points revealing that their positions are mostly random. The number of discarded channels during typical experiments have been around 10 % of the total number of channels. The selected channels are then calibrated for use in temperature maps.

5.3.1 Calibration and Repeatability

The resistance of the thermometers are calibrated against precision Cernox^{TM} sensors also placed on the outer surface of the cavity. The calibration process starts when the cavity is immersed in liquid Helium ($\sim$ 4.2 K), and the whole thermal mass has equilibrated to the temperature of the bath. After this, the vapor pressure of Helium is progressively lowered which in turn slowly cools down the bath while keeping approximate thermal equilibrium in the system. During this process, multiple temperature maps are acquired along with the corresponding temperature from the calibrated precision sensors. This process generates calibration data i.e voltage v/s temperature for each channel. The bias network in the input stage of the analog circuit (Fig. 5.3) generates a constant current flowing through the resistor. Using Eq. (5.1) to describe the resistance and an arbitrary voltage offset V_0 in the electronics, the measured voltage is given by,

$$V = V_0 - V_\infty e^{\frac{g}{T}} , \tag{5.2}$$

where we have defined $g \equiv \mathcal{E}_g/k_B$ and V_∞ corresponds to the potential difference across the resistor in the high temperature limit. The calibration data from a single thermometer channel along with the best fit to Eq. (5.2) is shown in

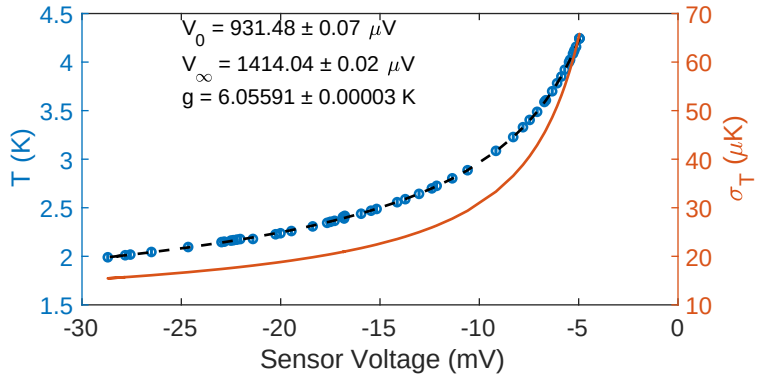

Figure 5.6: Temperature as a function of voltage for a single thermometer channel. The blue circles with error bars (very small since the data is averaged over 1 second) represent measured calibration data, while the black dashed line is the best fit with parameters shown in the plot. The orange line shows the systematic uncertainty of temperature measurement.

Fig. 5.6.

The statistical uncertainty of the potential difference measured across the resistors leads to an uncertainty in model parameter estimation. For example the total uncertainty in g is given by $\sigma_g = \sqrt{\sum_i \sigma_{V,i}^2 (\partial g/\partial V_i)^2}$, where V_i and $\sigma_{V,i}$ are the mean voltage and the uncertainty of the mean respectively for the calibration point i. $\partial g/\partial V_i$ is calculated as the differential change of the fit parameter g for an infinitesimal change of only one observation point V_i while keeping all other points the same. The estimates of uncertainty in the fit parameters improve with more observation points during calibration. This is crucial since the uncertainty in fit parameters σ_{V_0}, σ_{V_∞} and σ_g introduce a systematic uncertainty in the measurement of temperature, σ_T^{syst} given by,

$$\sigma_T^{\text{syst}} = \sqrt{\left(\sigma_g \frac{\partial T}{\partial g}\right)^2 + \left(\sigma_{V_0} \frac{\partial T}{\partial V_0}\right)^2 + \left(\sigma_{V_\infty} \frac{\partial T}{\partial V_\infty}\right)^2} = \frac{T}{g}\sqrt{\sigma_g^2 + T^2\left\{\left(\frac{\sigma_{V_0}}{V_0 - V}\right)^2 + \left(\frac{\sigma_{V_\infty}}{V_\infty}\right)^2\right\}}, \tag{5.3}$$

where we have neglected any correlations in error estimates of the fit parame-

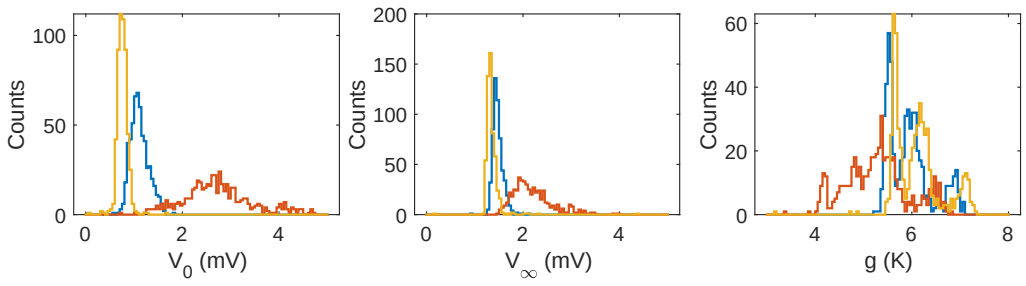

Figure 5.7: Histograms of calibration fit parameters V_0, V_∞ and g for three successive cool downs of the same cavity shown in blue, orange and yellow respectively.

ters. The orange line in Fig. 5.6 shows σ_T^{syst} as a function of the observed voltage. For the channel shown, an uncertainty of 15 μK is expected near 2 K while a much greater uncertainty of 65 μK is predicted near 4.2 K. The uncertainty of temperature measurement is greater at higher temperatures since the resistance changes less at higher temperature.

Each resistor of the thermometry device must be calibrated each time the system is cooled down. This is because each sensor has a slightly different resistance and temperature dependence. Further, it has been observed that individual resistors change after each thermal cycle. Figure 5.7 illustrates the overall statistics of the fit parameters of all the sensor channels showing change after each thermal cycle. Due to disruptions during cool-down, the cavity and the thermometry system were not in thermal equilibrium for the data shown in orange leading to wider distribution of estimated calibration parameters. While the statistical distribution of V_0 and V_∞ are close to Gaussian in all the cases, the statistics of g is not. While the statistical distribution of g shows multiple peaks, their spatial distribution on the cavity surface is random. A possible explanation for this observation is that the resistors were manufactured in different batches giving them different compositions and resulting band gaps. After calibration,

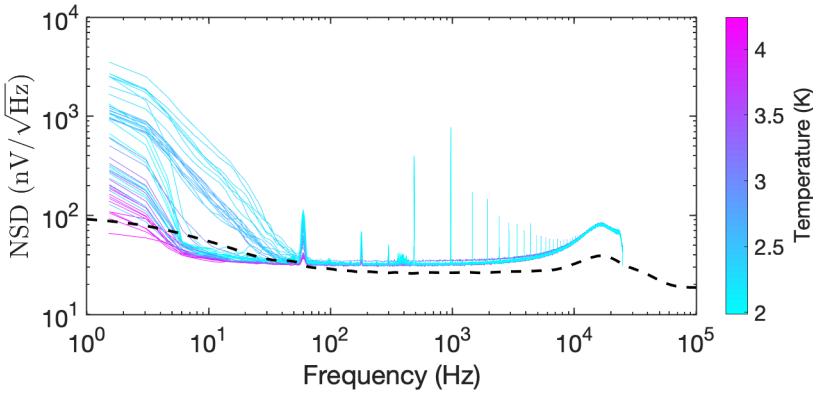

Figure 5.8: Noise spectral density of the calibration data as a function of frequency for different temperatures. The black dashed line is the estimated noise from the amplifier circuit which feeds the ADCs.

all raw data can to be converted to temperature for further analysis.

5.3.2 Noise Sources

The signals acquired from the sensors on the temperature boards are subject to noise from bath fluctuations, ambient electromagnetic radiation, electronic noise introduced by the analog circuit and noise from the ADC. In order to characterize these contributions, we calculate the noise spectral density n as a function of frequency f of the acquired signals $V(t)$ using the Welch's method.[Welch, 1967] The noise spectral density of the calibration measurements during cooldown from one experiment averaged over all working sensor channels is shown in Fig. 5.8. The noise present in these signals can be broadly classified into three categories. The High Frequency (HF) part of the noise spectrum ($\gtrsim$ 10 kHz) is consistent with the estimated noise from the analog processing circuit, which is shown as the black dashed line. The majority of the high frequency noise can be attributed to the PGIA as explained in Sec. 5.2 while the discrepancy between

the measured spectra and the theoretical calculation arises from the use of a different gain setting in experiment than the one used for estimation. The second noise contribution can be seen as discrete peaks in the spectrum at 60 Hz and its harmonics among others. The source of these peaks may be ambient electromagnetic noise, noise in the analog circuits or even vibrations in the Helium bath. The third contribution to the noise spectrum is the Low Frequency (LF) component $\lesssim 100$ Hz which shows a strong dependence on bath temperature.

The temperature dependence of low frequency noise in the T-map data suggests that it is generated by the cryogenic system. Figure 5.8 shows that the LF noise generally increases in magnitude with decreasing temperatures, even though the measurement is subject to random variations. The sources of noise in the cryogenic system may include cryogenic turbulence excited by the pumping of Helium vapor out of the test dewar and actuation of valves to control the vapor pressure of the bath. A detailed study is required to ascertain the sources. The amplitude of the 60 Hz peak also generally increases with reducing temperature, giving evidence that it is not sourced from ambient electronic noise. The electronic noise spectra may be used to calculate the statistical uncertainty of the acquired T-maps.

The statistical uncertainty in a measured T-map depends on the time scale over which the data has been averaged. For example, at a high sample rate of 50 ksps, each image acquired from the system, is subject to noise up to 25 kHz[2], which includes the substantial electronic noise generated by the PGIA. Hence, a single T-map acquired at a large sample rate is subject to a large statistical uncertainty. In contrast, if a map is obtained at 1 ksps (or equivalently decimating

[2]When a continuous signal is sampled at a frequency f_s, the Nyquist-Shannon sampling theorem restricts the bandwidth of the resulting discrete signal to $f_s/2$.

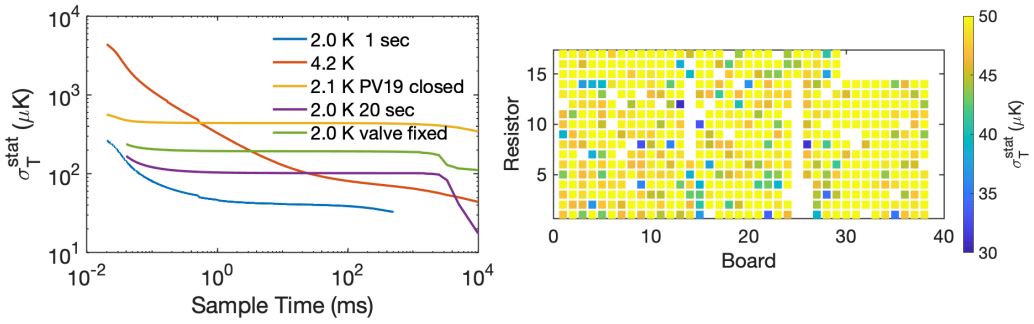

Figure 5.9: Statistical uncertainty of temperature measurement. Left panel shows σ_T^{stat} as a function of sample time for various experimental conditions, while the right plot shows the distribution of σ_T^{stat} for a 1 milli-second measurement corresponding to the blue line in the left panel.

the 50 ksps data by a factor of 50), all the high frequency noise is averaged out resulting in a much lower statistical uncertainty. We can quantify this effect by integrating the power spectrum with frequency. The one-sided discrete power spectral density $p_T(f_k)$ of a temperature sequence $T(t_j)$ of length N and sample rate $f_s \equiv 1/\Delta t$ is defined as,

$$p_T(f_k) \equiv \frac{2}{\Delta f}\left|\frac{1}{N}\sum_{j=0}^{N-1} T(t_j) e^{\frac{-2\pi k i}{N}}\right|^2 \tag{5.4}$$

where $t_j = j\Delta t$, $\Delta f = f_s/N$, $f_k = k\Delta f$ and k ranges from 1 to $N/2$. The total statistical uncertainty σ_T^{stat} of a temperature signal sampled at a time scale of $0.5/f_k$ is thus given by,

$$\sigma_T^{\text{stat}}(0.5/f_k) = \sqrt{\Delta f \sum_{j=1}^{k} p_T(f_j)}\,, \tag{5.5}$$

where k ranges from 1 to $N/2$ which in the case of the present T-map system ranges to a minimum of 20 μs. This estimation of statistical uncertainty determines the optimal sample rate for taking data.

Figure 5.9 shows the variation of mean statistical uncertainty of the T-map system with sample time, different cryogenic conditions and over the surface of

the cavity. The frequency dependence of σ_T^{stat} shows large uncertainty at small time-scales, which gets averaged out at intermediate sample times of $\approx$ 1 ms. The variation with frequency stays flat before eventually dropping off after considerable averaging of $\gtrsim$ 10 sec. The uncertainty also varies with temperature and cryogenic conditions. In general 4.2 K data (red) is more noisy, since the electronic noise dominates over the small temperature signal (Fig. 5.6 shows a typical calibration curve which changes less with temperature at 4.2 K.) while at $\approx$ 2 K, the bath fluctuations dominate uncertainty up to intermediate sample rates of 1 ksps. The cryogenic system sustains temperatures below 4.2 K in the vertical test setup by maintaining the vapor pressure of Helium using a pumping system further governed by valves. The long acquisition (violet) at 2.0 K suggests that very slow bath oscillations caused by periodic actuation of a control valve dominates σ_T^{stat}. The right panel of Fig. 5.9 shows a uniform distribution of uncertainty over the cavity surface at a sample time of 1-ms under this default experimental condition. In the absence of any pumping (yellow), the slow pressure drift of the bath completely dominates the uncertainty. Further, if all valves are kept open at a static position (green), a low frequency component at a sub Hz frequency shows up in addition to the drift. These observations suggest the use of intermediate sample rates of 1 ksps (or equivalently decimating the 50 ksps data by a factor of 50) for dynamic T-maps at 2 K where speed is not important, yielding statistical uncertainties around 100 μK. While the cryogenic system plays an important role in determining σ_T^{stat}, further reduction of uncertainty is possible by compensating for drifts on the cavity sensors using the bath temperature data.

Slow drifts in the bath temperature appear as an additive component to the actual heating on the cavity surface. At temperatures below the lambda point,

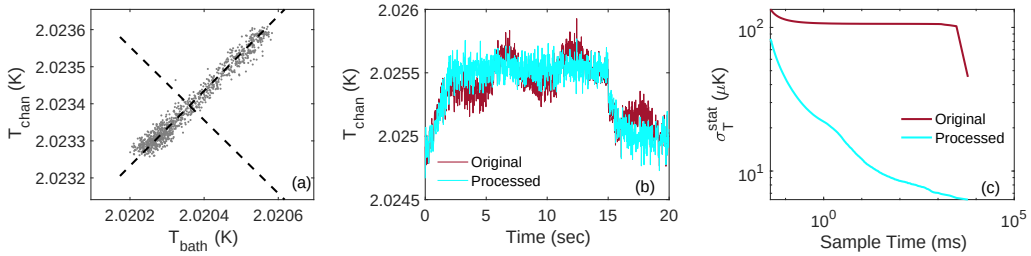

Figure 5.10: Bath subtraction as a method of reducing statistical uncertainty. (a) Principal component analysis of rf off data. (b) Rf on temperature measurement on one thermometer channel as a function of time. (c) Statistical uncertainty of the same T-map channel as a function of frequency.

thermal conductivity of the bath becomes very large, leading to an uniform temperature distribution of Helium around the sensors attached to the cavity. In principle, we can measure the Helium temperature fluctuations on separate bath sensors and directly subtract this contribution from the temperatures measured by the map, in order to isolate the heating on the cavity surface. However such a simple subtraction is not possible, since the sensors are thermally anchored to the cavity surface and are less affected by Helium temperature than a sensor suspended in the bath. Further, thermal fluctuations travel at $\approx 16\,\mathrm{m/s}$ in superfluid Helium at 2 K through second sound waves.[Wang et al., 1987] This can lead to small time differences between the fluctuations as measured by different thermometers on the cavity surface. Nevertheless, the equivalent phase lag of the sub-Hz oscillations illustrated in Fig. 5.9 as they propagate around the cavity surface will be small. As an example, the phase difference between the wave-fronts of a 1 Hz second sound wave as it propagates through a distance of 20 cm is $360 \times 0.2 \times 1/16 \approx 4.5^\circ$. As a result, subtraction of band-limited bath signals is a suitable method for reducing statistical uncertainty of the temperature map.

Elimination of bath fluctuations from the thermometer signals T_{chan} can be written as,

$$\hat{T}_{\text{chan}} = T_{\text{chan}} + \alpha F_L\{T_{\text{bath}} - \langle T_{\text{bath}} \rangle\}\,, \tag{5.6}$$

where $\hat{T}_{\text{chan}}$ is the processed data, α is a constant unique to each channel, $F_L\{\}$ is a functional which denotes low pass filtering[3] of the bath signal T_{bath} and $\langle T_{\text{bath}} \rangle$ is the mean bath temperature. A simple procedure for determining α is Principal Component Analysis (PCA)[Shlens, 2014] of the band-limited signals $F_L\{T_{\text{chan}}\}$ and $F_L\{T_{\text{bath}}\}$. This method calculates the direction vector of the bath oscillations (principal component of the signals) in the T_{chan}-T_{bath} space in the absence of additional heating on the cavity surface as shown in panel (a) of Fig. 5.10. The distribution takes the form similar to an ellipse, where each point in the plot corresponds to the values of the temperature signals at some instant. Since we have already filtered out the high-frequency components from the signals, the direction of largest standard deviation corresponds to bath oscillations, and the orthogonal direction corresponds to the actual desired data. It can be shown that the slope of the minor axis of the distribution equals to the desired α for the thermometer channel. Using this value in Eq. (5.6), we obtained the processed signal (cyan) in panel (b). Panel (c) shows σ_T^{stat} as a function of sample time for the duration of constant field in the cavity (flat portion of the processed signal). The data from this channel illustrates how this method can reduce the statistical uncertainty of temperature measurement from $\sim 100\,\mu$K to $\sim 30\,\mu$K for a sample rate of 1 ksps.

[3] It is important that the filter itself does not introduce any phase lag into the bath oscillations which makes zero-phase filtering preferable. This analysis uses the MATLAB© function `filtfilt`.[MathWorks®]

5.4 Thermal Flux Estimation

Besides the qualitative utility of T-maps to visualize local heating, they can also be used to quantify thermal flux which can be compared to theoretical models. A simple method of determining the thermal flux arises from assuming that heating on the cavity surface is mostly uniform with small departures on certain areas with characteristic length scales of more than the sensor spacing. The total power P_c^{cal} dissipated at the surface of the cavity as measured by N resistors can be approximated as,[Knobloch, 1997]

$$P_c^{\text{cal}} = \frac{1}{K_T} \sum_{i=1}^{N} \Delta T_{\text{chan},i} A_i \tag{5.7}$$

where $\Delta T_{\text{chan},i}$ and A_i are the increase in temperature and area covered by sensor i. K_T is a calibration factor which quantifies the increase in temperature of the cavity surface in response to thermal flux propagating into the Helium bath. This is related to the Kapitza resistance[Swartz and Pohl, 1989] of the Niobium/Helium interface and is assumed to be the same over all sensors. This value can be obtained by acquiring T-maps at low fields where the surface heating P_c can be estimated indirectly from Q_0 measurements. After the calibration process is complete, a temperature elevation on a sensor can be interpreted as a local thermal flux $\delta P_{c,i}^{\text{cal}}$ given by,

$$\delta P_{c,i}^{\text{cal}} = \frac{\Delta T_{\text{chan},i} A_i}{K_T} \,. \tag{5.8}$$

This estimation of thermal flux is subject to uncertainties from varying thermal contact efficiencies for each resistor and the spatial variation of the flux itself.

The efficiency of a sensor η_T is defined as the ratio of the temperature increase as seen on the sensor $\Delta T_{\text{chan},i}$ to the actual temperature increase on the surface $\Delta T_{\text{surf}}(\vec{x}_i)$, where $\vec{x}_i$ is a point on the outer surface of the cavity. The

efficiency of a thermometer is determined by the interfacial thermal resistance between the surface of the cavity and the resistor and between the resistor and the Helium bath. As explained in Sec. 5.2, the flow of heat between the Helium bath and the resistor is attenuated by encasing the resistor in thermal insulator material, with the exposed side touching the cavity surface. In addition, thermal grease is used to close gaps in the interface and allow for better heat transfer. Regardless of these measures, $\eta_T = 0.35 \pm 0.13$ has been reported in previous measurements of the thermometry system [Knobloch, 1997] which is one source of systematic uncertainty in flux measurement. The calibration data itself, along with thermal simulations of heating on the surface can serve as a method to measure η_T for individual sensors.

The spatial variation of heating on the cavity surface is yet another source of uncertainty in thermal flux measurement. In an ideal situation, heat from a point source on the rf surface diffuses into a localized distribution of flux on the Helium cavity interface. This flux distribution on the surface gives rise to elevated temperatures which can be approximated as a Gaussian given by $\Delta T(r) \approx \Delta T_0 \exp\{-r^2/(2\sigma_h^2)\}$, where ΔT_0 is the peak temperature on the surface and r is the distance from the peak. σ_h denotes the size of the distribution and is dependent on Kapitza resistance of the surface. The power emitted from the point source which also equals the total heat flux δP_c which flows through the surface into the Helium bath is given by,

$$\delta P_c = H_k \int_0^\infty \Delta T(r) 2\pi r \, \mathrm{d}r \approx 2\pi H_k \sigma_h^2 \Delta T_0 \,, \tag{5.9}$$

where H_k is the interfacial thermal conductivity between the cavity surface and the Helium bath. The heating on the cavity surface is observed on a few neighboring sensors. Assuming that the highest temperature is recorded on one sen-

sor with index m, the thermal power estimated from Eq. (5.8) is,

$$\delta P_{c,m}^{\text{cal}} = \frac{\Delta T_0 \exp\{-r^2/(2\sigma_h^2)\} A_m}{K_T} . \tag{5.10}$$

The ratio of estimated power to the real power given by $\chi \equiv \delta P_{c,m}^{\text{cal}} / \delta P_c$ is independent of the unknown quantity ΔT_0. Assuming that H_k, σ_h, K_T, A_m and η_{T_m} are known from material properties, thermal modelling and calibration data, the primary source of systematic uncertainty in the flux measurement stems from the unknown distance r of the sensor from the point source as seen on the cavity outer surface. The relative uncertainty ϵ_χ of the ratio χ is given by,

$$\epsilon_\chi \equiv \frac{\sqrt{\langle \chi^2 \rangle - \langle \chi \rangle^2}}{\langle \chi \rangle} = \sqrt{\frac{\langle \exp\{-r^2/(\sigma_h^2)\} \rangle}{\langle \exp\{-r^2/(2\sigma_h^2)\} \rangle^2} - 1} . \tag{5.11}$$

If the average distance between the resistors is l, then the position of the point source with respect to the sensor follows an uniform probability distribution between $r = 0$ and $r = l/2$. This allows us to estimate ϵ_χ as,

$$\epsilon_\chi = \sqrt{\frac{l}{2\sqrt{\pi}\sigma_h} \frac{\text{erf}(\frac{l}{2\sigma_h})}{\left\{\text{erf}(\frac{l}{2\sqrt{2}\sigma_h})\right\}^2} - 1} , \tag{5.12}$$

where $\text{erf}(x) \equiv 2/\sqrt{\pi} \int_0^x \exp(-u^2)\, \mathrm{d}u$ is the error function. With a thermometer spacing of $l \approx 1$ cm on a Nb_3Sn cavity operating at 2 K, we get $l/(2\sigma_h) \sim 1$. The spatial resolution of the T-map limits the relative uncertainty of a flux measurement to $\epsilon_\chi \approx 14\%$. This simple calculation illustrates the need for more sophisticated flux estimation methods which rely on multiple sensors and thermal models to reduce the systematic uncertainty of these measurements.

5.5 Results

The dynamic thermometry system can be used to image local heating on the surface of the cavity. Figure 5.11 shows a few snapshots from a dynamic T-map

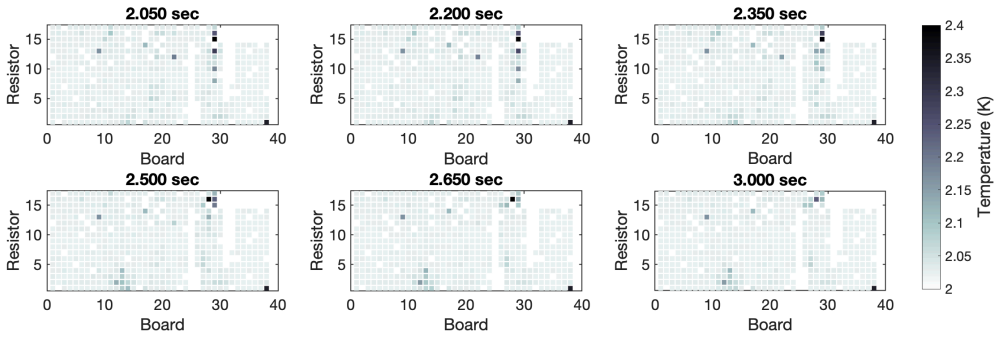

Figure 5.11: Snapshots from a dynamic T-map acquisition. All maps share the same color scale shown to the right. White squares represent discarded channels.

of a Nb_3Sn cavity acquired at 25 ksps. At $t = 2.05$ sec, a warm vertical streak can be observed on the surface of the cavity, indicating possible field emission. Over the next few snapshots, this streak disappears and a separate patch of local heating appears at the bottom of the cavity. This is the first dynamic observation of processing of a field emission event, clearly illustrating one application of this new T-map acquisition system.

CHAPTER 6

CONCLUSION

6.1 Microphonics Suppression

The operation of SRF cavities with high Q_L allows the use of efficient solid state amplifiers. However the availability of limited power presents a significant constraint on the peak microphonics detuning which can be tolerated while maintaining stable field. As a result, mitigation of vibration sources have become important for operations for a growing number of particle accelerators. Apart from passive measures, most cryomodules also incorporate fast tuners based on piezo-electric actuators which can be used for active resonance control such as in LCLS-II, XFEL and CBETA. Assuming that the mechanics is adequately described by linear partial differential equations, we can model the tuner's response as a slowly changing Linear Time Invariant system. As a result, the dynamics of the tuner can be encoded in a transfer function $\tau(\omega)$, which expresses the amplitude and phase response of the cavity resonance frequency to sinusoidal excitations applied to the actuator at different frequencies. Measurements from 7-cell SRF cavities used in the main linac of the CBETA project indicate that the bandwidth of an active control system must be limited to below microphonics frequencies of 200 Hz beyond which mechanical eigenmodes dominate the dynamics. The transfer function data is used in the design of the active microphonics control system.

The narrow band Active Noise Control(ANC) algorithm may be derived starting from the assumption that microphonics detuning can be decomposed into a finite sum of sine waves. A sine wave of the same frequency applied to

the actuator at the correct amplitude and phase should perfectly compensate for the vibrations. The use of stochastic gradient descent leads to an update relation which slowly changes phasors with components I_m and Q_m depending on the net microphonics detuning. The phasors in turn modulate carrier signals at the microphonics frequencies ω_m applied to the actuator thus completing the ANC feedback controller. The ANC algorithm is equivalent to a linear time invariant filter which allows for the computation of a frequency response. We use this response function to establish constraints on the adaptation rates μ_m and the controller phases ϕ_m in order to operate in the stable region. Finally we propose a modification which automatically minimizes the mean square of compensated detuning by adapting the value of the controller phase in response to changing tuner responses or changing vibration excitations. The effectiveness of the modified ANC algorithm was verified using numerical simulations before it was applied to the main linac cavities during rf operations of CBETA.

We applied various mitigation techniques on the main linac SRF cavities to reduce microphonics detuning. Passive measures included several modifications to the cryogenic system to damp thermo-acoustic oscillations and transients related to Helium flow which led to a reduction of peak detuning by at least a factor of 2. We further demonstrated the use of the active control system to achieve a stable reduction of microphonics typically by a factor of 2 without the need of detailed measurement of the tuner transfer function. Future work will involve finding the remaining sources of vibrations and eliminating them, incorporating automatic frequency tracking in the ANC algorithm in order to make it more robust, and devising an algorithm to automatically configure the ANC on multiple frequencies during operation. The ANC algorithm was put to use while commissioning the MLC for energy recovery operations.

6.2 RF Commissioning

The Main Linac Cryomodule (MLC) is responsible for energy recovery in CBETA and is operated at a large nominal loaded quality factor $Q_L \sim 6 \times 10^7$ in order to reduce average power requirements. Besides the crucial aspect of microphonics suppression, the commissioning process for the MLC also involves setting up the support equipment for stable operation. Each of the six 7-cell SRF cavities operating at 1.3 GHz inside the cryomodule are powered by separate Solid State Amplifiers (SSAs) with associated high level rf components. The initial performance of this equipment was affected by a manufacturing error on the high power rf circulators. Once these were repaired, all the components including the SSAs, circulators, rf couplers and waveguides were eventually tested to the full power requirements. The SSAs themselves are driven by the Low Level RF (LLRF) control system which measures the accelerating gradient inside the cavities and maintains them near to the desired set points. We use mixers to convert the 1.3 GHz signals to an Intermediate Frequency (IF) of 12.5 MHz which are then digitized by the LLRF to yield measurements of the voltage, forward and reverse travelling wave phasors. Initial commissioning of the LLRF involved the calibration of these signals. Besides the rf systems, SRF cavity operations also involve a cryogenic system responsible for sustaining the operating temperature of 1.8 K. We optimized the flow of liquid Helium through the cryomodule for maximum efficiency and minimum microphonics detuning.

Once the support systems for the SRF linac are configured, individual cavity commissioning is the next step. All rf cavities in CBETA were tuned to 1.2999 GHz, since one of the stiffened cavities in the MLC could not be tuned to the design frequency of 1.3 GHz. The commissioning procedure for the main

linac involves the adjustment of various gains, offsets, phase parameters and trip thresholds in the LLRF to establish stability of the accelerating gradient and ensure that the system protects itself from damage. While some of these steps can be done once, others need to be repeated on a daily basis to account for various drifts in the system. The daily start-up procedure includes cavity tuning, phase offset adjustment, microphonics measurement and beam based measurement of on-crest phase of all the cavities of the MLC. At the final stage of commissioning, the peak microphonics detuning was limited to 23 Hz among all the cavities which results in peak power requirements well within the capabilities of the SSAs providing rf power. While the short term stability of the accelerating field is near the specified tolerance of 10^{-4} of relative amplitude jitter on 4 out of the 6 cavities, we observe long term drift in amplitude on an unstiffened cavity. Regardless of these issues, energy recovery has been successfully demonstrated in the MLC cavities during 1-turn operations of CBETA with an energy balance efficiency of $99.4 \pm 0.1\%$.

Future work on rf commissioning will aim to optimize stability even further while preparing the system for very high beam currents up to 40 mA. The slow drift observed on one MLC cavity is a major outstanding issue. Measurement of ambient rf noise, cross-talk between the LLRF controllers of different cavities, response measurement of the Proportional-Integral feedback loops will likely improve the short term stability or jitter in the accelerating field. The uncertainty in phase rotation (offset) measurement may be improved by using the fast field phasor data instead of relying on averages. Preparation for high-current operations will involve extensive characterization of Higher Order Mode (HOM) excitations in the MLC, including measurement of heating in the HOM absorbers and observation of Beam Breakup Instability in the recirculat-

ing bunches. A detailed design of the current ramping system and compensating for the resulting transient beam loading will be critical in achieving stable high current energy recovery.

6.3 Transient Beam Loading

The energy recovery process in high-current ERLs is subject to transients during all modes of operation. Existing methods of analyzing transient beam loading rely on the notion of shunt impedance defined under the assumption of ultra-relativistic beams, while in contrast typical ERLs like CBETA operate in the medium energy range where relativistic effects become important. We present a self-consistent approach to calculating the longitudinal dynamics of a bunch traveling through a cavity by describing the field in terms of discrete eigen-modes which act as lossless simple harmonic oscillators coupled to the motion of macro-particles constituting the bunch. We show a numerical simulation of the model to study the evolution of the lower order modes in the fundamental pass-band of a 7-cell cavity during the passage of a single bunch. The results reveal energy conservation limited by the numerical precision of the calculation with a scale of 10^{-9} compared to the total energy transferred from the field to the beam. However, an approximation to this model, linear in bunch charge is sufficient to study transient beam loading in ERLs, since $\mathcal{E}_{gain}/\mathcal{E}_{fld} << 1$.

The circuit description of beam loading is equivalent to the linear model in the ultra-relativistic limit and does not show any measurable difference at low currents. However, during steady high-current ERL operation, the net induced phasor has a substantial imaginary component which results from the phase slip

of the low energy beam with respect to the phase velocity of the rf. While the exact amount is dependent on phasing, compensating for reactive beam loading directly using the rf power source would lead to prohibitively high power requirements, about 36.5 kW for the first main linac cavity of CBETA under the phasing used in the baseline design lattice. Detuning the cavity can compensate for this imaginary contribution of the induced impulse to the steady state mode phasor of the cavity. The required detuning of 158 Hz can reduce the power requirement dramatically to 40.4 W during continuous operations. On the other hand, it is possible to optimize the voltages and phases of the main linac cavities in order to minimize the forward power requirements without the need to detune them. This demonstrates the importance of reactive beam loading in ERLs which can not be predicted using the circuit model.

We analyze field transients and associated power requirements under high-gain proportional feedback control in various modes of operation. The analysis of bunch patterns suggest that while gaps are not acceptable within continuous bunch trains, the train length and repetition rate itself can be optimized to reduce transients while sustaining an arbitrary average beam current. Ramping beam during ERL startup is possible by steadily increasing the number of bunches in a single train while keeping the bunch charge constant and detuning the cavity proportional to the current to compensate for the reactive loading. Hence the ramp rate will be limited by how fast a resonance tuner can detune the cavity to minimize power consumption. During beam loss the maximum energy deposited by the residual stored beam into the cavity depends on total amount of stored charge in the return loop. If the energy deposited is large enough to drive a SRF cavity to it's quench field then fast kickers should be incorporated in the highest energy loop to prevent the remaining stored beam

to get decelerated. Based on this calculation CBETA will not require the use of fast kickers. Future research will concentrate on the implementation of the fast tuning system to automatically compensate for reactive beam loading.

6.4 Dynamic Temperature Mapping

While operating SRF cavities with narrow bandwidth and executing energy recovery are two ways of reducing the rf power requirements for linac operation, the use of new materials to lower heat dissipation on the cavity walls could result in significant gain of efficiency by reducing refrigeration demands. As an example, Nb_3Sn exhibits a much lower surface resistance at higher temperatures which makes this next leap in accelerator efficiency possible. However in experiments this material quenches at fields much lower than the predicted superheating field. In general, quenches arise from the onset of local heating on a cavity surface resulting from various processes including magnetic flux trapping, multipacting, field emission among others. The technique of cavity thermometry can be used to image local heating and measure heat flux on the surface which can enable the study of the underlying mechanisms. The Cornell T-map system uses 646 specially mounted carbon resistors as the active temperature sensing elements which are fixed all over the cavity surface to enable the observation of heat maps while the cavity is being tested with field. The mounting is designed to optimize heat transfer between the cavity surface and the resistor while insulating the path between the resistor and the Helium bath. We describe the operation of a new data acquisition system which is used to measure the resistance of these thermometers simultaneously at 50 ksps, and discuss the uncertainties of temperature and flux measurement.

The process of analyzing dynamic T-maps involve channel selection, resistance calibration, averaging and bath subtraction. Starting from when the whole cavity and the sensors equilibrate with the liquid Helium bath at 4.2 K, to the time, when the cryostat is cooled to $\approx$ 2 K, multiple short duration T-maps are acquired to serve as calibration measurements. Channel selection takes place at the lowest temperature by selecting the dominant cluster of points in the space of standard deviation v/s mean of the raw voltage data from the channels. Typically $\approx$ 10% of the channels are discarded. The resistance of the sensors is calibrated against a model which assumes that the carbon resistors act as small band gap semiconductors. Once each channel is separately calibrated, the model parameters can be used to convert a raw voltage measured by the acquisition system to a corresponding temperature. The systematic uncertainty σ_T^{syst} associated with the estimation of temperature is typically $\approx 15\ \mu$K at 2 K and $\approx 65\ \mu$K at 4.2 K owing to the smaller sensitivity of the resistance at higher temperatures. The acquired signals are subject to noise all over the frequency spectrum, with major contributions from the analog amplification circuit at $\gtrsim$ 10 kHz and temperature-dependent noise from the cryogenic system at $\lesssim$ 100 Hz. The noise spectrum gives rise to statistical uncertainties σ_T^{stat} in the measurement of temperature which is a function of the sample time. At 20 μs, the briefest sample time possible in the present system, and a bath temperature of 2 K, σ_T^{stat} is a few 100 μK, while this can be averaged out at intermediate sample rates where $\sigma_T^{\text{stat}} \sim 100\ \mu$K. Slow oscillations or drifts form a significant part of this residual uncertainty which can be reduced by subtracting away the slow variations in bath temperature using data from special sensors immersed in the Helium bath. Bath subtraction analysis allows the reduction of statistical uncertainty at 1 ksps to $\sigma_T^{\text{stat}} \sim 30\ \mu$K at which point it becomes comparable to

σ_T^{syst}.

The process of converting the observed thermometry data to thermal flux on the cavity surface is subject to various systematic uncertainties. Firstly, the thermal contact of the sensor with the surface and the altered flow of heat flux into the Helium bath in the presence of sensors give rise to a contact efficiency η_T which varies among sensors. While the measurement of η_T is possible by comparing observed temperature rise on the sensors at low field compared to ones predicted by thermal models, it is dependent on exact measurement of field in the cavity which itself introduces a systematic uncertainty of measurement. Further the limited spatial resolution of temperature measurement introduces an uncertainty in estimating the actual thermal flux since the position of the source of local heating is unknown. Future work will involve development of sophisticated thermal models taking into account measurements from multiple sensors to improve flux estimation. Efforts to reduce intermittent failures and data loss in the acquisition system are required to improve the overall reliability, while development of lower noise analog circuits can greatly reduce the statistical uncertainty of temperature measurement.

6.5 Outlook

The research projects reviewed in this dissertation focus on reducing electrical power required to operate SRF linacs used in modern particle accelerators. Chapters 2, 3 and 4 described the use of narrow bandwidth SRF cavities and the technique of energy recovery in an endeavor to reduce rf power requirements. Chapter 5 detailed a novel dynamic thermometry system which can be used

to characterize future SRF materials leading to potentially lower refrigeration requirements further boosting efficiency. An extension of this effort of improving efficiency in particle accelerators would naturally involve developing new technologies of beam transport which further reduce energy consumption. The fixed field alternating return arc of CBETA based on permanent magnets is an excellent example. In addition, SRF ERLs can be used for hadron cooling in an Electron-Ion Collider to preserve the luminosity of the stored beam. This precludes the use of an on-energy hadron injection system and hence greatly reduces power consumption of the facility. The work presented in this dissertation contributes to all of these applications.

APPENDIX A

IMPERFECT DIRECTIONAL COUPLERS

The dual directional coupler used for measuring beam loading in the main linac is effectively a 4-port device connected to the fundamental power coupler of the cavity. We use a simple circuit model to characterize the operation of this device. We define the excitation at the two waveguide ports 1 and 2, using complex voltage phasors $\tilde{V}_+$ and $\tilde{V}_-$, denoting the forward traveling wave entering port 1, exiting port 2 into the cavity and the reverse traveling wave reflected from the cavity entering port 2, exiting port 1 respectively. The ports 1 and 2 can transfer power in either direction with very little attenuation. The powers are defined as,

$$P_+ \equiv \frac{|\tilde{V}_+|^2}{2\frac{R}{Q}Q_L}\,, \tag{A.1a}$$

$$P_- \equiv \frac{|\tilde{V}_-|^2}{2\frac{R}{Q}Q_L}\,, \tag{A.1b}$$

where P_+, P_- are the actual forward and reflected powers respectively and $Q_L R/Q$ is the effective impedance of the fundamental power coupler and the cavity. In addition, two other ports 3 and 4 corresponding to phasors $\tilde{O}_+$ and $\tilde{O}_-$ couple to a small portion of the forward and reverse traveling waves respectively and these are used to measure the powers during machine operation. The observed phasors are linearly coupled to the actual traveling wave phasors through,

$$\begin{bmatrix} \tilde{O}_+ \\ \tilde{O}_- \end{bmatrix} = \begin{bmatrix} \tilde{M}_{11} & \tilde{M}_{12} \\ \tilde{M}_{21} & \tilde{M}_{22} \end{bmatrix} \begin{bmatrix} \tilde{V}_+ \\ \tilde{V}_- \end{bmatrix}, \tag{A.2}$$

where the elements of the 2x2 matrix encode the attenuation and phase relationships between the actual phasors and the coupled phasors. The matrix elements, $\tilde{M}_{12}$ and $\tilde{M}_{21}$ represent the cross-coupling in the directional coupler and

should ideally be 0. However, for any real directional coupler, we should take into account the presence of non-zero off diagonal elements since it affects the measurement of beam loading.

The process of calibration and measurement of forward and reflected powers used in CBETA directly affects the beam loading measurements. The coupled signals from ports 3 and 4 are detected by the rf control system as voltage phasors $\tilde{O}_+$ and $\tilde{O}_-$ respectively. The forward and reflected powers are measured as,

$$\tilde{P}_+ \equiv \kappa_+ |\tilde{O}_+|^2 \,, \tag{A.3a}$$

$$\tilde{P}_- \equiv \kappa_- |\tilde{O}_-|^2 \,, \tag{A.3b}$$

where κ_+ and κ_- are calibration factors. The process of calibration involves substituting the cavity with a shorted waveguide, which reflects the incoming wave with a phase shift of π, leading to $\tilde{V}_-^{\text{cal}} = -\tilde{V}_+^{\text{cal}}$, where cal represents the calibration measurements. Using Eq. (A.2), we can represent the observed phasors during calibration in terms of the actual phasors as $\tilde{O}_+^{\text{cal}} = (\tilde{M}_{11} - \tilde{M}_{12})\tilde{V}_+^{\text{cal}}$ and $\tilde{O}_-^{\text{cal}} = (\tilde{M}_{21} - \tilde{M}_{22})\tilde{V}_+^{\text{cal}}$. Further, we set up an independent measurement of forward power, directly from the rf power source yielding the correct value of P_+^{cal} for the calibration process. Using this known power measurement, the calibration constants are set to $\kappa_+ = P_+^{\text{cal}}/|\tilde{O}_+^{\text{cal}}|^2$ and $\kappa_- = P_+^{\text{cal}}/|\tilde{O}_-^{\text{cal}}|^2$. Combining these calculations for the calibration constants with the definition of actual powers in Eq. (A.1), we get

$$\kappa_+ = \frac{1}{2|\tilde{M}_{11} - \tilde{M}_{12}|^2 \frac{R}{Q} Q_L} \,, \tag{A.4a}$$

$$\kappa_- = \frac{1}{2|\tilde{M}_{21} - \tilde{M}_{22}|^2 \frac{R}{Q} Q_L} \,, \tag{A.4b}$$

where the matrix elements are still undetermined. We can use these relations

linking the calibration constants with the coupling matrix to determine the measured difference between forward and reflected power.

During normal operation, the amplitude and phase of the reflected wave $\tilde{V}_-$ depends on the resonant frequency of the cavity represented as a tuning phase ψ', the cavity voltage V_c, the Fourier amplitude of beam current I_b and the phasing of the beam. Using Eq. (**??**) and (1.31), the reflection coefficient of the cavity, defined as $\Gamma \equiv \tilde{V}_-/\tilde{V}_+ = \tilde{I}_-/\tilde{I}_+$ is given by,

$$\Gamma = -\frac{\frac{1-\beta}{1+\beta} + \frac{I_b}{V_c}\frac{R}{Q}Q_L e^{-i\phi_0} + i\tan\psi'}{1 + \frac{I_b}{V_c}\frac{R}{Q}Q_L e^{-i\phi_0} + i\tan\psi'}\,, \tag{A.5}$$

where $\beta \equiv Q_0/Q_{ext}$ is the coupling factor representing the ratio of intrinsic quality factor Q_0 and external quality factor Q_{ext} of the cavity, while ϕ_0 represents the phase of arrival of an ultra-relativistic beam with respect to the phase of maximum energy gain. In the case of the CBETA main linac, we operate the cavities in the over-coupled regime ($\beta >> 1$) while being tuned to the rf source frequency ($\psi' = 0$). This simplifies the expression of reflection factor to,

$$\Gamma = \frac{1 - \frac{I_b}{V_c}\frac{R}{Q}Q_L e^{-i\phi_0}}{1 + \frac{I_b}{V_c}\frac{R}{Q}Q_L e^{-i\phi_0}} \equiv \frac{1-f}{1+f}\,, \tag{A.6}$$

where we have defined $f \equiv \frac{I_b}{V_c}\frac{R}{Q}Q_L e^{-i\phi_0}$. Using the lumped circuit model for resonant cavities, we can further use $V_c = \tilde{V}_+ + \tilde{V}_-$ to write $\tilde{V}_+ = V_c/(1+\Gamma)$ and $\tilde{V}_- = \Gamma V_c/(1+\Gamma)$ which form theoretical estimates of the actual forward and reverse traveling wave phasors in the directional coupler.

We can now combine the theoretical estimates of the actual traveling wave phasors with the expressions for calibration factors to calculate the difference between observed forward and reflected powers. Using Eq. (A.3) and Eq. (A.4), we get

$$\tilde{P}_+ - \tilde{P}_- = \frac{|\tilde{O}_+|^2}{2|\tilde{M}_{11} - \tilde{M}_{12}|^2\frac{R}{Q}Q_L} - \frac{|\tilde{O}_-|^2}{2|\tilde{M}_{21} - \tilde{M}_{22}|^2\frac{R}{Q}Q_L}\,. \tag{A.7}$$

Plugging in Eq. (A.2) along with the expressions of estimated forward and reflected wave phasors and Eq. (A.6), we get

$$\tilde{P}_+ - \tilde{P}_- = V_c^2 \frac{|(1+f)\tilde{M}_{11} + (1-f)\tilde{M}_{12}|^2}{8|\tilde{M}_{11} - \tilde{M}_{12}|^2 \frac{R}{Q} Q_L} - V_c^2 \frac{|(1+f)\tilde{M}_{21} + (1-f)\tilde{M}_{22}|^2}{8|\tilde{M}_{21} - \tilde{M}_{22}|^2 \frac{R}{Q} Q_L} + O(f^2)\,, \tag{A.8}$$

where we have assumed that $\frac{I_b}{V_c}\frac{R}{Q}Q_L << 1$. Simplifying the expression we get,

$$\begin{aligned}\tilde{P}_+ - \tilde{P}_- = \frac{V_c^2}{8\frac{R}{Q}Q_L}\left\{\frac{|\tilde{M}_{11} + \tilde{M}_{12}|^2}{|\tilde{M}_{11} - \tilde{M}_{12}|^2} - \frac{|\tilde{M}_{21} + \tilde{M}_{22}|^2}{|\tilde{M}_{21} - \tilde{M}_{22}|^2}\right\} + \frac{V_c^2}{8\frac{R}{Q}Q_L}\Bigg\{ \\ \frac{f(\tilde{M}_{11} + \tilde{M}_{12})^*(\tilde{M}_{11} - \tilde{M}_{12}) + f^*(\tilde{M}_{11} + \tilde{M}_{12})(\tilde{M}_{11} - \tilde{M}_{12})^*}{|\tilde{M}_{11} - \tilde{M}_{12}|^2} \\ - \frac{f(\tilde{M}_{21} + \tilde{M}_{22})^*(\tilde{M}_{21} - \tilde{M}_{22}) + f^*(\tilde{M}_{21} + \tilde{M}_{22})(\tilde{M}_{21} - \tilde{M}_{22})^*}{|\tilde{M}_{21} - \tilde{M}_{22}|^2}\Bigg\} + O(f^2)\,.\end{aligned} \tag{A.9}$$

The first term is independent of f and consequently beam current, so we denote it as a constant,

$$\tilde{P}_c \equiv \frac{V_c^2}{8\frac{R}{Q}Q_L}\left\{\frac{|\tilde{M}_{11} + \tilde{M}_{12}|^2}{|\tilde{M}_{11} - \tilde{M}_{12}|^2} - \frac{|\tilde{M}_{21} + \tilde{M}_{22}|^2}{|\tilde{M}_{21} - \tilde{M}_{22}|^2}\right\}. \tag{A.10}$$

If we had a perfect directional coupler, corresponding to the limit $\tilde{M}_{12} = \tilde{M}_{21} \to 0$, then $\tilde{P}_c \to 0$, which is consistent with negligible power dissipation as expected, when a cavity is operated with $\beta >> 1$. Plugging the above definition into Eq. (A.9) and simplifying, we get,

$$\begin{aligned}\tilde{P}_+ - \tilde{P}_- = \tilde{P}_c + \frac{V_c^2}{8\frac{R}{Q}Q_L}\Bigg\{\frac{(f+f^*)(|\tilde{M}_{11}|^2 - |\tilde{M}_{12}|^2) - (f-f^*)(\tilde{M}_{11}^*\tilde{M}_{12} - \tilde{M}_{11}\tilde{M}_{12}^*)}{|\tilde{M}_{11} - \tilde{M}_{12}|^2} \\ - \frac{(f+f^*)(|\tilde{M}_{21}|^2 - |\tilde{M}_{22}|^2) - (f-f^*)(\tilde{M}_{21}^*\tilde{M}_{22} - \tilde{M}_{21}\tilde{M}_{22}^*)}{|\tilde{M}_{21} - \tilde{M}_{22}|^2}\Bigg\} + O(f^2)\,.\end{aligned} \tag{A.11}$$

We now recognize that $f \equiv \frac{I_b}{V_c}\frac{R}{Q}Q_L e^{-i\phi_0} \approx \frac{I_b}{V_c}\frac{R}{Q}Q_L \cos\phi_0(1 - i\phi_0)$, for a beam which is close to the perfectly accelerating or the decelerating phase. Further in a practical differential coupler, $\tilde{M}_{12} = \delta_1\tilde{M}_{11}$ and $\tilde{M}_{21} = \delta_2\tilde{M}_{22}$, where $|\delta_1|, |\delta_2| << 1$.

Simplifying Eq. (A.11) under these approximations and keeping only the first order terms,

$$\tilde{P}_+ - \tilde{P}_- = \tilde{P}_c + \frac{IV_c \cos\phi_0}{2}\left\{\frac{|\tilde{M}_{11}|^2 - |\tilde{M}_{12}|^2}{|\tilde{M}_{11} - \tilde{M}_{12}|^2} - \frac{|\tilde{M}_{21}|^2 - |\tilde{M}_{22}|^2}{|\tilde{M}_{21} - \tilde{M}_{22}|^2}\right\} + O(I^2)\,, \tag{A.12}$$

where we have substituted the Fourier amplitude of the beam current, I_b, with the measured beam current, I, where $I_b = 2I$. Finally, defining a constant $\chi \equiv 0.5\{(|\tilde{M}_{11}|^2 - |\tilde{M}_{12}|^2)/|\tilde{M}_{11} - \tilde{M}_{12}|^2 - (|\tilde{M}_{21}|^2 - |\tilde{M}_{22}|^2)/|\tilde{M}_{21} - \tilde{M}_{22}|^2\}$, we arrive at a simple expression for the difference between measured forward and reflected power,

$$\tilde{P}_+ - \tilde{P}_- = \tilde{P}_c + \chi I V_c \cos\phi_0 + O(I^2)\,, \tag{A.13}$$

which is valid in the regime $\frac{I_b}{V_c}\frac{R}{Q}Q_L << 1$.

BIBLIOGRAPHY

Dan T. Abell, Nathan M. Cook, and Stephen D. Webb. Symplectic modeling of beam loading in electromagnetic cavities. *Phys. Rev. Accel. Beams*, 20:052002, May 2017. doi: 10.1103/PhysRevAccelBeams.20.052002. URL https://link.aps.org/doi/10.1103/PhysRevAccelBeams.20.052002.

Mitsuo Akemoto, Dai Arakawa, Seiji Asaoka, Enrico Cenni, Masato Egi, Kazuhiro Enami, Kuninori Endo, Shigeki Fukuda, Takaaki Furuya, Kaiichi Haga, et al. Construction and commissioning of the compact energy-recovery linac at kek. *Nuclear Instruments and Methods in Physics Research Section A: Accelerators, Spectrometers, Detectors and Associated Equipment*, 877:197 – 219, 2018. ISSN 0168-9002. doi: https://doi.org/10.1016/j.nima.2017.08.051. URL http://www.sciencedirect.com/science/article/pii/S0168900217309518.

Jay Amrit and Claire Z. Antoine. Kapitza resistance cooling of single crystal (111) niobium for superconducting rf cavities. *Phys. Rev. ST Accel. Beams*, 13: 023201, Feb 2010. doi: 10.1103/PhysRevSTAB.13.023201. URL https://link.aps.org/doi/10.1103/PhysRevSTAB.13.023201.

S. Antipov, E. Efimenko, A. Romanenko, and D. A. Sergatskov. Time-Resolved Measurements of High-Field Quench in SRF Cavities. In *Proc. 16th Int. Conf. RF Superconductivity (SRF'13): Paris, France*, pages 743–746, 2013. URL https://accelconf.web.cern.ch/SRF2013/papers/tup112.pdf. TUP112.

Michaela Arnold, Jonny Birkhan, Jonas Pforr, Norbert Pietralla, Felix Schließmann, Manuel Steinhorst, and Florian Hug. First operation of the superconducting darmstadt linear electron accelerator as an energy recov-

ery linac. *Phys. Rev. Accel. Beams*, 23:020101, Feb 2020. doi: 10.1103/PhysRevAccelBeams.23.020101. URL https://link.aps.org/doi/10.1103/PhysRevAccelBeams.23.020101.

N.W. Ashcroft and N.D. Mermin. *Solid State Physics*. Cengage Learning, 1976. URL https://www.amazon.com/Solid-State-Physics-Neil-Ashcroft/dp/0030839939.

J. Balewski, J. Bernauer, J. Bessuille, R. Corliss, R. Cowan, C. Epstein, P. Fisher, D. Hasell, E. Ihloff, Y. Kahn, et al. The darklight experiment: A precision search for new physics at low energies. *arXiv*, physics.ins-det:1412.4717, 2014. URL https://arxiv.org/abs/1412.4717.

N Banerjee, J Dobbins, F Furuta, G Hoffstaetter, R Kaplan, M Liepe, P Quigley, E Smith, and V Veshcherevich. Microphonics suppression in the cbeta linac cryomodules. *Journal of Physics: Conference Series*, 1067(8):082004, 2018. URL http://stacks.iop.org/1742-6596/1067/i=8/a=082004.

N. Banerjee et al. Microphonics Studies of the CBETA Linac Cryomodules. In *Proc. of International Particle Accelerator Conference (IPAC'17), Copenhagen, Denmark, 14-19 May, 2017*, number 8 in International Particle Accelerator Conference, pages 1138–1141, Geneva, Switzerland, May 2017. JACoW. ISBN 978-3-95450-182-3. doi: https://doi.org/10.18429/JACoW-IPAC2017-MOPVA122. URL http://jacow.org/ipac2017/papers/mopva122.pdf. https://doi.org/10.18429/JACoW-IPAC2017-MOPVA122.

Nilanjan Banerjee, Georg Hoffstaetter, Matthias Liepe, Peter Quigley, and Zeyu Zhou. Active suppression of microphonics detuning in high Q_L cavities. *Phys. Rev. Accel. Beams*, 22:052002, May 2019. doi: 10.1103/

PhysRevAccelBeams.22.052002. URL https://link.aps.org/doi/10.1103/PhysRevAccelBeams.22.052002.

J. Bardeen, L. N. Cooper, and J. R. Schrieffer. Microscopic theory of superconductivity. *Phys. Rev.*, 106:162–164, Apr 1957. doi: 10.1103/PhysRev.106.162. URL https://link.aps.org/doi/10.1103/PhysRev.106.162.

A. Bartnik, N. Banerjee, D. Burke, J. Crittenden, K. Deitrick, J. Dobbins, C. Gulliford, G. H. Hoffstaetter, Y. Li, W. Lou, P. Quigley, D. Sagan, K. Smolenski, J. S. Berg, S. Brooks, R. Hulsart, G. Mahler, F. Meot, R. Michnoff, S. Peggs, T. Roser, D. Trbojevic, N. Tsoupas, and T. Miyajima. Cbeta: First multipass superconducting linear accelerator with energy recovery. *Phys. Rev. Lett.*, 125:044803, Jul 2020. doi: 10.1103/PhysRevLett.125.044803. URL https://link.aps.org/doi/10.1103/PhysRevLett.125.044803.

S. Belomestnykh and H. Padamsee. Performance of the CESR Superconducting RF System and Future Plans. In *Proceedings, 10th International Conference on RF Superconductivity (SRF2010), Tsukuba, Japan, September 6-11*, 2001. URL https://accelconf.web.cern.ch/srf01/papers/sa003.pdf.

Ilan Ben-Zvi. Superconducting energy recovery linacs. *Superconductor Science and Technology*, 29(10):103002, sep 2016. doi: 10.1088/0953-2048/29/10/103002. URL https://doi.org/10.1088%2F0953-2048%2F29%2F10%2F103002.

Ilan Ben-Zvi and Vadim Ptitsyn. *Electron Proton and Electron Ion Colliders*, pages 77–114. WORLD SCIENTIFIC, 2015. doi: 10.1142/9789814651493_0005. URL https://www.worldscientific.com/doi/abs/10.1142/9789814651493_0005.

J. Scott Berg, Stephen Brooks, James Crittenden, Yulin Li, Christopher Mayes, Francois Méot, Dejan Trbojevic, and Nicholaos Tsoupas. CBETA FFAG Beam Optics Design. In *59th ICFA Advanced Beam Dynamics Workshop on Energy Recovery Linacs*, page TUIDCC004, 2018. doi: 10.18429/JACoW-ERL2017-TUIDCC004. URL https://doi.org/10.18429/JACoW-ERL2017-TUIDCC004.

A. Boucheffa, M.X. François, and F. Koechlin. Kapitza resistance and thermal conductivity for niobium. *Cryogenics*, 34:297 – 300, 1994. ISSN 0011-2275. doi: https://doi.org/10.1016/S0011-2275(05)80066-9. URL http://www.sciencedirect.com/science/article/pii/S0011227505800669. Fifteenth International Cryogenic Engineering Conference.

J. Branlard, V. Ayvazyan, L. Butkowski, H. Schlarb, J. Sekutowicz, W. Cichalewski, A. Piotrowski, K. Przygoda, W. Jalmuzna, and J Szewinski. Llrf system design and performance for xfel cryomodules continuous wave operation. *SRF Workshop*, 2013. URL https://accelconf.web.cern.ch/srf2013/papers/thp086.pdf. THP086.

J. M. Byrd, S. De Santis, J. Jacob, and V. Serriere. Transient beam loading effects in harmonic rf systems for light sources. *Phys. Rev. ST Accel. Beams*, 5:092001, Sep 2002. doi: 10.1103/PhysRevSTAB.5.092001. URL https://link.aps.org/doi/10.1103/PhysRevSTAB.5.092001.

A. D. Cahill, J. B. Rosenzweig, V. A. Dolgashev, S. G. Tantawi, and S. Weathersby. High gradient experiments with x-band cryogenic copper accelerating cavities. *Phys. Rev. Accel. Beams*, 21:102002, Oct 2018. doi: 10.1103/

PhysRevAccelBeams.21.102002. URL https://link.aps.org/doi/10.1103/PhysRevAccelBeams.21.102002.

Jared Carlson, Alden Pack, Mark K. Transtrum, Jaeyel Lee, David N. Seidman, Danilo B. Liarte, Nathan Sitaraman, Alen Senanian, James P. Sethna, Tomas Arias, and Sam Posen. Analysis of magnetic vortex dissipation in sn-segregated boundaries in nb_3sn srf cavities. *arXiv*, cond-mat.supr-con: 2003.03362, 2020. URL https://arxiv.org/abs/2003.03362.

Alexander Wu Chao, Karl Hubert Mess, Maury Tigner, and Frank Zimmermann. *Handbook of Accelerator Physics and Engineering*. WORLD SCIENTIFIC, 2nd edition, 2013. doi: 10.1142/8543. URL https://www.worldscientific.com/doi/abs/10.1142/8543.

Wojciech Cichalewski, Julien Branlard, Andrzej Napieralski, and Christian Schmidt. European XFEL Cavities Piezoelectric Tuners Control Range Optimization. In *Proceedings, 15th International Conference on Accelerator and Large Experimental Physics Control Systems (ICALEPCS 2015), Melbourne, Australia, October 17-23*, 2015. URL https://doi.org/10.18429/JACoW-ICALEPCS2015-MOPGF079.

G. Ciovati. AC/RF Superconductivity. In *CERN Accelerator School: Course on Superconductivity for Accelerators*, pages 57–75, 2014. doi: 10.5170/CERN-2014-005.57. URL http://dx.doi.org/10.5170/CERN-2014-005.57.

E. U. Condon. Forced oscillations in cavity resonators. *Journal of Applied Physics*, 12(2):129–132, 1941. doi: 10.1063/1.1712882. URL https://doi.org/10.1063/1.1712882.

Zachary Conway and Matthias Liepe. Fast Piezoelectric Actuator Control of Microphonics in the CW Cornell ERL Injector Cryomodule. In *Particle accelerator. Proceedings, 23rd Conference, PAC'09, Vancouver, Canada, May 4-8, 2009*, page TU5PFP043, 2010. URL http://accelconf.web.cern.ch/AccelConf/PAC2009/papers/tu5pfp043.pdf.

Leon N. Cooper. Bound electron pairs in a degenerate fermi gas. *Phys. Rev.*, 104: 1189–1190, Nov 1956. doi: 10.1103/PhysRev.104.1189. URL https://link.aps.org/doi/10.1103/PhysRev.104.1189.

G. Devanz. Multipactor simulations in superconducting cavities and power couplers. *Phys. Rev. ST Accel. Beams*, 4:012001, Jan 2001. doi: 10.1103/PhysRevSTAB.4.012001. URL https://link.aps.org/doi/10.1103/PhysRevSTAB.4.012001.

P. Dhakal, G. Ciovati, G. R. Myneni, K. E. Gray, N. Groll, P. Maheshwari, D. M. McRae, R. Pike, T. Proslier, F. Stevie, R. P. Walsh, Q. Yang, and J. Zasadzinzki. Effect of high temperature heat treatments on the quality factor of a large-grain superconducting radio-frequency niobium cavity. *Phys. Rev. ST Accel. Beams*, 16:042001, Apr 2013. doi: 10.1103/PhysRevSTAB.16.042001. URL https://link.aps.org/doi/10.1103/PhysRevSTAB.16.042001.

Pashupati Dhakal, Gianluigi Ciovati, Peter Kneisel, and Ganapati Rao Myneni. Superconducting dc and rf properties of ingot niobium. In *Proc. 15th Int. Conf. RF Superconductivity (SRF'11),*, Chicago, IL, USA, 2011. URL https://arxiv.org/abs/1202.0811.

L. Doolittle, G. Huang, A. Ratti, C. Serrano, R. Bachimanchi, C. Hovater, S. Babel, B. Hong, D. Van Winkle, B. Chase, E. Cullerton, and P. Varghese. The

LCLS-II LLRF system. In *Proceedings, International Particle Accelerator Conference (IPAC'15), Richmond, USA, May 3-8*, Geneva, Switzerland, 2015. JACoW. URL https://doi.org/10.18429/JACoW-IPAC2015-MOPWI021.

Bruce Dunham, John Barley, Adam Bartnik, Ivan Bazarov, Luca Cultrera, John Dobbins, Georg Hoffstaetter, Brent Johnson, Roger Kaplan, Siddharth Karkare, Vaclav Kostroun, Yulin Li, Matthias Liepe, Xianghong Liu, Florian Loehl, Jared Maxson, Peter Quigley, John Reilly, David Rice, Daniel Sabol, Eric Smith, Karl Smolenski, Maury Tigner, Vadim Vesherevich, Dwight Widger, and Zhi Zhao. Record high-average current from a high-brightness photoinjector. *Applied Physics Letters*, 102(3):034105, 2013. doi: 10.1063/1.4789395. URL https://doi.org/10.1063/1.4789395.

R. Eichhorn, B. Bullock, B. Elmore, B. Clasby, F. Furuta, Y. He, G. Hoffstaetter, M. Liepe, T. O'Connell, J. Conway, P. Quigley, D. Sabol, J. Sears, E. Smith, and V. Veshcherevich. The cornell main linac cryomodule: A full scale, high q accelerator module for cw application. *Physics Procedia*, 67:785 – 790, 2015. ISSN 1875-3892. doi: https://doi.org/10.1016/j.phpro.2015.06.133. URL http://www.sciencedirect.com/science/article/pii/S1875389215005143. Proceedings of the 25th International Cryogenic Engineering Conference and International Cryogenic Materials Conference 2014.

Ralf Eichhorn et al. Cornell's Main Linac Cryomodule for the Energy Recovery Linac Project. In *Proceedings, 5th International Particle Accelerator Conference (IPAC 2014): Dresden, Germany, June 15-20*, number 5 in International Particle Accelerator Conference, page WEPRI061, Geneva, Switzerland, June 2014. JACoW Publishing. URL https://accelconf.web.cern.ch/ipac2014/papers/wepri061.pdf.

Ralf Eichhorn et al. First Cool-down of the Cornell ERL Main Linac Cryomodule. In *Proceedings, 7th International Particle Accelerator Conference (IPAC 2016): Busan, Korea, May 8-13, 2016*, page WEPMR020, 2016. doi: 10.18429/JACoW-IPAC2016-WEPMR020. URL http://inspirehep.net/record/1470183/files/wepmr020.pdf.

S. J. Elliott, M. Ghandchi Tehrani, and R. S. Langley. Nonlinear damping and quasi-linear modelling. *Philosophical Transactions of the Royal Society of London A: Mathematical, Physical and Engineering Sciences*, 373(2051), 2015. ISSN 1364-503X. doi: 10.1098/rsta.2014.0402. URL http://rsta.royalsocietypublishing.org/content/373/2051/20140402.

Enclustra FPGA Solutions. Mars ZX2. https://www.enclustra.com/en/products/system-on-chip-modules/mars-zx2/. [Online; accessed 25-October-2020].

Fumio Furuta et al. ERL Main Linac Cryomodule Cavity Performance and Effect of Thermal Cycling. In *Proceedings, 7th International Particle Accelerator Conference (IPAC 2016): Busan, Korea, May 8-13, 2016*, page WEPMR022, 2016. doi: 10.18429/JACoW-IPAC2016-WEPMR022. URL http://accelconf.web.cern.ch/ipac2016/doi/JACoW-IPAC2016-WEPMR022.html.

Fumio Furuta et al. Performance of the Novel Cornell ERL Main Linac Prototype Cryomodule. In *Proceedings, 28th International Linear Accelerator Conference (LINAC16): East Lansing, Michigan, September 25-30, 2016*, page TUPLR011, 2017. doi: 10.18429/JACoW-LINAC2016-TUPLR011. URL http://inspirehep.net/record/1633195/files/tuplr011.pdf.

Mingqi Ge, Nilanjan Banerjee, John Dobbins, Ralf Eichhorn, Fumio Furuta, Georg Hoffstaetter, Matthias Liepe, Peter Quigley, James Sears, and Vadim

Veshcherevich. Measurements and Analysis of Cavity Microphonics and Frequency Control in the Cornell ERL Main Linac Prototype Cryomodule. In *Proceedings, 28th International Linear Accelerator Conference (LINAC16): East Lansing, Michigan, September 25-30, 2016*, page TUPLR010, 2017. doi: 10.18429/JACoW-LINAC2016-TUPLR010. URL http://inspirehep.net/record/1633194/files/tuplr010.pdf.

Z. Geng. Rf control optimization and automation for normal conducting linear accelerators. *IEEE Transactions on Nuclear Science*, 64(8):2361–2368, 2017. URL https://doi.org/10.1109/TNS.2017.2723508.

A Grassellino, A Romanenko, Y Trenikhina, M Checchin, M Martinello, O S Melnychuk, S Chandrasekaran, D A Sergatskov, S Posen, A C Crawford, S Aderhold, and D Bice. Unprecedented quality factors at accelerating gradients up to 45 mvm^{-1} in niobium superconducting resonators via low temperature nitrogen infusion. *Superconductor Science and Technology*, 30(9):094004, aug 2017. doi: 10.1088/1361-6668/aa7afe. URL https://doi.org/10.1088%2F1361-6668%2Faa7afe.

S. Grieser, D. Bonaventura, P. Brand, C. Hargens, B. Hetz, L. Lessmann, C. Westphalinger, and A. Khoukaz. A cryogenic supersonic jet target for electron scattering experiments at magix@mesa and mami. *Nuclear Instruments and Methods in Physics Research Section A: Accelerators, Spectrometers, Detectors and Associated Equipment*, 906:120 – 126, 2018. ISSN 0168-9002. doi: https://doi.org/10.1016/j.nima.2018.07.076. URL http://www.sciencedirect.com/science/article/pii/S0168900218309124.

C. Gulliford, N. Banerjee, A. Bartnik, J. S. Berg, J. Crittenden, J. Dobbins, R. Hulsart, J. Jones, D. J. Kelliher, B. Kuske, W. Lou, M. McAteer, R. Michnoff,

S. Peggs, P. Quigley, D. Sagan, K. Smolenski, V. Vesherevich, D. Widger, G. H. Hoffstaetter, and D. Trbojevic. Beam commissioning results from the cbeta fractional arc test. *arxiv*, physics.acc-ph:1902.03370, 2019. URL https://arxiv.org/abs/1902.03370.

C. Gulliford, N. Banerjee, A. Bartnik, J. Crittenden, K. Deitrick, G. H. Hoffstaetter, P. Quigley, K. Smolenski, J. S. Berg, R. Michnoff, S. Peggs, and D. Trbojevic. Measurement of the per cavity energy recovery efficiency in the single turn cbeta configuration. *arXiv*, physics.acc-ph:2010.14983, 2020. URL https://arxiv.org/abs/2010.14983.

D.L. Hall et al. Cavity Quench Studies in Nb3Sn Using Temperature Mapping and Surface Analysis of Cavity Cut-outs. In *Proc. of International Conference on RF Superconductivity (SRF'17), Lanzhou, China, July 17-21, 2017*, number 18 in International Conference on RF Superconductivity, pages 840–843, Geneva, Switzerland, Jan. 2018. JACoW. ISBN 978-3-95450-191-5. URL https://doi.org/10.18429/JACoW-SRF2017-THPB041.

B J Hansen, O Al Atassi, R Bossert, J Einstein-Curtis, J Holzbauer, W Hughes, J Hurd, J Kaluzny, A Klebaner, J Makara, Y Pischalnikov, W Schappert, R Stanek, J Theilacker, R Wang, and M J White. Effects of thermal acoustic oscillations on lcls-ii cryomodule testing. *IOP Conference Series: Materials Science and Engineering*, 278(1):012188, 2017. URL http://stacks.iop.org/1757-899X/278/i=1/a=012188.

Y. He, G. H. Hoffstaetter, M. Liepe, M. Tigner, and E. N. Smith. Cryogenic Distribution System for the Proposed Cornell ERL Main Linac. In *Proceedings, 3rd International Conference on Particle accelerator (IPAC 2012): New Orleans,*

USA, May 2-25, 2012, volume C1205201, pages 619–621, 2012. URL https://accelconf.web.cern.ch/IPAC2012/papers/MOPPP026.PDF.

G. H. Hoffstaetter et al. CBETA Design Report, Cornell-BNL ERL Test Accelerator. *arXiv*, physics.acc-ph:1706.04245, 2017. URL https://arxiv.org/abs/1706.04245.

Georg H. Hoffstaetter and Ivan V. Bazarov. Beam-breakup instability theory for energy recovery linacs. *Phys. Rev. ST Accel. Beams*, 7:054401, May 2004. doi: 10.1103/PhysRevSTAB.7.054401. URL https://link.aps.org/doi/10.1103/PhysRevSTAB.7.054401.

Jeremiah Holzbauer, Brian Chase, Lawrence Doolittle, Joshua Einstein-Curtis, Yuriy Pischalnikov, Warren Schappert, and Carlos Serrano. Active Microphonics Compensation for LCLS-II. In *Proceedings, 9th International Particle Accelerator Conference (IPAC 2018): Vancouver, BC Canada, April 29-May 4, 2018*, page WEPML007, 2018. doi: 10.18429/JACoW-IPAC2018-WEPML007. URL http://lss.fnal.gov/archive/2018/conf/fermilab-conf-18-612-ad-td.pdf.

T.H. Kandil, H.K. Khalil, J. Vincent, T.L. Grimm, W. Hartung, J. Popielarski, R.C. York, and S. Seshagiri. Adaptive feedforward cancellation of sinusoidal disturbances in superconducting rf cavities. *Nuclear Instruments and Methods in Physics Research Section A: Accelerators, Spectrometers, Detectors and Associated Equipment*, 550(3):514 – 520, 2005. ISSN 0168-9002. doi: https://doi.org/10.1016/j.nima.2005.05.060. URL http://www.sciencedirect.com/science/article/pii/S0168900205012830.

Ivan Karpov and Philippe Baudrenghien. Transient beam loading and rf power evaluation for future circular colliders. *Phys. Rev. Accel. Beams*, 22:081002, Aug

2019. doi: 10.1103/PhysRevAccelBeams.22.081002. URL https://link.aps.org/doi/10.1103/PhysRevAccelBeams.22.081002.

S. A. Kivelson and D. S. Rokhsar. Bogoliubov quasiparticles, spinons, and spin-charge decoupling in superconductors. *Phys. Rev. B*, 41:11693–11696, Jun 1990. doi: 10.1103/PhysRevB.41.11693. URL https://link.aps.org/doi/10.1103/PhysRevB.41.11693.

J. Knobloch. Field emission and thermal breakdown in superconducting niobium cavities for accelerators. *IEEE Transactions on Applied Superconductivity*, 9(2):1016–1022, 1999. doi: 10.1109/77.783471. URL https://doi.org/10.1109/77.783471.

Jens Knobloch. *Advanced Thermometry Studies of Superconducting Radio-Frequency Cavities*. PhD thesis, Cornell University, Ithaca, NY, 1997. URL https://ui.adsabs.harvard.edu/abs/1997PhDT.......166K.

I. V. Konoplev, K. Metodiev, A. J. Lancaster, G. Burt, R. Ainsworth, and A. Seryi. Experimental studies of 7-cell dual axis asymmetric cavity for energy recovery linac. *Phys. Rev. Accel. Beams*, 20:103501, Oct 2017. doi: 10.1103/PhysRevAccelBeams.20.103501. URL https://link.aps.org/doi/10.1103/PhysRevAccelBeams.20.103501.

R. Koscica, N. Banerjee, G. H. Hoffstaetter, W. Lou, and G. Premawardhana. Energy and rf cavity phase symmetry enforcement in multiturn energy recovery linac models. *Phys. Rev. Accel. Beams*, 22:091602, Sep 2019. doi: 10.1103/PhysRevAccelBeams.22.091602. URL https://link.aps.org/doi/10.1103/PhysRevAccelBeams.22.091602.

P.N. Koufalis, D.L. Hall, M. Liepe, and J.T. Maniscalco. Effects of Interstitial

Oxygen and Carbon on Niobium Superconducting Cavities. *arXiv*, 2016. URL https://arxiv.org/abs/1612.08291. 1612.08291.

Geoffrey A. Krafft and Gerd Priebe. Compton sources of electromagnetic radiation. *Reviews of Accelerator Science and Technology*, 03(01):147–163, 2010. doi: 10.1142/S1793626810000440. URL https://doi.org/10.1142/S1793626810000440.

S. M. Kuo and D. R. Morgan. Active noise control: a tutorial review. *Proceedings of the IEEE*, 87(6):943–973, June 1999. ISSN 0018-9219. doi: 10.1109/5.763310. URL https://ieeexplore.ieee.org/document/763310.

Danilo B Liarte, Sam Posen, Mark K Transtrum, Gianluigi Catelani, Matthias Liepe, and James P Sethna. Theoretical estimates of maximum fields in superconducting resonant radio frequency cavities: stability theory, disorder, and laminates. *Superconductor Science and Technology*, 30(3):033002, jan 2017. doi: 10.1088/1361-6668/30/3/033002. URL https://doi.org/10.1088/1361-6668/30/3/033002.

Danilo B. Liarte, Daniel Hall, Peter N. Koufalis, Akira Miyazaki, Alen Senanian, Matthias Liepe, and James P. Sethna. Vortex dynamics and losses due to pinning: Dissipation from trapped magnetic flux in resonant superconducting radio-frequency cavities. *Phys. Rev. Applied*, 10:054057, Nov 2018. doi: 10.1103/PhysRevApplied.10.054057. URL https://link.aps.org/doi/10.1103/PhysRevApplied.10.054057.

M. Liepe, S. Belomestnykh, J. Dobbins, R. Kaplan, C. Strohman, and B. Stuhl. Experience with the new digital rf control system at the cesr storage ring. In *Proceedings of the 2005 Particle Accelerator Conference*, pages 2592–2594, May

2005. doi: 10.1109/PAC.2005.1591193. URL https://ieeexplore.ieee.org/document/1591193.

M. Liepe, D. L. Hartill, G. H. Hoffstaetter, S. Posen, P. Quigley, and V. Veshcherevich. Experience with the Cornell ERL Injector SRF Cryomodule during High Beam Current Operation. In *Particle accelerator. Proceedings, 2nd International Conference, IPAC 2011, San Sebastian, Spain, September 4-9, 2011*, volume C110904, pages 35–37, 2011. URL https://accelconf.web.cern.ch/IPAC2011/papers/mooda01.pdf.

M. Liepe, G. H. Hoffstaetter, S. Posen, P. Quigley, and V. Veshcherevich. High Current Operation of the Cornell ERL Superconducting RF Injector Cryomodule. In *Proceedings, 3rd International Conference on Particle accelerator (IPAC 2012): New Orleans, USA, May 2-25, 2012*, volume C1205201, pages 2378–2380, 2012. URL https://accelconf.web.cern.ch/IPAC2012/papers/weppc072.pdf.

Matthias Liepe, Sergey Belomestnykh, Eric Chojnacki, Zachary Conway, Valeri Medjidzade, Hasan Padamsee, Peter Quigley, James Sears, Valery Shemelin, and Vadim Veshcherevich. SRF Experience with the Cornell High-Current ERL Injector Prototype. In *Particle accelerator. Proceedings, 23rd Conference, PAC'09, Vancouver, Canada, May 4-8, 2009*, page TU3RAI01, 2010. URL http://accelconf.web.cern.ch/AccelConf/PAC2009/papers/tu3rai01.pdf.

H. Luck and Ch. Trepp. Thermoacoustic oscillations in cryogenics. part 1: basic theory and experimental verification. *Cryogenics*, 32(8):690 – 697, 1992. ISSN 0011-2275. doi: https://doi.org/10.1016/0011-2275(92)

90277-H. URL http://www.sciencedirect.com/science/article/pii/001122759290277H.

P. Marchand, T. Ruan, F. Ribeiro, and R. Lopes. High power 352 mhz solid state amplifiers developed at the synchrotron soleil. *Phys. Rev. ST Accel. Beams*, 10:112001, Nov 2007. doi: 10.1103/PhysRevSTAB.10.112001. URL https://link.aps.org/doi/10.1103/PhysRevSTAB.10.112001.

T. Mastorides, C. Rivetta, J. D. Fox, D. Van Winkle, and P. Baudrenghien. Rf system models for the cern large hadron collider with application to longitudinal dynamics. *Phys. Rev. ST Accel. Beams*, 13:102801, Oct 2010. doi: 10.1103/PhysRevSTAB.13.102801. URL https://link.aps.org/doi/10.1103/PhysRevSTAB.13.102801.

MathWorks®. Zero-phase digital filtering - MATLAB filtfilt. https://www.mathworks.com/help/signal/ref/filtfilt.html. [Online; accessed 28-October-2020].

Lia Merminga, David R. Douglas, and Geoffrey A. Krafft. High-current energy-recovering electron linacs. *Annual Review of Nuclear and Particle Science*, 53 (1):387–429, 2003. doi: 10.1146/annurev.nucl.53.041002.110456. URL https://doi.org/10.1146/annurev.nucl.53.041002.110456.

N Nakamura, R Kato, T Miyajima, M Shimada, T Hotei, and R Hajima. S2e simulation of an ERL-based high-power EUV-FEL source for lithography. *Journal of Physics: Conference Series*, 874:012013, jul 2017. doi: 10.1088/1742-6596/874/1/012013. URL https://doi.org/10.1088%2F1742-6596%2F874%2F1%2F012013.

G.R. Neil, C. Behre, S.V. Benson, M. Bevins, G. Biallas, J. Boyce, J. Coleman,

L.A. Dillon-Townes, D. Douglas, H.F. Dylla, et al. The jlab high power erl light source. *Nuclear Instruments and Methods in Physics Research Section A: Accelerators, Spectrometers, Detectors and Associated Equipment*, 557(1): 9 – 15, 2006. ISSN 0168-9002. doi: https://doi.org/10.1016/j.nima.2005.10.047. URL http://www.sciencedirect.com/science/article/pii/S0168900205019674. Energy Recovering Linacs 2005.

A. Neumann, W. Anders, O. Kugeler, and J. Knobloch. Analysis and active compensation of microphonics in continuous wave narrow-bandwidth superconducting cavities. *Phys. Rev. ST Accel. Beams*, 13:082001, Aug 2010. doi: 10.1103/PhysRevSTAB.13.082001. URL https://link.aps.org/doi/10.1103/PhysRevSTAB.13.082001.

A. Neumann, W. Anders, R. Goergen, J. Knobloch, O. Kugeler, S. Belomestnykh, J. Dobbins, R. Kaplan, M. Liepe, and C. Strohman. Cw measurements of cornell llrf system at hobicat. In *Proceedings, 15th Superconducting Radio Frequency Workshop (SRF '2011), Chicago, USA, July 25-29, 2011*, number 15 in Superconducting Radio Frequency Workshop, page MOPO67, Geneva, Switzerland, July 2011. JACoW Publishing. URL https://accelconf.web.cern.ch/SRF2011/papers/mopo067.pdf.

H. Padamsee, J. Knobloch, and T. Hays. *RF superconductivity for accelerators, 2nd Edition*. Wiley, 2008. ISBN 978-3-527-40842-9. URL https://www.wiley.com/en-us/RF+Superconductivity+for+Accelerators%2C+2nd+Edition-p-9783527408429.

Hasan S. Padamsee. Superconducting radio-frequency cavities. *Annual Review of Nuclear and Particle Science*, 64(1):175–196, 2014. doi: 10.

1146/annurev-nucl-102313-025612. URL https://doi.org/10.1146/annurev-nucl-102313-025612.

Dario Pellegrini, Andrea Latina, Daniel Schulte, and S. Alex Bogacz. Beam-dynamics driven design of the lhec energy-recovery linac. *Phys. Rev. ST Accel. Beams*, 18:121004, Dec 2015. doi: 10.1103/PhysRevSTAB.18.121004. URL https://link.aps.org/doi/10.1103/PhysRevSTAB.18.121004.

Yuriy Pischalnikov, Butch Hartman, Jeremiah Holzbauer, Warren Schappert, Samuel Smith, and Jae-Chul Yun. Reliability of the LCLS II SRF Cavity Tuner. In *Proceedings, 17th International Conference on RF Superconductivity (SRF2015), Whistler, Canada, September 13-18*, 2015. URL https://doi.org/10.18429/JACoW-SRF2015-THPB065.

S Posen and D L Hall. Nb3sn superconducting radiofrequency cavities: fabrication, results, properties, and prospects. *Superconductor Science and Technology*, 30(3):033004, jan 2017. doi: 10.1088/1361-6668/30/3/033004. URL https://doi.org/10.1088%2F1361-6668%2F30%2F3%2F033004.

S. Posen and M. Liepe. Measurement of the Mechanical Properties of Superconducting Cavities During Operation. In *Proceedings, 3rd International Conference on Particle accelerator (IPAC 2012): New Orleans, USA, May 2-25*, volume C1205201, pages 2399–2401, 2012a. URL https://accelconf.web.cern.ch/IPAC2012/papers/weppc081.pdf.

Sam Posen and Matthias Liepe. Mechanical optimization of superconducting cavities in continuous wave operation. *Phys. Rev. ST Accel. Beams*, 15:022002, 2012b. doi: 10.1103/PhysRevSTAB.15.022002. URL https://journals.aps.org/prab/abstract/10.1103/PhysRevSTAB.15.022002.

A. Pukhov. Particle-In-Cell Codes for Plasma-based Particle Acceleration. In *CAS - CERN Accelerator School: Plasma Wake Acceleration*, pages 181–206, Geneva, 2016. CERN. doi: 10.5170/CERN-2016-001.181. URL https://doi.org/10.5170/CERN-2016-001.181.

J. Rose, W. Gash, B. Holub, Y. Kawashima, H. Ma, N. Towne, and M. Yeddulla. Nsls-ii rf systems. *Proceedings, PAC*, 2011. URL https://accelconf.web.cern.ch/PAC2011/papers/frobs4.pdf. FROBS4.

Steffen Rudtsch and Christoph von Rohden. Calibration and self-validation of thermistors for high-precision temperature measurements. *Measurement*, 76:1 – 6, 2015. ISSN 0263-2241. doi: https://doi.org/10.1016/j.measurement.2015.07.028. URL http://www.sciencedirect.com/science/article/pii/S0263224115003632.

R. Rybaniec, K. Przygoda, W. Cichalewski, V. Ayvazyan, J. Branlard, L. Butkowski, S. Pfeiffer, C. Schmidt, H. Schlarb, and J. Sekutowicz. Fpga-based rf and piezocontrollers for srf cavities in cw mode. *IEEE Transactions on Nuclear Science*, 64(6):1382–1388, June 2017. ISSN 0018-9499. doi: 10.1109/TNS.2017.2687981. URL https://ieeexplore.ieee.org/document/7887694.

B. Schmitz, J. Köszegi, K. Alomari, O. Kugeler, and J. Knobloch. Magnetometric mapping of superconducting rf cavities. *Review of Scientific Instruments*, 89(5):054706, 2018. doi: 10.1063/1.5030509. URL https://doi.org/10.1063/1.5030509.

S. Setiniyaz, R. Apsimon, and P. H. Williams. Implications of beam filling patterns on the design of recirculating energy recovery linacs. *Phys. Rev. Accel. Beams*, 23:072002, Jul 2020. doi: 10.1103/PhysRevAccelBeams.23.072002.

URL https://link.aps.org/doi/10.1103/PhysRevAccelBeams.23.072002.

O. A. Shevchenko, N. A. Vinokurov, V. S. Arbuzov, K. N. Chernov, I. V. Davidyuk, O. I. Deichuly, E. N. Dementyev, B. A. Dovzhenko, Ya. V. Getmanov, Ya. I. Gorbachev, et al. The novosibirsk free-electron laser facility. *Bulletin of the Russian Academy of Sciences: Physics*, 83(2):228–231, 2019. URL https://doi.org/10.3103/S1062873819020278.

Jonathon Shlens. A tutorial on principal component analysis. *arXiv*, 1404.1100, 2014. URL http://arxiv.org/abs/1404.1100.

Yehoshua Socol. High-power free-electron lasers-technology and future applications. *Optics and Laser Technology*, 46:111 – 126, 2013. ISSN 0030-3992. doi: https://doi.org/10.1016/j.optlastec.2012.06.040. URL http://www.sciencedirect.com/science/article/pii/S0030399212003118.

Valeriia N Starovoitova, Lali Tchelidze, and Douglas P Wells. Production of medical radioisotopes with linear accelerators. *Applied Radiation and Isotopes*, 85:39–44, feb 2014. doi: 10.1016/j.apradiso.2013.11.122. URL http://www.sciencedirect.com/science/article/pii/S096980431300571X.

John S. Steinhart and Stanley R. Hart. Calibration curves for thermistors. *Deep Sea Research and Oceanographic Abstracts*, 15(4):497 – 503, 1968. ISSN 0011-7471. doi: https://doi.org/10.1016/0011-7471(68)90057-0. URL http://www.sciencedirect.com/science/article/pii/0011747168900570.

Neil Stilin, Adam Holic, Matthias Liepe, Ryan Porter, and James Sears. Stable CW Operation of Nb_3Sn SRF Cavity at 10 MV/m using Conduction Cooling. *arXiv*, 2020. URL https://arxiv.org/abs/2002.11755. 2002.11755.

E. T. Swartz and R. O. Pohl. Thermal boundary resistance. *Rev. Mod. Phys.*, 61: 605–668, Jul 1989. doi: 10.1103/RevModPhys.61.605. URL https://link.aps.org/doi/10.1103/RevModPhys.61.605.

M. Tigner. A possible apparatus for electron clashing-beam experiments. *Il Nuovo Cimento (1955-1965)*, 37(3):1228–1231, 1965. doi: 10.1007/BF02773204. URL https://doi.org/10.1007/BF02773204.

Nicholas Valles. *Pushing The Frontiers Of Superconducting Radio Frequency Science: From The Temperature Dependence Of The Superheating Field Of Niobium To Higher-Order Mode Damping In Very High Quality Factor Accelerating Structures*. PhD thesis, Cornell University, Ithaca, NY, 2014. URL https://hdl.handle.net/1813/36143.

Rabi T. Wang, William T. Wagner, and Russell J. Donnelly. Precision second-sound velocity measurements in helium ii. *Journal of Low Temperature Physics*, 68(5):409–417, Sep 1987. ISSN 1573-7357. doi: 10.1007/BF00682305. URL https://doi.org/10.1007/BF00682305.

P. Welch. The use of fast fourier transform for the estimation of power spectra: A method based on time averaging over short, modified periodograms. *IEEE Transactions on Audio and Electroacoustics*, 15(2):70–73, 1967. doi: 10.1109/TAU.1967.1161901. URL https://ieeexplore.ieee.org/document/1161901.

Sigit Basuki Wibowo, Toshihiro Matsumoto, Shinichiro Michizono, Takako Miura, Feng Qiu, and Na Liu. Digital low level rf control system for the international linear collider. *Phys. Rev. Accel. Beams*, 21:082004, Aug 2018. doi: 10.1103/PhysRevAccelBeams.21.082004. URL https://link.aps.org/doi/10.1103/PhysRevAccelBeams.21.082004.

P. B. Wilson. High energy electron linacs: Applications to storage ring rf systems and linear colliders. Technical Report SLAC-PUB-2884, SLAC National Accelerator Laboratory, 1991. URL https://www.slac.stanford.edu/cgi-bin/getdoc/slac-pub-2884.pdf.

Naoto Yamamoto, Takeshi Takahashi, and Shogo Sakanaka. Reduction and compensation of the transient beam loading effect in a double rf system of synchrotron light sources. *Phys. Rev. Accel. Beams*, 21:012001, Jan 2018. doi: 10.1103/PhysRevAccelBeams.21.012001. URL https://link.aps.org/doi/10.1103/PhysRevAccelBeams.21.012001.